

**Studies on Laser Induced and RF Sputtered
Plasma using Optical Emission Spectroscopy and
Langmuir Probe**

Thesis submitted to
COCHIN UNIVERSITY OF SCIENCE AND TECHNOLOGY
in partial fulfillment of the requirements
for the award of the degree of
DOCTOR OF PHILOSOPHY

N. V. JOSHY

**Department of Physics
Cochin University of Science and Technology
Cochin – 682 022, Kerala. കോച്ചിൻ**

June 2008

**Studies on Laser Induced and RF Sputtered Plasma using Optical
Emission Spectroscopy and Langmuir Probe**

Ph.D thesis in the field of plasma physics

Author:

**N. V. Joshy
Optoelectronic Devices Laboratory
Department of Physics
Cochin University of Science and Technology
Cochin – 682 022, Kerala, India
e-mail: joshynv@gmail.com**

Supervisor:

**Dr. M.K. Jayaraj
Reader
Optoelectronics Device Laboratory
Department of Physics
Cochin University of Science and Technology
Cochin – 682 022, Kerala, India
e-mail: mkj@cusat.ac.in**


June 2008

Dr. M.K. Jayaraj
Reader
Department of Physics
Cochin University of Science and Technology
Cochin – 682 022

25th June, 2008

Certificate

Certified that the work presented in this thesis entitled “*Studies on Laser Induced and RF Sputtered Plasma using Optical Emission Spectroscopy and Langmuir Probe*” is based on the authentic record of research conducted by Mr. N. V. Joshy, under my guidance in the Department of Physics, Cochin University of Science and Technology, Cochin – 682 022 and has not been included in any other thesis submitted for the award of any degree.



Dr. M. K. Jayaraj
(Supervising Guide)

Phone : +91 484 2577404 extn 33 Fax: 91 484 2577595 email: mkj@cusat.ac.in

Declaration

Certified that the work presented in this thesis entitled "*Studies on Laser Induced and RF Sputtered Plasma using Optical Emission Spectroscopy and Langmuir Probe*" is based on the original research work done by me under the supervision and guidance of Dr. M. K. Jayaraj, Reader, Department of Physics, Cochin University of Science and Technology, Cochin-682022, and has not been included in any other thesis submitted previously for the award of any degree.

Cochin – 22
25th June, 2008



N. V. Joshy

Contents

| | |
|---|----|
| Preface | i |
| CHAPTER I: Plasma: Models and Production | |
| 1.1 Introduction | 3 |
| 1.2 Plasma properties | 6 |
| 1.2.1 Quasi-neutrality and Debye length | 6 |
| 1.2.2 Plasma sheath | 8 |
| 1.2.3 Plasma oscillations | 10 |
| 1.2.4 Ambipolar diffusion | 12 |
| 1.3 Elementary reactions taking place in plasma | 14 |
| 1.3.1 Collisional excitation/ionization | 14 |
| 1.3.2 Photo-excitation/ionization | 14 |
| 1.3.3 Bremsstrahlung | 15 |
| 1.4 Plasma models | 15 |
| 1.4.1 Thermal Equilibrium (TE) | 16 |
| 1.4.2 Local Thermal Equilibrium (LTE) | 18 |
| 1.4.3 Steady state corona model | 21 |
| 1.4.4 Collisional–Radiative (C-R) model | 23 |
| 1.5 Plasma production | 24 |
| 1.5.1 Laser Induced plasma (LIP) | 25 |
| 1.5.2 RF magnetron plasma | 30 |
| 1.6 Plasma diagnostics | 35 |
| 1.6.1 Optical emission spectroscopy (OES) | 37 |
| 1.6.2 Theory of Langmuir probe | 43 |

| | |
|------------------------------------|----|
| 1.7 ZnO: Optoelectronic importance | 50 |
| 1.8 Review of ZnO plasma studies | 52 |
| References | 56 |

CHAPTER II: Experimental techniques and instrumentation

| | |
|--|----|
| 2.1. Introduction | 67 |
| 2.2 Laser plasma characterization setup | 67 |
| 2.2.1 OES experimental set-up | 68 |
| 2.2.2 Langmuir probe-TOF of charged particles- Experimental set-up | 79 |
| 2.3 RF magnetron plasma characterization setup | 80 |
| 2.4 Voltage ramp and data acquisition set-up | 82 |
| 2.5 Thin film characterization techniques | 85 |
| References | 87 |

CHAPTER III: Optical emission spectroscopic studies of laser ablated zinc oxide plasmas

| | |
|---------------------------------|----|
| 3.1 Introduction | 91 |
| PART- I: Pristine ZnO plasma | |
| 3.2 Experimental conditions | 92 |
| 3.2.1 Laser ablation parameters | 92 |
| 3.2.2 Monochromator calibration | 93 |

| | |
|---|-----|
| 3.3 Results and discussions | 94 |
| 3.3.1 Electron Density and Temperature | 95 |
| 3.3.2 Intensity variation with pressure | 100 |
| 3.4 Conclusions | 103 |
| PART-II: Gallium doped ZnO plasma | |
| 3.5 Experimental set-up | 104 |
| 3.6 Result and discussions | 105 |
| 3.6.1 Spectral emissions | 105 |
| 3.6.2 Electron density (N_e) | 108 |
| 3.6.3 Time of flight (TOF) measurements | 112 |
| 3.6.4 Thin film analysis | 116 |
| 3.7 Conclusion | 118 |
| 3.8 Comparison of OES studies of ZnO and ZnO:Ga plasmas | 118 |
| References | 120 |

**CHAPTER IV: Spatial investigations of ion and electron
time of flight in laser ablated ZnO plasma**

| | |
|-------------------------------|-----|
| 4.1 Introduction | 127 |
| 4.2 Mechanism of DL formation | 128 |
| 4.3 Experimental set-up | 132 |
| 4.4 Results and discussion | 133 |
| 4.4.1 Ion time of flight | 133 |
| 4.4.2 Electron time of flight | 144 |
| 4.5 Conclusion | 153 |
| References | 154 |

**CHAPTER V: Characterization of ZnO plasma in a
Radio Frequency sputtering system**

| | |
|--|-----|
| 5.1 Introduction | 161 |
| 5.2 Experimental set-up | 162 |
| 5.3 Results and discussions | 163 |
| 5.3.1 Langmuir probe measurement | 163 |
| 5.3.2 Optical emission spectroscopic (OES) studies | 170 |
| 5.3.3 Thin film analysis | 173 |
| 5.4 Conclusion | 176 |
| References | 178 |

**CHAPTER VI: Spectroscopic investigations of
laser ablated PZT plume**

| | |
|---------------------------------------|-----|
| 6.1 Introduction | 183 |
| 6.2 Experimental set-up | 184 |
| 6.3 Results and discussion | 185 |
| 6.3.1 Spectral intensity | 185 |
| 6.3.2 Electron density (N_e) | 194 |
| 6.3.3 Electron temperature (kT_e) | 197 |
| 6.3.4 Time of flight studies (TOF) | 198 |
| 6.4 Conclusions | 202 |
| References | 204 |

CHAPTER VIII: Summary and outlook

| | |
|-----------------|-----|
| 7.1 Summary | 208 |
| 7.2 Future work | 211 |
| References | 212 |

Preface

The main objective of the present study is to understand different mechanisms involved in the production and evolution of plasma by the pulsed laser ablation and radio frequency magnetron sputtering. These two methods are of particular interest, as these are well accomplished methods used for surface coatings, nanostructure fabrications and other thin film devices fabrications. Material science researchers all over the world are involved in the development of devices based on transparent conducting oxide (TCO) thin films. Our laboratory has been involved in the development of TCO devices like thin film diodes using zinc oxide (ZnO) and zinc magnesium oxide (ZnMgO), thin film transistors (TFT's) using zinc indium oxide and zinc indium tin oxide, and some electroluminescent (EL) devices by pulsed laser ablation and RF magnetron sputtering.

In contrast to the extensive literature relating to pure ZnO and other thin films produced by various deposition techniques, there appears to have been relatively little effort directed towards the characterization of plasmas from which such films are produced. The knowledge of plasma dynamics corresponding to the variations in the input parameters of ablation and sputtering, with the kind of laser/magnetron used for the generation of plasma, is limited. To improve the quality of the deposited films for desired application, a sound understanding of the plume dynamics, physical and chemical properties of the species in the plume is required. Generally, there is a correlation between the plume dynamics and the structural properties of the films deposited. Thus the study of the characteristics of the plume contributes to a better understanding and control of the deposition process itself. The hydrodynamic expansion of the plume, the

composition, and size distribution of clusters depend not only on initial conditions of plasma production but also on the ambient gas composition and pressure. The growth and deposition of the films are determined by the thermodynamic parameters of the target material and initial conditions such as electron temperature and density of the plasma.

For optimizing the deposition parameters of various films (stoichiometric or otherwise), in-situ or ex-situ monitoring of plasma plume dynamics become necessary for the purpose of repeatability and reliability. With this in mind, the plume dynamics and compositions of laser ablated and RF magnetron sputtered zinc oxide plasmas have been investigated. The plasmas studied were produced at conditions employed typically for the deposition of ZnO films by both methods. Apart from this two component ZnO plasma, a multi-component material (lead zirconium titanate) was ablated and plasma was characterized.

The thesis has been organized in to seven chapters. Chapters III to VI are dedicated to the plasma plume investigation by OES and Langmuir probe. The **Chapter I** begins with a very brief introduction to plasmas in general and then a detailed description of the plasma models in which laser induced plasma (LIP) and RF magnetron plasma are categorized. The mechanisms of laser ablation and RF magnetron sputtering and the subsequent formation and evolution of the respective plumes with variations in the input parameters of plasma production are discussed. The plasma diagnostic techniques and the theory behind it, employed in this investigation are also discussed in this chapter. At the end, a review of the ZnO plasma studies is also included.

Chapter II is titled “Experimental techniques and instrumentation”. The experimental set-up for optical emission spectroscopy and that of time of flight measurement of ions and electrons using Langmuir probe, in the laser ablated plasma are discussed in this chapter. A brief description of the working and of various instruments used in the experimental set-up is also given. The constructional details and working of a high speed voltage ramp generator and data acquisition set-up, indigenously developed for Langmuir probe studies of RF magnetron plasma is presented in the last section of this chapter.

The **Chapter III** comprise of the results of optical emission studies (OES) of laser ablated ZnO plasma. OES studies were performed separately for pristine ZnO and gallium doped ZnO. Both these were ablated at different ambiances of reactive gases and also in vacuum. The plasma plume behavior was studied over the variations in the temperature of the substrate placed at 5 cm distance from the target. The TOF of various emitting species were studied to understand their forward propagation velocities. The plasma parameters are then correlated with the properties of films grown.

The investigation of laser ablated plasma using Langmuir probe is discussed in **Chapter IV**. The kinetic energies of ions were found to fall in to two regimes separated by hundreds of electron volts and exhibited fast decay. The electrons on the other hand exhibited extended temporal profile compared to ions. The electrons also were found to fall in to different energy groups at all laser fluences. The low energy groups were found to merge in to single energy category with very high laser fluence. The ambi-polar electric field arising due to the formation of double layer (DL) accelerates ions and the electrons on the other hand suffer subsequent deceleration. The behavior of electron and ion TOF

with the variation of laser fluences and ambient gas pressure were investigated along the propagation direction of the plume.

Chapter V contains the OES and Langmuir probe investigation of ZnO plasma produced by RF magnetron sputtering. The emission intensity along the plume propagation direction was recorded for all emitting species with sputtering power varying from 25 W to 200 W. The spectral intensity for all species was found maximum at 3 cm to 4 cm distance from the target. The ion density derived from the Langmuir probe measurements also exhibited maximum values at these distances. ZnO thin films were deposited at room temperature on glass substrates at different ambient gas pressures and RF powers for target to substrate distances of 3 cm and 6 cm. The films were analyzed for structural pattern and surface morphology by x-ray diffraction (XRD) and scanning electron microscopy (SEM) respectively. The plasma behavior at various sputtering conditions is correlated with the thin film properties.

The OES study of laser induced plasma of a multi-component target, lead zirconium titanate (PZT) is described in **Chapter VI**. This was done to understand how the plasma produced by the ablation of multi-component plasma differs from the two-component ZnO plasma. The electron density, electron temperature and velocities of the species by TOF studies were determined and compared with those of ZnO plasma.

Chapter VII summarizes the studies carried out in the present work. The electron density and electron temperature calculated for the pulsed laser ablated and RF magnetron sputtered ZnO plasmas are compared. The plasma parameters simulated using indigenously developed Langmuir probe measurements were

found to be similar to that deduced from earlier works. The double layer formation could be detected in laser ablated plasma. The conditions for stoichiometric and fissure-free thin film preparation suggested for ZnO were confirmed by experiments

Part of the thesis has been published/ communicated in the form of following papers

Journal papers

1. Optical emission spectroscopic studies on laser ablated zinc oxide plasma, K. J. Saji, **N. V. Joshy**, and M. K. Jayaraj, J. Appl. Phys. **100**, 043302 (2006).
2. Characterization of radio frequency plasma using Langmuir probe and optical emission spectroscopy, M. Nisha, K. J. Saji, R. S. Ajimsha, **N. V. Joshy** and M. K. Jayaraj, J. Appl. Phys **99** 033304 (2006).
3. Characterization of ZnO plasma in a radio frequency sputtering system, **N. V. Joshy**, Johny Isaac, and M. K. Jayaraj, J. Appl. Phys. (in press).
4. Spatial and Temporal Studies of Laser Ablated ZnO Plasma, **N. V. Joshy**, K. J. Saji, and M. K. Jayaraj, J. Appl. Phys. (under review).
5. Spatial investigations of ion and electron time of flight in laser ablated ZnO plasma, **N.V. Joshy**, K. J. Saji, and M. K. Jayaraj, (to be communicated).
6. High speed voltage ramp and data acquisition circuits for Langmuir probe measurements in radio frequency plasma, **N. V. Joshy**, Johny Isaac, K. J. Saji, and M. K. Jayaraj, (to be communicated)
7. Optical emission spectroscopic characterization of laser ablated PZT plasma, **N. V. Joshy**, S. Sasankakumar, R. Reshmi, and M. K. Jayaraj, (to be communicated)

Conference proceedings

1. Spatial study of RF magnetron plasma using Langmuir probe, **N. V. Joshy**, P. M. Aneesh, K. J. Saji, Johny Isaac, and M. K. Jayaraj, 20th National Symposium on Plasma and Technology, PLASMA (2005)
2. Kinematics of plasma plume generated by Laser ablation of Zinc Oxide, K. J. Saji, **N. V. Joshy**, and M. K. Jayaraj, 20th National Symposium on Plasma and Technology, PLASMA (2005).
3. Studies on RF plasma using Optical Emission Spectroscopy, K. J. Saji., M. Nisha., R. S. Ajimsha., **N. V. Joshy**, and M. K. Jayaraj, 19th National Symposium on Plasma and Technology, PLASMA (2004).
4. Optical emission spectral studies on Laser Ablated ZnO plasma, **N. V. Joshy**, R. Manoj, S. Meenu, and M. K. Jayaraj, DAE-BRNS Workshop on Plasma Surface Engineering September 23-25, (2004).
5. Influence of processing parameters on Pulsed Laser Deposited Zinc Oxide Thinfilms, by R. Manoj, **N. V. Joshy**, S. Meenu, C. Maneesh, and M. K. Jayaraj, IUMRS-ICAM, Yokohama Japan (2003).
6. Influence of processing parameters on the pulsed laser deposited ZnO:Al thin films, R. Manoj, C. Maneesh, S. Meenu. **N.V. Joshy**, Aldrin Antony, and M. K. Jayaraj, Second National Symposium on PLD of thin films PLD-2003, Pune (2003).

Acknowledgements

I put on record my deep sense of gratitude to my research guide, Dr. M. K. Jayaraj, for his unparalleled expertise shown in the guidance of my work and the unreserved willingness to share his knowledge and experience without which the completion of this work within the time frame would have been difficult. It has been a pleasant experience to work with him because of the freedom extended to us in evolving ideas and his forbearance and willingness to hear and acknowledge sincere efforts.

I thank ST. Paul's College management for all the support extended to me in the entire course of my Ph.D. program.

I express my sincere thanks to Prof. Godfrey Louis, Head of the Department and all the former Heads of the Department for permitting me to use the facilities. I also gratefully acknowledge the help and inspiration from all the other faculty members of the Department of Physics.

I am thankful to all the office and library staff of the Department of Physics and the technical staff at VSIC for all the help and cooperation.

I am indebted to Dr. Johney Isaac for his selfless efforts and sincerity shown to me in sharing his knowledge and experience in the instrumentation realm.

I thank University Grants Commission, Government of India for my inclusion in the FIP Scheme of Xth plan.

I remember with gratitude the sincere support extended to me by Mr. Ranjan Mukesh of IPR for sharing his knowledge and experience during the initial stages of my research.

I specially appreciate my colleagues K. J. Saji, R. S. Ajimsha and Anoop Menon for their sincere support and fruitful discussions during my research work,

I acknowledge the efforts of my senior colleagues Dr. Aldrin Antony and Dr. R. Manoj for their contribution in building up the facilities in the lab.

It is very heartening to note that my association with Sasank Kumar, Prince Josevillla, Meenu S. and C. Vineeth has developed in to a strong and lasting friendship. I acknowledge their goodwill.

I would like to express my sincere appreciation to my colleagues in the OED lab Dr. Nisha, Reshmi, , Asha, Rahana, Mini Krishna, Vanaja Madam, Anila teacher, James Sir, for all the help they had extended.

I appreciate and acknowledge with immense pleasure the association with the younger generation of the lab - Aneesh, Arun, Ratheesh, Krishna Prasad, Sanal and Sreeja.

I treasure my friendship with Vineetha, Ragitha, Maneesh chandran, Sukesh, Sarath, Manu, Sanjay, whom I got acquainted with at CUSAT.

I remember with gratitude the support and good will extended to me by my friends Dr. A.V. Alex, Com. V. C. Antony and P. T.C. Titus.

I record my deep and utmost gratitude to my wife and kids- amil & anna- for their selfless support, encouragement, patience and tolerance during the entire period of my research work.

I wish to express my love and regards to Anooja & Anjala for creating lively atmosphere in the evenings when they visit the lab.

I remember with love the support extended to me by my amma, chettan and valiachan right from my school days.

Finally I thank all my well wishers...

I thank God Almighty for his benevolence.

N. V. Joshy

CHAPTER I

Plasma: Models and Production

Abstract

A brief introduction to plasmas in general and a detailed description of the plasma models for laser induced plasma (LIP) and RF magnetron plasmas are presented. The mechanisms of laser ablation and RF magnetron sputtering and the subsequent formation and evolution of the respective plumes with variations in the input parameters of plasma production are also discussed. The plasma diagnostic techniques and the theory behind it, employed in this investigation are also discussed in this chapter. At the end, a review of the studies on ZnO plasma is presented.

1.1 Introduction

The plasma state is often referred to as the *fourth* state of matter, an identification that resonates with the element of *fire*, which along with earth, water and air made up the elements of Greek cosmology according to Empedocles, who lived in Sicily in the 5th century BC. Fire may indeed result in a transition from the gaseous to the plasma state, in which a gas may be fully or, more likely, partially ionized. For the present; we identify *plasma* as any state of matter that contains enough free charged particles for its dynamics to be dominated by electromagnetic forces. In practice quite modest degrees of ionization are sufficient for a gas to exhibit electromagnetic properties. Even at 0.1 per cent ionization, a gas already has an electrical conductivity almost half the maximum possible that is reached at about 1 per cent ionization.

The outer layers of the sun and stars in general are made up of matter in an ionized state and from these regions winds blow through interstellar space contributing, along with stellar radiation, to the ionized state of the interstellar gas. Thus, much of the matter in the universe exists in the plasma state. The earth and its lower atmosphere is an exception, forming a plasma-free oasis in a plasma universe. The upper atmosphere on the other hand, stretching into the ionosphere and beyond to the magnetosphere, is rich in plasma effects. Solar physics and in a wider sense cosmic electrodynamics make up one of the roots from which the physics of plasmas has grown; in particular, that part of the subject known as magneto-hydrodynamics (MHD) was established largely through the work of Alfvén. A quite separate root developed from the physics of gas discharges, with glow discharges used as light sources and arcs as a means of cutting and welding metals. The word *plasma* was first used by Langmuir in 1928 to describe the ionized regions in gas discharges. These origins are

discernible even today though the emphasis has shifted. Much of the impetus for the development of plasma physics over the second half of the twentieth century came from research into controlled thermonuclear fusion on the one hand and astrophysical and space plasma phenomena on the other.

To a degree, these links with big applications of plasma physics over a range of technologies. The use of plasmas as sources for energy-efficient lighting and for metal and waste recycling and their role in surface engineering through high-speed deposition, etching and semiconductor device fabrication may seem prosaic by comparison with fusion and space science but these and other commercial applications have laid firm foundations for a new plasma technology. That said, the main concern throughout this investigation is to focus on the physics of plasmas employed in the fabrication of thin film devices of optoelectronic importance in industry and R &D labs.

Plasma is matter heated beyond its gaseous state, heated to a temperature so high that atoms are stripped of at least one electron from their outer shells, so that what remains are positive ions in a sea of free electrons. Not all the atoms have to be ionized: the cooler plasmas used in plasma processing are only 1-10% ionized, with the rest of the gas remaining as neutral atoms or molecules. At higher temperatures, such as those in nuclear fusion research, plasmas become fully ionized, meaning that all the particles are charged, not that the atoms have been stripped of all their electrons. Ordinary fluids are in thermal equilibrium, meaning that the atoms or molecules have a Maxwellian (Gaussian) velocity distribution [1],

$$f(v) = A \exp\left[-\left(1/2mv^2 / kT_e\right)\right] \quad (1.1)$$

where, A is a normalization factor, and k is Boltzmann's constant. The parameter T_e , is the temperature, which determines the width of the distribution. In plasma, the different species—ions, electrons, and neutrals—may have different temperatures: T_i , T_e , and T_n . These three (or more, if there are different kinds of ions or atoms) interpenetrating fluids can move through one another, but they may not collide often enough to equalize the temperatures, because the densities are usually much lower than for a gas at atmospheric pressure. However, each species usually collides with itself often to have a Maxwellian distribution. Very hot plasmas may be non-Maxwellian and would have to be treated by kinetic theory. A cool plasma would have to have an electron temperature of at least about 10,000°K. Then the fast electrons in the "tail" of the distribution would be energetic enough to ionize atoms they collide with often enough to overcome recombination of ions and electrons back into neutrals. Because of the large numbers, it is more convenient to express temperature in electron-volts ($1eV = 11,600^\circ K$).

Plasma science began in the 1920s with experiments on gas discharges by Irving Langmuir. Plasma physics got its greatest impetus with the start of research on controlled nuclear fusion in the 1950s. The task is to reproduce on earth the thermonuclear reactions occurring in stars to generate their energy. This is possible only by plasmas of over $10^4 eV$ ($\approx 10^8 K$). Another use of plasmas is in the generation of coherent radiation: microwave tubes, gas lasers, free electron lasers, etc. Plasma-based particle accelerators are being developed for high energy physics. Intense x-ray sources using pulsed power technology simulate nuclear weapons effects.

Femto-second lasers can produce plasmas with such a short rise times that very short chemical and biological events can now be studied. Industrial plasmas,

which are cooler, higher pressure, and more complex than those in the applications listed above, are being used for hardening metals, such as airplane turbine blades and automobile parts, for treating plastics for paint adhesion and reduced permeation, for nitriding surfaces against corrosion and abrasion, for forming diamond coatings, and for many other purposes. However, the application of plasma science that is increasingly affecting our everyday life is that of semiconductor production.

1.2 Plasma properties

A brief outline of the inherent plasma properties of plasma in general is presented in this section. The knowledge of the general characteristics of the plasma is essential in the context of identifying different categories of plasmas and the changes occurring in it due to the changes in the input parameters related to plasma production and evolution.

1.2.1 Quasi-neutrality and Debye length

Plasmas are charged fluids (interpenetrating fluids of ions and electrons) which obey Maxwell's equations [Eq. (1.1)], but in a complex way. The electric and magnetic fields in the plasma control the particle orbits. At the same time, the motions of the charged particles can form charge bunches, which create electric fields, or currents, which create magnetic fields. Thus, the particle motions and the electromagnetic fields have to be solved for in a self-consistent way. One of Maxwell's equations is Poisson's equation [1]:

$$\nabla \cdot D = \nabla \cdot \epsilon_0 E = e(N_i - N_e) \quad (1.2)$$

For electrostatic fields, E can be derived from a potential V :

$$E = -\nabla V \quad (1.3)$$

where up on Eq. (1.2) becomes

$$\nabla^2 V = (e/\epsilon_0)(N_e - N_i) \quad (1.4)$$

This equation has a natural scale length for V to vary. To see this, let us replace ∇^2 with $1/L^2$, where L is the length over which V varies. The ratio of the potential energy $|eV|$ of an electron in the electric field to its thermal energy kT_e is then approximately,

$$\left| \frac{eV}{kT_e} \right| = L^2 \frac{(N_e - N_i)e^2}{\epsilon_0 kT_e} \quad (1.5)$$

The natural length scale on the right, called the Debye length λ_D , is defined by

$$\lambda_D = \left(\frac{\epsilon_0 kT_e}{N_e e^2} \right)^{1/2} \quad (1.6)$$

Debye length is an important plasma parameter, which is a measure of shielding distance or thickness of the sheath. If an electric field is created in the plasma, the charged particles will react to reduce the effect of the field. The electron being lighter and more mobile will respond fast to reduce the electric field. The response of charged particles to reduce the effect of local electric field is called Debye shielding and shielding gives the plasma its quasi-neutrality. If an electric potential is applied between two surfaces immersed in plasma, the surfaces will attract the equal amount of opposite charges. The concentration of charged particles near the two surfaces will shield the charged surfaces from the plasma

bulk. The applied electric potential will therefore develop mostly near the surfaces over a distance λ_D , called Debye length defined by Eq. (1.6).

Another plasma parameter related to Debye length is, the number of particles, N_D , in the Debye sphere, which is a sphere of radius λ_D . The solution of Poisson's equation given by Eq. (1.4) can be obtained only by assuming that the shielding effect is produced by a large number of electrons or the shielding can occur only if Debye sphere contains a large number of electrons. Due to the exponential decay of the potential, it can be assumed that the shielding is caused by electrons in the Debye sphere, whose number is given by,

$$N_D = \frac{4\pi}{3} N_e \lambda_D^3 = \frac{1.178 \times 10^9 T_e^{3/2} (eV)}{N_e^{1/2}} \quad (1.7)$$

N_D has to be therefore much larger than unity to fulfill the collective characteristic of the plasma. In the interior of a plasma, the charge densities must be very nearly equal, and we may define a common density, called the plasma density N , to be either N_i or N_e . However, there are regions, called sheaths, where L is the order of λ_D , there, the ratio N_i / N_e does not have to be near unity. The condition $N_i \approx N_e$ is called quasi-neutrality and is probably the most important characteristic of a plasma. Charged particles will always find a way to move to shield out large potentials and maintain equal densities of the positive and negative species.

1.2.2 Plasma sheath

If L is of the order of the Debye length, then by Eq. (1.5), the quasi-neutrality condition can be violated. This is what happens near the walls around plasma and near objects, such as probes, inserted into the plasma. Adjacent to the surface, a sheath of thickness about $5\lambda_D$ forms [1], in which the ions outnumber

the electrons and a strong electric field, is created. The potential of the wall is negative relative to the plasma, so that electrons are repelled by a Coulomb barrier. This is necessary because electrons move much faster than ions and would escape from the plasma and leave it positively charged (rather than quasi-neutral) unless they were repelled by this "sheath drop".

If an isolated material body is placed in contact with plasma, the electron current to the body is initially much larger than that of ion current. The isolated body will therefore be charged $-$ vely until its potential is lowered sufficiently that the net charge arriving at the body is zero. Since no current can flow through an isolated body an equal number of $+ve$ and $-ve$ charge must arrive at the body per unit time for equilibrium to exist. Thus there exists a potential difference or contact potential with respect to plasma. Such a region, through which the potential drop takes place, is called sheath region. This $-ve$ potential region must repel further electrons leaving from plasma, and the $+ve$ ions enter into the sheath will be swept into the body. It follows that the $+ve$ and $-ve$ charge densities within the sheath region will be unequal [2].

The plasma is virtually electric field free, except around the perturbations, and so is equipotential. Let us call this potential as plasma potential (space potential) V_p and there associate a floating potential V_f with the isolated substrate. Since V_f is such as to repel electrons, then $V_f < V_p$. In the absence of a reference $V_p - V_f$ is meaningless. Because of the charging of the substrate, it is as though a potential energy 'hill' develops in front of the substrate (Fig. 1.1). However it is a downhill journey for ions from the plasma to the substrate, but uphill for the electrons, so that only those electrons with enough initial kinetic energy make it to the 'top' i.e., the substrate.

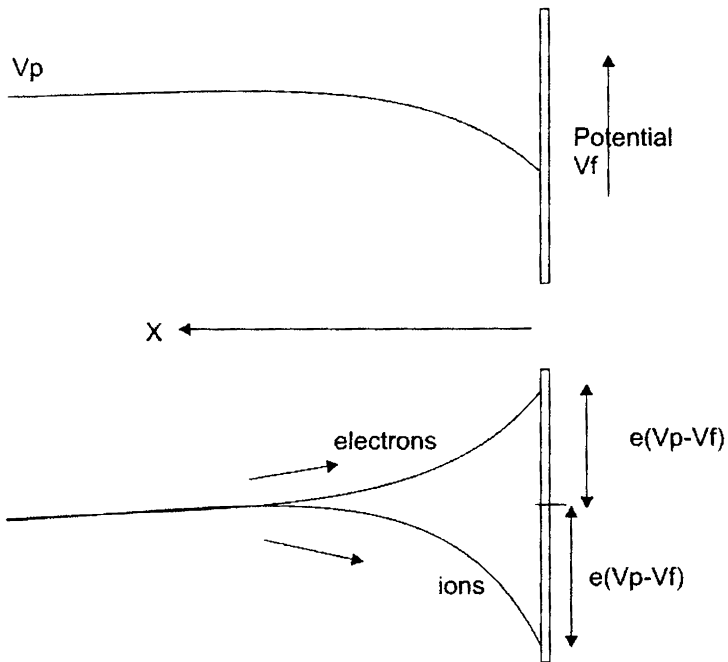


Fig.1.1 Variation of electrical potential (upper) and the potential energies of electrons and positive ions (lower) in the vicinity of an electrically floating substrate.

1.2.3 Plasma oscillations

If there occurs a charge separation (+ve ions and electrons) in plasma by some means, an electric field is established. This field will tend to accelerate the electrons back to their equilibrium position. Due to their momentum they will overshoot the equilibrium position and an electric field in opposite direction is

set up. The electrons will then be accelerated back and will tend to oscillate about their equilibrium position. This high frequency oscillation in a gas discharge is called plasma oscillations [2]. Frequency of oscillation is given by

$$\omega_e = \left(\frac{N_e e^2}{m_e \epsilon_0} \right)^{1/2} \quad (1.8)$$

ω_e is called plasma frequency, m_e the electron mass and ϵ_0 , the permittivity of free space N_e is the electron density. It should be of the order of GHz. Plasma density is frequently described by ω_e rather than N_e itself.

$$\lambda_D \omega_e = \left(\frac{\epsilon_0 k T_e}{N_e e^2} \right)^{1/2} \times \left(\frac{N_e e^2}{m_e \epsilon_0} \right)^{1/2} = \left(\frac{k T_e}{m_e} \right)^{1/2} \approx \bar{U}_e \quad (1.9)$$

where \bar{U}_e is the RMS velocity of electrons and T_e is electron temperature.

The relationship $\lambda_D \omega_e \approx \bar{U}_e$ says that the electrons can move a distance of about λ_D in a time of $1/\omega_e$. This means that if the plasma is disturbed by an electromagnetic wave of angular frequency ω , then the plasma electrons can respond fast enough to maintain neutrality if $\omega < \omega_e$. So ω_e is the minimum frequency for propagation of longitudinal waves in plasma.

Just as the electrons could oscillate in the plasma, so also can the ions. The mass of the ions (m_i) ensures that their oscillations are so slow that the electrons can maintain thermal equilibrium. The ion frequency is more complex to find than the electron frequency. However in the case where T_e is large, the ion oscillation frequency ω_i simplifies to the form,

$$\omega_i = \left(\frac{N_i e^2}{m_i \epsilon_0} \right)^{1/2} \quad (1.10)$$

In Langmuir's work, he discovered that certain regions of a plasma discharge tube exhibit periodic variations of electron density, which we nowadays terms *Langmuir waves*.

1.2.4 Ambipolar diffusion

Whenever there is a concentration gradient of particles, the random motion of the particles results in a net flow down the gradient. This is the phenomenon of diffusion [3]. The resulting ion (J_i) and electron (J_e) current densities in the presence of a diffusion gradient dN/dx (one dimension) can be written as

$$J_e = -eD_e \left(\frac{dN_e}{dx} \right) \quad (1.11)$$

$$J_i = -eD_i \left(\frac{dN_i}{dx} \right) \quad (1.12)$$

D_e and D_i are the diffusion coefficients and N_e and N_i the number densities of the electrons and ions respectively. Diffusion coefficient and mobility (μ) are related by temperature as $D / \mu = kT / e$. This is Einstein's relation. Since the mobility of electrons is very much greater than that of the ions, the electron diffusion coefficient will be very much greater than the ion diffusion coefficient. One might see as a result that, in a region of concentration gradient, the electrons would stream out very much faster than ions. This is initially true, but the exodus of the electrons leaves the rest of the plasma more +ve and set up a

restraining electric field E which grows large enough to equalize the diffusion rates of the ions and electrons. In the presence of both the resulting electric field E and the diffusion gradient, J_i and J_e becomes,

$$J_i = eN_i\mu_i E - eD_i \frac{dN_i}{dx} \quad (1.13)$$

$$J_e = -eN_e\mu_e E - eD_e \frac{dN_e}{dx} \quad (1.14)$$

At the equalization of diffusion rates $J_i = J_e$. Since N_i and N_e and hence their gradients are closely equal throughout the whole body of plasma. Equating current densities gives

$$EN_e(\mu_i + \mu_e) = (D_i + D_e) \frac{dN_e}{dx}$$

$$E = \frac{(D_i + D_e)}{N_e(\mu_i + \mu_e)} \frac{dN_e}{dx} \quad (1.15)$$

Substituting this value of E back in equations (1.13) or (1.14),

$$J_i = J_e = \frac{(D_i\mu_i + D_e\mu_e)}{(\mu_i + \mu_e)} \frac{dN_e}{dx} \quad (1.16)$$

So the collective behavior of ions and electrons causes them to move with the same diffusion coefficient. This is the phenomenon of ambi-polar diffusion, which will apply to all motions within the plasma.

1.3 Elementary reactions taking place in plasma

Several processes involving atoms, ions, electrons, and photons, take place in a plasma. These can all be characterized by rate equations and corresponding time constants. The most important ones, i.e., those which determine the conditions in the plasma, are discussed below [4]. For each process there is an exact inverse process.

1.3.1 Collisional excitation/ionization

It involves a collision between an electron and an atom/ion. Kinetic energy from the electron is transferred to the atom/ion which is excited to a higher energy state. The opposite, collisional de-excitation occurs when an electron collides with an excited atom/ion which de-excites and transfers energy to the electron.



where, $A(q)$ and $A(q)^*$ are atom/ion in the lower and upper states respectively. Collisional ionization can occur if the free electron has sufficient energy to release another electron from the atom/ion. If two electrons encounter an ion and one electron recombines, we have collisional recombination. This event is also referred to as three body recombination.



1.3.2 Photo-excitation/ionization

Photo-excitation occurs when an incoming photon is absorbed and the atom/ion is raised to a higher energy level. Photo-de-excitation is the reverse process and normally referred to as a bound-bound process, i.e., the electron is bound both before and after the process. Such a process yields emission with distinct energies, i.e., line emission. The spectral width of such a line is governed by

several line-broadening mechanisms. Natural broadening is due to the limited lifetime of the excited state. In high temperature plasmas, Doppler broadening, due to the velocity distribution of the emitting ions is important. Furthermore, the influence of strong electric and magnetic fields results in Stark and Zeeman effects.

$$A(q) + h\nu \leftrightarrow A(q)^* \quad (1.19)$$

Photo-ionization occurs when the incident photon has sufficient energy to remove an electron from the atom/ion. In photo-recombination, an incoming electron recombines with an ion resulting in the emission of a photon. This is called a free-bound transition and yields continuous radiation.

$$A^{z+} + h\nu \leftrightarrow A^{(z+1)+} + e \quad (1.20)$$

1.3.3 Bremsstrahlung

Bremsstrahlung occurs when a free electron is decelerated by the influence of an atom/ion. The loss in kinetic energy is emitted as a photon. In inverse bremsstrahlung, the energy from an incoming photon is converted to an increase in the kinetic energy of a free electron in the close vicinity of an ion. Bremsstrahlung is a free-free transition and the emitted radiation is continuous.

1.4 Plasma models

In order to predict the relative behavior of any atomic species in the plasma, we must know the expected population of its various possible states. In many cases, the life times of plasma or atomic species are insufficient to guarantee that an equilibrium population has been achieved. For example, the plasma produced by the pulsed laser ablation is highly transient and it cools off within a few

microseconds. During this cooling down process the plasma emits continuum radiation due to bremsstrahlung and recombination process and discrete radiation due to de-excitation processes of atoms and ions present in the plasma. However some type equilibriums are obtained in some plasma and so it of interest to understand those.

To obtain the information regarding the macroscopic behavior of the plasma by a kinetic description, we should solve a complex system of equations describing all the reactions that occur in the plasma. They are ionization, dissociation, recombination, elastic and inelastic collisions, radiative emission, photon re-absorption and bremsstrahlung processes, discussed in the previous section. The rates of all these reactions should be properly estimated. For this, the thermo-dynamical approach is usually preferred, relying on the hypothesis of infinite rate coefficients.

1.4.1 Thermal Equilibrium (TE)

For a thermo-dynamical description, it is essential to keep in consideration, the contribution of different forms of energy present in the plasma. The equilibrium distribution of these energies are respectively the Maxwell, Boltzmann and Planck functions, each one characterized by a parameter T , the temperature. A system is in complete thermo-dynamical equilibrium, (TE), if all the forms of energy are in equilibrium with each other. This happens when the rate of a reaction is the same as the rate of inverse process for all processes. In this case the parameter T is the same for all the distributions, assuming the familiar meaning of temperature and the principle of detailed balance must hold. Under TE conditions the population of the excited levels for each species follows the Boltzmann distribution [5]:

$$\frac{N_i}{N_j} = \frac{g_i}{g_j} \exp[-(E_i - E_j)/kT] \quad (1.21)$$

where, N_i and N_j are the population densities of the excited levels i and j respectively, g and E are the statistical weight and excitation energy of the levels respectively and T is the temperature. Also the radiation is in thermal equilibrium and so is given by the black body level.

$$\rho(\nu) = 8\pi h \nu^3 / [\exp(h\nu / kT) - 1] c^3 \quad (1.22)$$

where, $\rho(\nu)$ is the energy density per unit frequency. Now this will be an equilibrium situation if the rate at which atoms make transitions from i to j is equal to the rate at which they go from j to i . This is known as the principle of detailed balance and leads to,

$$(A_{ij} + B_{ij}\rho)N_i = B_{ji}\rho N_j \quad (1.23)$$

The numbers A_{ij} , B_{ij} and B_{ji} are called the Einstein's Coefficients. The population of the different ionization stages in the TE hypothesis is described by Saha equation, which in the case of the neutral and singly ionized species of the same element can be written as,

$$\frac{N_e N_i}{N_a} = \frac{K_{ion}}{\alpha_{rec}} = \left(\frac{2g_i}{g_a} \right) (2\pi m_e kT / h^3)^{3/2} \times \exp[-(E_a - \Delta E_{ion}) / kT] \quad (1.24)$$

where, N_e , N_i and N_a are the plasma electron density, and the number densities of the singly ionized species and the neutral atomic species, respectively. K_{ion} and α_{rec} are the ionization and recombination rates respectively. E_a is the energy of atomic transition while ΔE is the energy of the ionic transition plus the

ionization potential of the neutral species in the ground states and m_e , the electron mass.

1.4.2 Local Thermal Equilibrium (LTE)

The above mentioned situations cannot be fully realized in many of the plasma generated in the laboratory. Therefore some kind approximation must be adopted to describe their states. In laser induced plasma (LIP), the radiative energy is decoupled since radiative energy requires the plasma to be optically thick at all frequencies (black body). This kind of plasma is usually described by a state known as local thermal equilibrium (LTE). In LTE model, it is assumed that the distribution of population densities of electrons is determined exclusively by particle collision process that the later takes place with sufficient rapidity that the distribution responds instantaneously to any change in the plasma conditions. This means that the collision processes are much more effective than the radiative processes in establishing the plasma thermodynamics, ie if the characteristic collision time $1/\nu_{col}$ is much less than the characteristic time for decay, $\tau_{rad} = 1/\Delta\nu_{nat}$, where, $\Delta\nu_{nat}$, is the natural line width of plasma emission lines. Under these conditions the non-equilibrium of the radiations can be neglected and the atoms, ions and electrons can be considered to be at equilibrium. It is thus possible to find a temperature parameter that satisfies both Boltzmann and Maxwell distributions and Saha law. If LTE is a good approximation of the plasma state, the plasma excitation temperature (T_e) and electron density (N_e) can be used to describe the plasma characteristics and the plasma analysis become possible.

Since the electrons, because of their greater velocity are most efficient particles in causing collisional transitions, it is their collision rate that need to be

compared with the radiative decay rates. Thus, consider atoms or ions in some level p making transition to the lower state q , as they are struck by electrons. The rate at which these transitions take place may be expressed as [6],

$$\text{Collision rate} = N_e N(p) X(T_e, p, q) \quad (1.25)$$

where, $X(T_e, p, q)$ is defined as the de-excitation coefficient and $N(p)$ is the number of atom or ions in the level p . The RHS of Eq. (1.25) is expressed in terms of transitions/unit volume/unit time. For radiation decay rate to cause less than 10% departure from LTE, the collisional rate must be at least 10 times the radiative rates. That is for all levels p and q ,

$$N_e N(p) X(T_e, p, q) \geq 10 N(p) A(p, q) \quad (1.26)$$

where, $A(p, q)$ is the atomic transition probability.

Griem [7] and Wilson [8] developed separately the criterion for the applicability of LTE model based on the assumption that the LTE model cannot be applied to optically thin plasma. At sufficiently low density, the probability of radiative transition becomes comparable with or even exceeds the probability of corresponding collisional transition. In optically thin plasma, the process of emission of photon is not balanced by its inverse because the population distribution among levels departs from that predicted by Boltzmann equation. For hydrogen – like atom Griem found a condition on electron density (expressed in cm^{-3}) for which a level p in partial LTE, with a confidence of 10 % as,

$$N_e \geq 7 \times 10^{18} \left(z^7 / p^{17/2} \right) \left(k T_e / z^2 E_H \right)^{1/2} \quad (1.27)$$

E_H is the ionization potential of hydrogen atom and $z = 2$ for singly charged ions. So in hydrogen plasma, the population of the third level is (with a confidence of 10 %) in LTE with highest levels, if

$$N_e \geq 1.7 \times 10^{14} \text{ cm}^{-3} \quad (1.28)$$

More generally the lower limit of electron density N_e is given (in cm^{-3}) by Mc Whirter criterion [6] deduced from equation (1.26) is

$$N_e \geq 1.6 \times 10^{12} T_e^{1/2} \Delta E^3 \text{ cm}^{-3} \quad (1.29)$$

where, ΔE (in eV) is the highest energy transition for which the condition (1.29) holds and T_e is the plasma temperature in $^\circ\text{K}$. This criterion is a necessary, though insufficient condition for LTE. The expressions found by the other two authors- Griem and Wilson- are in good agreement with Eq (1.29). They differ only in the constant.

| | |
|-----------------------|------------------------|
| Griem | = 9.2×10^{16} |
| Wilson | = 1.3×10^{17} |
| Mc Whirter (Eq. 1.29) | = 1.6×10^{17} |

In a time evolving plasma, like those produced in pulsed laser ablation, besides the above mentioned Mc Whirter criterion expressed in Eq. (1.29), a further condition must hold to have LTE. Since the plasma expands and cools, it is necessary that the characteristic time on which T_e and N_e change is much longer than the time, τ_{rel} needed to cause the plasma to equilibrate. In this case the plasma evolves passing through a succession of LTE states. If this is not the case, the plasma evolves very fast and does not reach equilibrium. This condition is more easily fulfilled at later stages of evolution than the early times,

where the plasma has slowed down its evolution. LTE can still be achieved at initial stages of expansion when ablated in ambient gas pressures, in which case the expansion is slower and number density N_e higher.

1.4.3 Steady state corona model

In order to explain some features of the solar corona, an atomic model has been proposed which has been found useful in discussing low density laboratory plasmas. Instead of each collision process being balanced by its inverse collision process as in LTE model, the balance in corona model is between collisional ionization (and excitation) and radiative recombination (and spontaneous decay). In this model, it is assumed that the radiation escape without interacting with plasma (optically thin approximation).

If the plasma density is lowered very much less than LTE equilibrium, only the strongest of the collision processes can influence the plasma. Consider the process of collisional ionization and three body recombination [Eq. (1.18)], which because they are inverse processes, must take place at equal rate in LTE. The ionization rate is proportional to N_e and recombination rate is proportional to N_e^2 . The positive ions may also recombine with electrons by radiative processes [Eq. (1.20)]. The rate of this process is proportional to N_e , so that at sufficiently low electron density, it is more important than three body recombination. Then the ionization equilibrium is a balance between recombination and ionization by electron collision. Such plasma is called corona model plasma and it refers to plasma of much lower density than LTE model so that atom-atom collision is negligible. The question is how high the electron density may be before the corona model breaks down. This limit of maximum density is reached when collisions start to interfere with the assumption that the

only mechanism of decay is by emission of radiation. The most probable collision process of this nature is the collision between an excited atom or ion and an electron where the atom or ion makes transition to a neighboring level. It is sufficient to take the following as the criterion of applicability of corona model [6]

$$\sum_{s < p}^q A(p, s) \geq N_e X(T_e, p, q) \quad (1.30)$$

where, A is an atom or ion having energy levels p , s and q with $s < q$ and $X(T_e, p, q)$ the de-excitation coefficient.

At the limiting value of N_e , there are as many collisional transitions out of level p as radiative level p . The inequality (1.30) is evaluated to get,

$$N_e < 5.6 \times 10^8 (z+1)^6 T_e^{1/2} \exp\left[\frac{(1.162 \times 10^3 \times (z+1)^2)}{T_e}\right] \quad (1.31)$$

To meet the requirements of corona model, the electron temperature must be greater than $10^4 K$ (for more than 1% ionization of all atoms). The number density N_e between LTE limit and corona limit differ by a magnitude of 10^6 orders. Corona equilibrium is exhibited by plasmas produced by radiofrequency (RF) and direct current (DC) magnetron sputtering, electron cyclotron resonance (ECR), and microwave plasmas. The electron density (N_e) of the order 10^{11} cm^{-3} and electron temperature (kT_e) in the range 1.5 eV to 5 eV has been reported [9-22] for these plasmas.

1.4.4 Collisional–Radiative (C-R) model

The collisional–radiative model was developed to fill the gap of several orders of magnitude (10^6) in the electron density where neither the LTE model nor the corona equilibrium is valid. This is a modification of the corona model which takes in to account collisional transition as well as radiative decay from higher bound levels, three body recombination and radiative recombination. Again it is assumed that the radiation produced in the interior of the plasma escape with no trapping. ie, the plasma is treated in the optically thin approximation. The basic assumptions in C–R model are,

1. Free electrons have Maxwellian velocity distribution.
2. The transitions between any pair of bound levels are induced by electron collisions. These processes are represented by Eq. (1.17)
3. Ionization is by electron collision from any bound level and is partially balanced by three body recombination to any level. The process may be represented by Eq. (1.18)

The Tokamak plasma, produced in nuclear fusion experiments, is a good example where the C–R model is effectively employed for the determination of plasma parameters. Figure 1.2 is an illustration [23] of various plasmas those occur in nature and produced in laboratory, in terms of the respective number density and temperature.

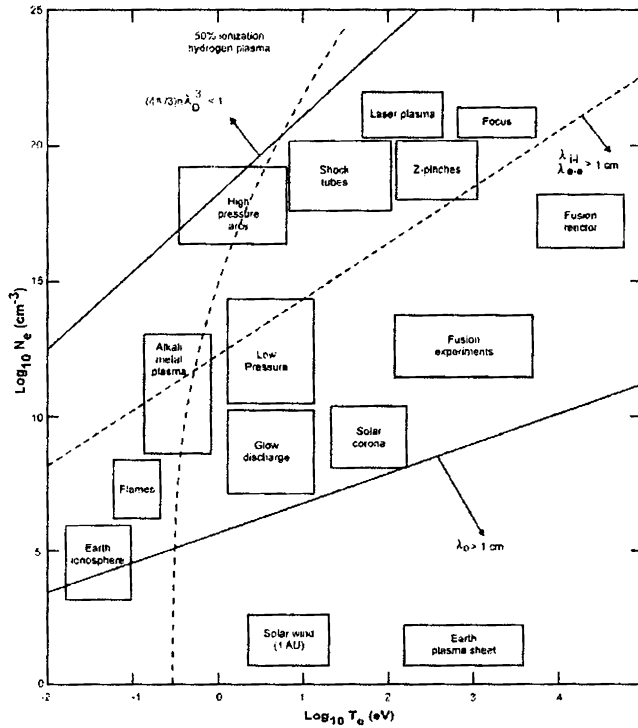


Fig. 1.2: Sketch of approximate magnitudes of N_e and kT_e giving a comparable information on some typical plasmas

1.5 Plasma production

Plasma is produced by a variety of methods in laboratory, viz, laser induced plasma (LIP), RF/DC magnetron sputtering, ECR, microwave, Tokamak, plasma spray etc, which are generated for the purpose of thin film or device applications, fundamental research or to meet the commercial and industrial needs. The choice and mode of plasma production are governed by the use and applicability to the systems which adapts itself to the plasma bulk behavior.

For plasma assisted, stoichiometric thin film depositions or device fabrications, LIP or RF magnetron plasmas are the most versatile and time tested ones. The theoretical and technical feasibility of these plasma productions by virtue of the exciting source parameters and ambience of plasma evolution, are discussed in the following sections.

1.5.1 Laser Induced plasma (LIP)

Laser-produced plasma is transient in nature with characteristic parameters that evolve quickly and are strongly dependent on irradiation conditions such as incident laser intensity and pulse duration, laser wavelength, irradiation spot size, ambient gas composition and pressure [24-31]. The different mechanisms involved during a laser ablation process, including laser absorption, evaporation, transient gas dynamics, radiation transport, condensation, ionization and recombination, are rather complex and require rigorous and elaborate investigations. These mechanisms are also dependant on the type of material (metal, semi-conductor, or insulator and single, two component or multi-component) target used for ablation.

(i) Physical description of laser plasma expansion

The interaction of high-intensity laser pulses with a solid target involves laser–solid interaction and plasma formation. The process can be divided schematically into two different regimes:

(a) At low laser fluence the vapor produced by the leading edge of the laser pulse behaves like a thin medium and the laser beam passes nearly unattenuated through the vapor.

(b) At high laser fluence the vapor temperature is high enough to cause appreciable atomic excitation and ionization. Then the vapour begins to absorb the incident laser radiation leading to vapor breakdown and plasma formation.

A typical intensity profile can be found from the exponential attenuation of the incident laser light with intensity I_0 .

$$I_{(z)} = (1 - R)I_0 \exp(-\alpha z) \quad (1.32)$$

where, R is the reflectivity in which $1 - R = A$, the surface absorbance and α , the absorption coefficient. The attenuation length (laser absorption length)

α^{-1} is typically around 10 nm for most metals. UV light has a low reflectivity for many metals and other materials in contrast to IR light [32]. This has made UV lasers attractive for material processing and for PLD. In nanosecond laser heating of metal, the absorbed laser energy, first heats up the target to the melting point and then to its vaporization temperature whereas laser ablation with femto and pico-second laser pulses can be considered as a direct solid–vapour transition.

In the former case evaporation occurs from the liquid metal, and heat conduction into the solid target is the main source of energy loss. Several authors [33-36] have performed a detailed analysis of the laser–solid interaction in the nanosecond regime. The vaporization process is often described by using the heat flow equation in one-dimensional form, as appropriate to many experimental conditions (normal vaporization) [37, 38]

$$\rho c \frac{\partial T}{\partial t} = \frac{\partial T}{\partial z} \left(K \frac{\partial T}{\partial z} \right) + \alpha A I_0 \times \exp(-\alpha z) \quad (1.33)$$

where T , ρ , c , K and A are temperature, mass density, specific heat, thermal conduction and surface absorbance of the target, respectively, while I_0 is the

intensity of the incident laser pulse, and z the coordinate normal to the target surface. For conducting materials the energy, which is deposited by the laser light within the absorption layer $z = 1/\alpha$, propagates more deeply into the bulk. The critical parameter is the thermal diffusivity D , given by,

$$D = K / (\rho c) \quad (1.34)$$

A typical length scale for thermal processing is the heat diffusion length, given by,

$$l_{th} = 2(D\tau_L)^{1/2} \quad (1.35)$$

where, τ_L is the pulse width of the laser. For multi-component solids, a small thermal diffusion depth is a necessary condition for stoichiometric ablation [39]. When the laser intensity exceeds the ablation threshold of the target, the laser beam evaporates and ionizes material, creating a plasma plume above the material surface. Initially the atoms, molecules and ions undergo collisions in the high-density region near the target forming the so-called Knudsen layer [40], leading to a highly directional expansion perpendicular to the target surface. The expansion dynamics of the laser-produced plasma plume have been described using semi-quantitative models [41,42]. In the initial stage, the interaction of the laser beam with the bulk target results in the evaporation of the surface layer. Following this, the interaction of the laser beam with the evaporating material leads to the formation of an isothermally expanding plasma and this persists until the termination of the laser pulse. The vapor particles are pushed forward and in the lateral direction solely by high pressure emanating from the target surface when the ejected plume is considered transparent to the incident laser beam. Strong laser-plasma interaction creates an additional high-pressure and kinetic energy fuelling further expansion of the plume. The two dominant

photon absorption processes at this stage of ablation in laser-produced plasmas are and photo-ionization (PI) inverse Bremsstrahlung (IB) [see sections 1.3 (ii) and (iii)].

The IB process involves the absorption of photons by free electrons, which gain energy from the laser beam during collisions with neutral and ionized atoms. IB due to electron–neutral interaction is usually one or two orders of magnitude smaller than that due to electron–ion interaction when the ion density is high. The expression for IB absorption coefficient, α_{IB} , of an electron gas with a Maxwellian velocity distribution and a kinetic temperature T_e due to electron–ion collisions is given by [43,44]

$$\alpha_{IB} = 1.369 \times 10^{-23} \left[\frac{z^3 N_i^2 \lambda^3}{T_e^{1/2}} \right] \times \left[1 - \exp \left[- \frac{h\nu}{kT_e} \right] \right] \text{cm}^{-1} \quad (1.36)$$

where z is the charge state of the ion, N_i the ion density (in cm^{-3}), λ the wavelength (in cm), T_e the electron temperature (in $^{\circ}\text{K}$) and $h\nu$ the laser energy. The IB process is less efficient in the UV than in the visible and IR part of the light spectrum but the phenomenon of direct PI of excited atoms in the vapour can play a significant role [43].

After the termination of the laser pulse, no particles are ejected from the target surface. An adiabatic expansion of the plasma occurs where the temperatures can be related to the dimensions of the plasma. The adiabatic expansion has been treated by Anisimov et al. [45,46] and Singh and Narayan [41]. It has been pointed out that the forward directed nature of the laser evaporation process results from anisotropic expansion velocities of different species, which are mainly controlled by the initial dimensions of the expanding plasma. The thermal energy is rapidly converted into kinetic energy, with the plasma attaining extremely high expansion velocities. According to Singh and Narayan,

after the laser pulse is terminated, the plume expands adiabatically with the additional assumptions that there are no spatial variations in the plume temperature, i.e. $\Delta T = 0$. As pointed out by Anisimov et al. this approximation is undoubtedly questionable and also the results from their calculations of the angular and energy distribution of the ablated atoms are for a multicomponent system (YBaCuO -target) and cannot easily be generalized to other materials.

During the initial stages of plasma expansion when the particle density is high ($\sim 10^{19} \text{ cm}^{-3}$), the mean free path of the particles is short ($\sim \mu\text{m}$) and the plasma behaves as a continuum fluid. As the plasma expands the temperature drops very rapidly (within 100 ns time), however the drop in temperature is smaller at later times ($>100 \text{ ns}$) because energy is regained through recombination of ions. The plasma expands freely in vacuum or low pressures. As the background pressure increases, the plume behavior is characterized by strong interpenetration of the laser plasma and ambient low-density gas. The expansion dynamics of the plume in this pressure regime is determined by the properties of the plasma as well as the background gas. In this regime collisional effects starts to play a role. At still higher background pressures, the expansion dynamics of the plasma are fully governed by the nature and pressure of the ambient gas used [46]. In general, an increase in background pressure results in the following effects: (i) an increase in fluorescence from all species due to enhanced collisions on the expansion front and subsequent inter-plume collisions, (ii) shock front formation, (iii) slowing of the plume compared to propagation in vacuum resulting in spatial confinement of the plasma. The presence of ambient gas during expansion may also lead to reactive scattering, thermalization of the plume, enhanced condensation leading to cluster and nanoparticle formation, etc.

1.5.2 RF magnetron plasma

Magnetron plasma sources are being widely used in many industrial and technological processes, especially those related to sputter-etching and thin film deposition applications [48-53]. The high deposition rate achieved has turned the magnetron sputtering techniques into one of the most popular methods to deposit dielectric, metallic, and compound films. Magnetron sputtering is particularly useful when high deposition rates and low substrate temperatures are required [54]. The homogeneity and quality of these films have motivated intensive research by the scientific community devoted to relate external input parameters to the properties of the resulting film [55-58].

(i) Principles of magnetron sputtering

The magnetron sputtering principle was first reported by Penning [59] in 1936 and it took nearly 40 years for the invention of the planar magnetron, which is the work-horse in magnetron sputtering deposition today. The basic feature of a magnetron discharge is the confinement of the plasma in front of the target (cathode) [60,61]. This is achieved by the combination of electric and magnetic fields [60]. The magnetic field strength is adjusted in such a way (about 50 to 200 mT) that the electrons are significantly influenced by the magnetic field while the ions are not. The electrons perform cycloidal orbits in the crossed electric and magnetic fields, leading to very high ionization efficiency. Therefore, magnetron discharges can be sustained at much lower pressures ($<10^{-2}$ Pa) and/or higher current densities than the glow discharges. A schematic diagram of a magnetron sputtering discharge is shown in figure 1.3. The magnetic field confines the electrons in front of the target in a torus-like plasma region which causes a non-uniform erosion of the target. The potential

distribution in the discharge, i.e. between the target and the substrate, is essential for the sputtering and the deposition of the film. This potential distribution determines the energies of the ions and neutral species which contribute to the deposition process. The external discharge parameters such as working pressure, discharge power, design of the magnetic field (i.e. balanced or unbalanced magnetrons) and the excitation mode (DC or RF) influence the potential.

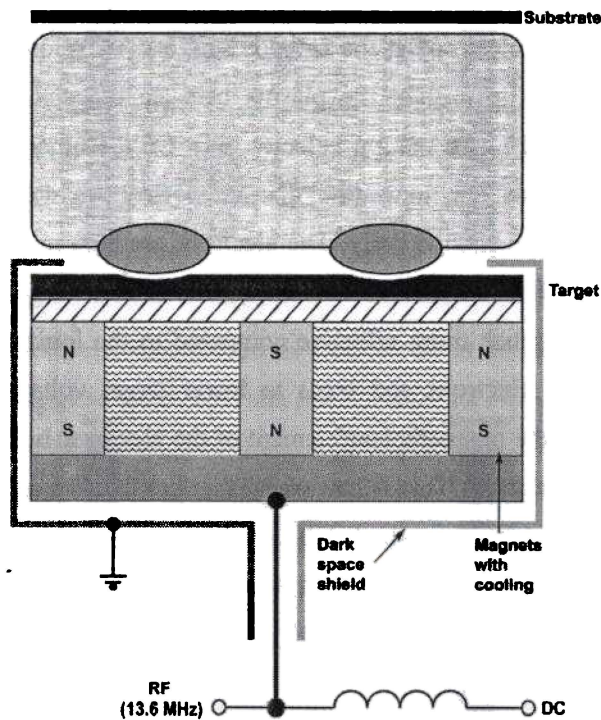


Fig.1. 3 Schematic diagram of magnetron sputtering configuration for RF and DC excitations.

For DC and RF excitation the potential distributions are shown schematically in figures 1.4 (a) and (b). Due to the different ionization mechanisms in DC and RF discharges, the potential distributions are significantly different for these two excitation modes. The discharge voltage, i.e. the negative DC voltage which is measured at the target, is much lower for RF compared to DC excitation. This large difference (up to a factor of seven at low power) is caused by different processes at the target and in the plasma body which govern the DC and the RF magnetron discharge [62, 63]. The DC discharge is based upon the generation of ion-induced secondary electrons at the cathode (target). Therefore, large target voltages are necessary to sustain the plasma because the electron emission increases almost linearly with the ion velocity [64]. On the other hand, the RF plasma is mainly driven by ionization due to electrons which perform an oscillating motion in the plasma body. The electrons are able to follow the RF frequency of 13.56 MHz while the ions are not, due to their large inertia. This kind of excitation is much more effective compared to the ionization by non-oscillating secondary electrons and leads to lower target voltages in an RF discharge. However, the magnetic confinement of the electrons is, by far, not as good as in the dc discharge. This is caused by the fact that during the positive half-cycle the target acts not as cathode but as anode.

Therefore, the plasma density in front of the substrate is significantly higher for RF compared to DC excitation. The sputtering yield S depends linearly on the ion energy [65]:

$$S = \text{const.}(E_{ion} - E_{thres}) = \text{const.}e(V_p - V_{dc} - V_{thres}) \quad (1.37)$$

Yamamura and Itoh [66] gave a semi-empirical formula for the sputtering threshold energy:

$$E_{thres} = 8U_s(M_1/M_2)^{2/5} \quad (1.38)$$

where, U_s is the surface potential barrier and $M_{1,2}$ are the mass numbers of the ion and the target, respectively.

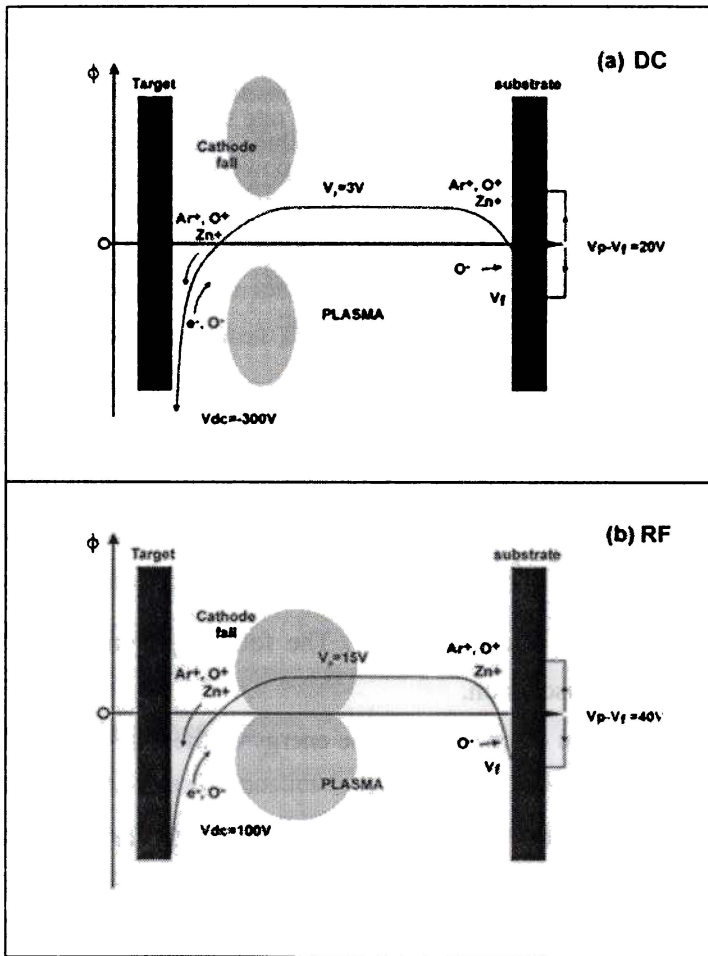


Fig.1. 4 (a) Potential distribution in (a) DC excited (b) RF excited magnetron sputtering discharge.

The low discharge voltages V_{dc} (for RF) lead to significantly lower deposition rates for an RF magnetron discharge compared to a DC sputtering process under the condition of constant discharge power. The deposition rate is proportional to the discharge power, as expected [67]. This property of a magnetron sputtering discharge is advantageous for the controlling of a sputter deposition process. The DC process yields deposition rates that are a factor of 1.5–2 higher than that for RF sputtering. For DC sputtering the deposition rate starts to increase from zero power. In the case of RF excitation a threshold power for sputtering of 10 W is observed, due to the low discharge voltages. The deposition rate R is proportional to S , the sputtering yield, and $I(1-\gamma)$, with I the discharge current and γ the secondary electron emission coefficient:

$$R = const. SI(1-\gamma) \quad (1.39)$$

Combining (1.37) and (1.39) one obtains,

$$R = const.eI(1-\gamma)(V_{ion} - V_{thres})$$

$$R = const.eP(1-\gamma) \left(1 + \frac{V_p - V_{thres}}{|V_{dc}|} \right) \quad (1.40)$$

where, P represents the discharge power. The following conclusions can be drawn from the above discussion.

- (i) The deposition rate is determined by the energy of the ions at the sputtering target.
- (ii) The energy of reflected argon atoms is higher for dc than for RF excitation.

Apart from the nonreactive gas [68] introduced in to the chamber for ignition of the plasma, in some cases a reactive gas is injected into the plasma, so the deposited material has different proportions of reacting atoms and sputtered material. This is the so-called reactive sputtering process [69]. The reactive

sputtering process is a very attractive method since in dependence on the reactive gas composition and partial pressure; layers with different chemical compositions and properties can be prepared. Furthermore, the deposition rates are generally enhanced in reactive sputtering. Ceramic compound targets are often too insulating to be sputtered by DC excitation. In this case RF power supplies have to be used, which are much more expensive than DC supplies.

In the schematic potential distributions shown in figures 1.4(a) and (b) is due to the sputtering of zinc oxide (ZnO) with argon gas in presence of reactive gas (oxygen). The positive ions (Ar^+ , O^+ , Zn^+) are accelerated in the cathode fall $V_p - V_{dc}$ towards the cathode, leading to the sputtering of the target. On the other hand, electrons and negative ions (O^-) move from the target to the substrate. Together with reflected neutral argon atoms energetic negative ions can reach the substrate and will influence the layer growth. In the case of the RF discharge however, the plasma torus is more extended towards the substrate [63] as schematically shown in figure 1.4(b). This is easily seen by visual inspection of a magnetron discharge excited by DC and RF. It causes a higher plasma density in front of the substrate for RF excitation and hence a higher ion saturation current to the growing film.

1.6 Plasma diagnostics

The objective of plasma diagnostics is to obtain the information about the state of plasma by means of experimental analysis of the physical processes occurring in it. The knowledge of plasma parameters is required to understand fully the effects of the physical processes taking place in the plasma and to deduce from them its properties. The diagnostic tools are classified into ex-situ and in-situ techniques. The ex-situ techniques sample the contents plasma reactor and

transfer a fragment of the contents outside the reactor for examination. Among the ex-situ or off-line that are used for the plasma diagnostics are mass spectrometry and gas phase electron paramagnetic resonance. Since the contents of a plasma reactor include many highly reactive species, one can never be certain that species analyzed ex-situ have not undergone changes during their transfer from the reactor.

The in-situ or on-line techniques can be further classified in to intrusive and nonintrusive methods. Any diagnostic technique is to some extent intrusive and perturbs the plasma. In some cases, this perturbation may be negligible, while in others it may be quite significant. The extent to which the perturbation is significant depends on the required information.

The most commonly used techniques for plasma diagnostics are mass spectrometry, optical methods and electric probes. Optical diagnostic techniques use photons to transmit information from the plasma to the detection tool and are the least intrusive in-situ plasma diagnostic methods. These include, optical emission spectroscopy (OES), laser induced fluorescence (LIF), laser absorption spectroscopy (LAS), laser interferometry etc. Apart from the number density and electron temperature the optical diagnostic techniques are capable of gathering qualitative and quantitative information of various species, their spatial and temporal behavior even in highly transient plasmas. The theory of OES applicable to laser induced plasma in the LTE regime is discussed in detail in the later section.

Variety of electric probes, viz, single, double, triple and ionic probes are in use in the plasma characterization. The electrostatic or Langmuir probes are suitable for measuring parameters of cold plasmas. This technique allows the determination of plasma density, N_e , electron temperature T_e , plasma potential

V_p , and floating potential V_f . The probes do not provide information on the chemistry of the plasma, but will serve in complimenting the information gathered from other diagnostic techniques. The theory of single cylindrical probe used in the characterization of RF magnetron plasma is discussed in detail in the section 1.6.2.

1.6.1 Optical emission spectroscopy (OES)

OES is one of the simplest, nonintrusive ways to investigate the initial phase of plasma dynamics since it uses intrinsic light emission from the LIP and does not require external excitation. This advantage makes the OES experimental setup very simple and adaptable to automation and remote sensing. Using OES one can obtain fundamental information about the plume by looking directly at the emission spectrum. Spectral information in its most sophisticated form can provide information on the plasma ionization balance, rate processes, and the densities and temperatures. However, estimation of different parameters of the plume using OES requires some assumptions, most importantly of which is the existence of local thermodynamic equilibrium (LTE) and optically thin plasma.

The issue of LTE in laser-produced plasmas has been discussed by several authors [70-73]. In a transient system, such as plasma formed by a pulsed laser source, the existence of LTE requires that the electron-atom and electron-ion collisional processes occur sufficiently fast and dominate radiative processes. In a system that is in LTE, particles will have Maxwellian velocity distributions, population levels will be distributed according to Boltzmann's statistics, ionization states will be described by Saha's equation, and the radiation density

will obey Planck's law as discussed in section 1.4 (ii). The validity can be confirmed by McWhirter criterion expressed by the inequality (1.29)

(i) Density measurement

One of the most powerful spectroscopic tools to determine plasma density with reasonable accuracy is by measuring the stark broadened line profile of an isolated atom or singly charged ion. There are various broadening mechanisms which are likely to contribute significantly to line widths observed in plasmas viz., natural broadening, Doppler broadening, instrument broadening, resonance pressure broadening and Stark broadening. Natural line broadening is significant only at low density plasma. For the plasma produced by the laser ablation in vacuum, where ablated species exhibit high expansion velocities, one of the dominant contributions to spectral line broadening is Doppler broadening, which is due to different Doppler shifts ($\Delta\lambda = \lambda V_z / c$) experienced by the species in different regions of the plume having different velocity components V_z in the direction of observation. The Doppler line widths full width half maximum (FWHM) for the expansion velocities of the $\sim 10^6$ cm s⁻¹, are less than 0.02 nm, for emission lines in the green region of the visible spectrum. The Doppler broadening which has Gaussian line profile, becomes more significant in low density plasma [7] and hence can be safely ignored in laser ablated plasma. Setting the spectrograph at its maximum resolution can minimize the instrumental broadening. The gas pressure broadening is generally not important in highly ionized plasmas such as those generated by lasers.

However in dense plasma, these line broadening mechanisms are negligible because the line shapes are strongly influenced by interaction of radiating atoms or ions with surrounding particles. The interactions are those between radiating

systems and plasma ions or electrons. Because of the presence of electric fields this type of broadening is called Stark broadening. The stark broadened line profile is Lorentzian [7] and has to be confirmed while making density measurements. Stark profiles allow the determination of electron densities in plasmas of almost any chemical composition, even if the latter is not well known.

The FWHM of the Stark broadened lines $\Delta\lambda_{1/2}$ (in Å) is related to the electron density by the expression: [7, 73]

$$\Delta\lambda_{1/2} = 2W\left(\frac{N_e}{10^{16}}\right) + 3.5A\left(\frac{N_e}{10^{16}}\right)^{1/4} \times \left(1 - \frac{3N_D^{-1/3}}{4}\right)W\left(\frac{N_e}{10^{16}}\right) \quad (1.41)$$

where, W is the electron impact parameter, which can be incorporated to different temperatures; A is the ion broadening parameter, and N_D , the number of particles in the Debye sphere. The first term on the right side of above equation represents the broadening due to electron contribution and the second term is the ion correction factor. For non-hydrogenic ions Stark broadening is predominantly by electron impact. Since the perturbations caused by ions are negligible compared to electrons, the ion correction factor can safely be neglected. Therefore, equation (1.41) reduces to,

$$\Delta\lambda_{1/2} = 2W\left(\frac{N_e}{10^{16}}\right)A^0 \quad (1.42)$$

For the electron number densities $N_e \geq 10^{15} \text{ cm}^{-3}$ the stark broadening will predominate over other line broadening mechanisms and the plasma will be sufficiently dense to satisfy the requirements of LTE.

(ii) Temperature measurements

The assumption of the existence of a temperature requires the presence of certain local equilibrium conditions that must exist in each small volume element of the plasma being examined. The direct technique for the determination of atom and ion temperature is the measurement of the thermal Doppler broadening of suitable lines. Nevertheless, this method encounters difficulties both at high pressure (because of pressure broadening) and high temperature (lack of resolution for the lines which are at short wavelengths). Among the various methods, relative line intensity measurements are the most used technique for laser ablated plasmas. This technique is based on the fact that densities of atoms in various states are proportional to the exponentials of the negative ratios between the excitation energy and the thermal energy kT (Boltzmann's law).

(a) Boltzmann plot method

The electron temperatures can be determined with good accuracy using Boltzmann plot method [7], under the assumption that the plasma is in the LTE regime. The electron temperature is determined the equation,

$$\ln\left(\frac{I_{mn}\lambda_{mn}}{A_{mn}g_{mn}}\right) = \ln\left(\frac{N}{Z}\right) - \left(\frac{E_m}{kT_e}\right) \quad (1.43)$$

for a transition from an upper state m to a lower state n , I_{mn} is the integral intensity of emission, λ_{mn} is the transition wavelength, A_{mn} is the transition probability, E_m and g_m are the energy and statistical weight of the upper level, respectively, k is the Boltzmann constant and T_e is the electron temperature. The temperature is obtained from the slope ($-1/kT_e$) of the plot of $\ln [(I_{mn}\lambda_{mn}/A_{mn}g_m)]$

versus E_m . The total number density N and the partition function Z are not required to determine the temperature.

(b) Relative intensities of line from the same element and ionization state

The oldest method for the determination of temperature in LTE plasmas is based on the fact that densities in various excited states are proportional to the products of statistical weights with the exponentials of the negative ratios of excitation energy and the thermal energy kT_e [7, 73]. The temperature is accordingly inversely proportional to the logarithm of the ratio of the total intensities of lines arising from different upper levels, provided that none of the lines is affected by self absorption. Hence kT_e is given by

$$kT_e = \frac{E' - E}{\ln \left(\frac{I \lambda^3 g' f'}{I' \lambda'^3 g f} \right)} \quad (1.44)$$

where, I , λ , g and f are total integral intensity (integrated over the profile), wavelength, statistical weight (of the lower state of the line), and absorption oscillator strength respectively, of the particular emission line and E is the excitation energy. The primed quantities correspond to the other line and k is Boltzmann constant and T_e , the electron temperature. Since the difference between E' and E can be small, the accuracy of this method can be poor. To circumvent this problem one can resort to the determination of relative intensities of lines from the same element but from successive ionization stages.

(c) Relative line intensities of subsequent ionization stages of the same element

The reason for the discrepancies in the evaluation of electron temperature, as described in the previous section is due the relatively small separation between the upper levels of the two lines, which is normally not much larger than typical thermal energies or may be smaller. This renders the line intensity ratio rather insensitive to temperature changes. The improvement in the sensitivity is obtained by selecting two emission lines of the same element but due to successive ionization states. In this case the effective energy difference is enhanced by the ionization energy, which larger than the thermal energies of plasma in LTE. The ratio of such line intensities follows,

$$\frac{I'}{I} = \frac{f' g' \lambda^3}{f g \lambda^3} (4\pi^{3/2} a_0^3 N_e)^{-1} \left(\frac{kT_e}{E_H} \right) \exp\left(-\frac{E' + E_\infty - E - \Delta E_\infty}{kT_e} \right) \quad (1.45)$$

The primed quantities correspond to higher ionization state, and ΔE_∞ is the reduction factor of ionization energy E_∞ of the lower ionization state. E_H is the ionization energy of hydrogen atom, a_0 is the Bohr radius and E the excitation energy. The correction factor in the ionization energy is given by,

$$\Delta E_\infty = 3z \frac{e^2}{4\pi\epsilon_0} \left(\frac{4\pi N_e}{3} \right)^{1/3} \quad (1.46)$$

Where, $z=1$ for neutral atoms, $z=2$ for singly ionized species, etc.

The plasma produced by the ablation of conducting, semi-conducting and insulator targets using various laser sources have been characterized [31,71, 72, 74-79] by the OES technique described above.

1.6.2 Theory of Langmuir probe

A Langmuir probe provides information on the charged particle density, plasma (space) potential, as well as electron temperature [9-22, 80-82]. The probe consists of basically a metal tip, which measures the current of charged particles at various probe potential. From the curve of the collected current I versus the probe potential V , i.e. the probe characteristic curve, the relevant quantities can be derived. However, in the case of magnetron plasma, the relation between the shape of this curve and the plasma properties is not straight forward due to the presence of strong magnetic field. In this case, since the electrons are trapped by the magnetic field near the cathode, the electronic current collected by the probe is lower than that obtained without magnetic field. This effect becomes more important when the quantity $\beta = r_p/r_L$, with r_p the probe tip radius and r_L the electron Larmour radius, reach value above unity. Moreover, a typical exponential fit to the probe characteristic curve gives overestimated values of electron temperature [83, 84]. Some reports have appeared in the literature trying to solve this problem [85-88], and one of the best solution is the introduction of an upper cut-off voltage V_c above which all curve points are not taken into account in fitting procedure. This voltage is located between the plasma and floating potential, and is chosen using the minimum electron temperature criterion [86].

The probe current is dependent on the potential imposed on the probe. A typical current voltage plot is shown in Figure 1.5. This characteristic is normally determined by the plasma properties in the immediate vicinity of the probe [11,89,90].The general shape of the I - V characteristic can be divided into three parts. When the probe is biased positively with respect to the local plasma potential the flux of particles reaching the probe will consist of carriers of

negative charge (normally electrons). This region is called the electron accelerating region and is labeled as III in Figure 1.5. These electrons will be collected from a region called the sheath, which is the region close to the probe surface where the potential exerted by the probe is not shielded by the plasma. When the probe is biased at a potential slightly smaller than the plasma potential only particles with enough energy to overcome the potential barrier will be collected. This region (region II in Fig. 1.5) is called the electron retarding region.

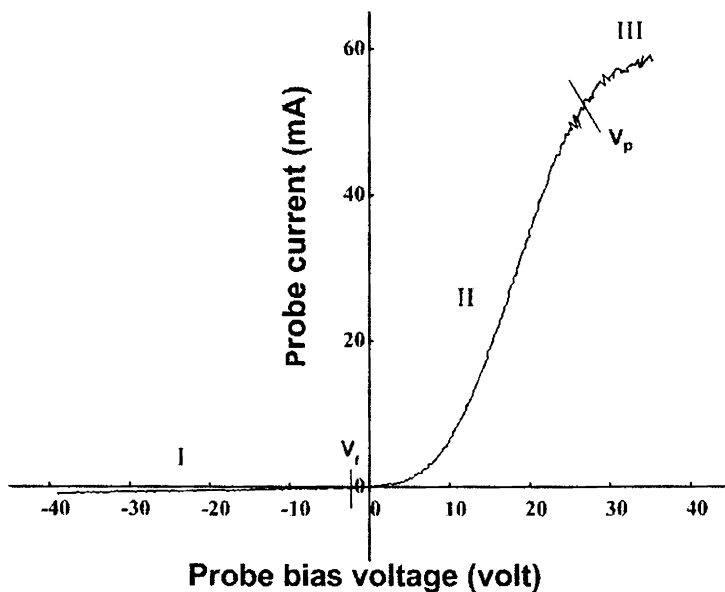


Fig 1.5 Typical current voltage plot, V_s and V_f represents the plasma (space) potential and floating potential respectively.

The last region is accessed when the probe is biased increasingly negative relative to the plasma potential. In this region (region I in Figure 1.5) only positive ions will reach the probe. This region is called the ion saturation region. The governing theories applicable to these three regions in the I - V plot are discussed in the remainder of this section. The electron-retarding region (region II) is the easiest to describe and will be discussed first. In this region the probe actually acts as an energy selector, collecting only those electrons which have sufficient kinetic energy to overcome the potential barrier.

If the electron distribution is in local thermal equilibrium, the electron energy distribution function can be assumed to be Maxwellian and the current drawn in this regime follows the relation [90]

$$I_e = N_e e A \left(\frac{kT_e}{2\pi m_e} \right)^{1/2} \exp\left(\frac{e(V - V_p)}{kT_e} \right) \quad (1.47)$$

where I_e is the electron current, N_e the electron number density, e the electron charge, A the probe area, k the Boltzmann constant, T_e the electron temperature and m_e the electron mass. The gradient of a plot of $\ln(I_e)$ versus the applied voltage, V , yields the electron temperature.

$$\frac{\partial \ln(I_e)}{\partial V} = \frac{1}{T_e} \quad (1.48)$$

The knowledge of the electron current at the plasma potential, substitution of T_e in equation (1.47) yields to the electron number density.

The electron acceleration region (III) is governed by the orbital motion theory, and an expression for the electron current in this region can be derived as follows: consider a point charge at a bias potential V_b , separated from an electron with charge e at some point where the potential is V_p . Assume that the electron

has a forward trajectory, with velocity v_0 and impact parameter p as defined in figure 1.6.

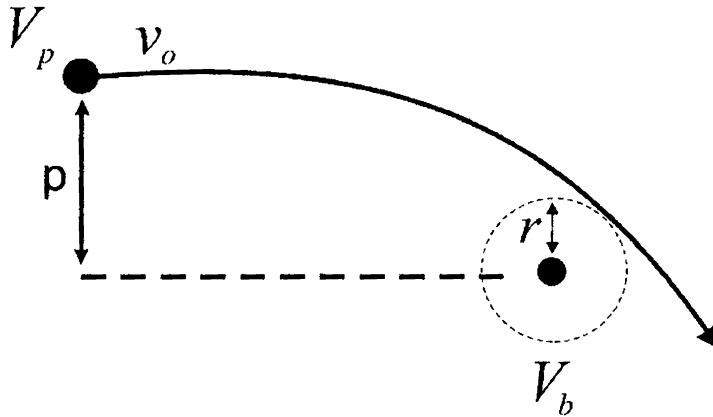


Fig.1.6. Schematic of the input for the orbital motion theory.

The total kinetic energy T of the particle at any time during its trajectory is given by:

$$T = \frac{1}{2} m \left[v^2 + r^2 \left(\frac{d\psi}{dt} \right)^2 \right] \quad (1.49)$$

Where, the two terms on the right hand side of Eq. (1.49) are, respectively, the translational and the rotational parts of the total kinetic energy. Given that (conservation of angular momentum):

$$\frac{d\psi}{dt} = \frac{pv_0}{r^2} \quad (1.50)$$

we can rewrite the expression (1.49) as:

$$T = \frac{1}{2}mv^2 + T_0 \frac{p^2}{r^2} \quad (1.51)$$

Given equation (1.51), we can rewrite the total energy of the system as:

$$E_T = \frac{1}{2}mv_0^2 - eV_p = \frac{1}{2}mv^2 + T_0 \frac{p^2}{r^2} - eV \quad (1.52)$$

At the point of closest distance to the probe (r_c), the translational kinetic energy is totally converted into centrifugal energy ($v = 0$), thus the total energy expression (1.52) can be rewritten as:

$$\frac{1}{2}mv_0^2 - eV_p = T_0 \frac{p^2}{r_c^2} - eV_c \quad (1.53)$$

Rearranging expression (1.53) gives:

$$p = r_c \left[1 - \frac{e(V_c - V_p)}{T_0} \right]^{1/2} \quad (1.54)$$

Taking r_c as the probe radius a , any particle with $p < a [1 + (V_c - V_p)/T_0]^{1/2} = p_a$ will be collected. The expression for the current collected by a cylindrical probe given a Maxwellian electron velocity distribution can also be derived [analogous to Eq. (1.47)]. It takes the form:

$$I_e = N_e e A \left(\frac{kT_e}{2\pi m_e} \right)^{1/2} \frac{2}{\sqrt{\pi}} \left(1 - \frac{e(V - V_p)}{kT_e} \right)^{1/2} \quad (1.55)$$

The ion saturation current region I_i is a more difficult region to describe. The amount of ion current is governed by the Bohm criterion, since the ion temperature is much lower than the electron temperature in the plasmas under consideration. The Bohm criterion states that the ion velocity must acquire a positive (towards the probe) velocity at the plasma sheath edge even when the ions have very low temperatures. This velocity is provided by the existence of a

“pre-sheath” potential drop that occurs at long distances in the plasma. The ion current is thus dependent on the electron temperature. There are a number of assumptions which are inherent in the analysis of probe data including that plasma is collisionless, electron energy distribution is Maxwellian, the ions are singly charged and that ion and electron densities are equal ($N_i = N_e$ defining plasma density).

The ion saturation portion of the characteristic is used to determine the ion density. The expression for ion current drawn by the probe [91] derived similarly is,

$$I_i = \frac{Ae^{3/2}N_i}{2\sqrt{\pi}} \left(\frac{3kT_e}{m_i} \right)^{1/2} \left(1 - \frac{(V - V_p)}{kT_e} \right) \quad (1.56)$$

Where, m_i is the ion density. In the absence of any electron current, the probe current should be a function of the square root of the probe potential. The derivative of I_i^2 with respect to V gives,

$$\frac{\partial I_i^2}{\partial V} = - \frac{3A^2 e^3 N_i^2}{4\pi m_i} \quad (1.57)$$

When the probe current squared is plotted against sufficiently negative probe bias voltage a straight line results, and the slope of that line is used to calculate the ion density.

$$N_i^2 = - \frac{4\pi m_i}{3A^2 e^3} \left(\frac{\partial I_i^2}{\partial V} \right) \quad (1.58)$$

The final plasma parameter which may be determined from the probe characteristic is the floating potential V_f . It is the potential at which the ion current is equal to the electron current. This is the potential which would be acquired by an insulated substrate placed in to the plasma. This is the simplest of

the probe parameter to acquire and is often useful in determining the plasma potential in the event when the ion saturation region is not obtained in the characteristic. Since the difference between V_f and V_p is related to electron temperature [2] by the approximate relation [9],

$$V_p = V_f - \frac{kT_e}{e} \left[\frac{1}{2} \ln \left(\frac{\pi m_i}{2m_e} \right) \right] \quad (1.59)$$

The above expressions are strictly only valid in collisionless sheath conditions (i.e. when the mean free path $\lambda >$ sheath dimensions). Higher order corrections have to be included in the expressions in situations where collisions occur within the plasma sheath.

(a) Practical complications

Real probe measurement is much more complex, for a variety of reasons. The effective current-collecting area of the probe is not its geometric surface area, but rather the area of the interface between the plasma and sheath around the probe; and the thickness of the sheath, for a given plasma, is a function of the probe potential. The probe should be small, so that the probe current does not constitute a significant drain on the plasma. With a cylindrical probe, the varying sheath thickness is an even larger effect [2, 3].

Two more complications are associated with additional charge generation. Secondary electrons may be generated at the probe due the direct impact of ions, electrons and photons or the heating effects caused by such impact, giving rise to additional current flow; electron impact ionisation may occur in the sheath, again enhancing current flow.

Yet one more problem concerns the tendency of charged particles to take up orbital path around the probe, further influencing the probe characteristics. In the

glow discharges arising in sputtering and plasma etching, there are additional difficulties due to directed high-energy electrons which flow through plasma. However, the Langmuir probe technique has been successively applied with different innovative methods on variety of plasma sources including RF and DC magnetron, microwave, electron cyclotron resonance, laser induced plasmas [9-31] over many decades to derive the plasma parameters with the help of which plasma processing and control over the plasma were realized.

1.7 ZnO: Optoelectronic importance

Zinc oxide (ZnO) is nontoxic, abundant, and therefore, relatively cheap. It has a wide direct band gap (3.37 eV) and a reasonably large piezoelectric coefficient. These properties have encouraged investigations of its possible use in surface acoustic wave (SAW) devices such as resonators, filters and waveguides [92–95]. Films of ZnO generally exhibit *n*-type semiconduction, the conductivity of which can be improved and stabilized (at high temperature) by judicious doping with, for example, Al or Ga [96–98]. This property, together with the broad optical transparency, has prompted extensive investigation of such films as transparent electrodes in flat-panel displays, thin-film transistors, and solar cells. Arsenic incorporation, resulting in *p*-type doped ZnO, has also been demonstrated [99] thus initiating the possibility of *p* – *n* junctions based on ZnO [100]. ZnO films exhibit up to three separate luminescence bands—in the ultraviolet (UV) and the green and yellow regions of the electromagnetic spectrum. The UV emission is associated with direct recombination of photo-generated charge carriers (exciton emission),[101] but unraveling the mechanisms contributing to the visible emissions remains a subject of active research [101,102]. UV lasing, at room temperature, from both films [103,104]

and nanotubes [105] of ZnO on sapphire has been reported. ZnO polycrystalline thin films and powders act as disordered dielectric media where lasing originates from the random scattering in the medium. [106]. There are reports of random lasing even with low density of ZnO nanorods [107], where strong transverse confinement of light inside ZnO is achieved by depositing MgO buffer layer over ZnO nanorods.

ZnO films can also show a large enough second-order nonlinear optical response to support second-harmonic generation [108]. Although polymeric materials show high third order optical nonlinearity [109], in subpicosecond time scale and find applications in all optical switching devices, [110] they are prone to degradation due to thermal and aging effects. However inorganic materials, such as ZnO, with high melting point (2248 K) and response to nonlinear optical effects make it a suitable choice. All the ZnO films provide excellent UV shielding due to the absorption edge on the short wavelength side ($\lambda \sim 300$ nm). Apart from this, high reflectance in the IR region can make this film a good candidate for application as the coating for heat reflectors. ZnO possess high excitonic binding energy (60 meV) and higher radiation hardness compared to other materials. Due to high melting point ZnO can withstand high annealing temperature and treatment processing associated with doping and contact formation. It also implies that ZnO based devices would not degrade fast due to low defect generation and would comparatively last longer. The versatility of ZnO listed above prompted active research in the last two decades based on thin film deposition of this material in its pure form or in combination with suitable material for specific device fabrication.

ZnO thin films have been grown by a variety of methods, including radio-frequency (RF) and direct-current (DC) sputtering, [97,102] chemical vapor

deposition, [94] spray pyrolysis, electron cyclotron resonance-assisted molecular beam epitaxy, and pulsed laser deposition (PLD) [96,101,109]. Among these techniques RF magnetron sputtering and PLD have generated wide popularity in the deposition of ZnO films. The former for its relatively low cost in the commercial synthesis of thin films over other methods and the later for its superior quality of film deposition and flexibility in the manipulation of input parameters for plasma production. The input parametric variables in PLD with and without added dopant atoms with ZnO, are the laser excitation wavelength, fluence and pulse duration in vacuum and in various reactive or nonreactive ambient gas pressures as a function of substrate material and substrate temperature. For example there are reports of ZnO thin films with p-type conductivity when doped with gallium and ablated in N₂O or NH₃ ambience [111].

1.8 Review of ZnO plasma studies

In contrast to the extensive literature relating to ZnO films produced by PLD and their properties, there appears to have been relatively little effort directed towards characterization of the ablation plume from which such films are produced. Few reports on the characterization of laser ablated and RF sputtered ZnO plasmas are available [19,31,112-115]. The idea of plasma characterization is to assist in the optimization of the deposition conditions favorable for the type of thin films of specific use. Most of the LIP characterizations are based on ablation of ZnO target with excimer laser which are having large pulse width [112-114]. The spatial evolution of electron density, electron temperature and spectral emission intensity has not been reported for laser ablated ZnO plasma.

Kilini et al [112] have reported the comparison of LIP characteristics of ZnO plasma generated by the ablation with nano second (KrF) and femto second (XeCl) excimer lasers at low fluence (1.7 J cm^{-2}) and at oxygen ambient pressure range 5×10^{-5} to 5×10^{-3} mbar. The velocities of the species were higher in plasma obtained in femto second ($13.0 \pm 0.5 \text{ km s}^{-1}$ for Zn I) compared to nano second ($10.3 \pm 0.5 \text{ km s}^{-1}$) laser ablation. The velocity of Zn II ($33.4 \pm 0.5 \text{ km s}^{-1}$) was highest among other species in the plume. This is found to be the general phenomenon in LIP irrespective of the type of laser and fluences. The smoother films were reported to be deposited at 300°C to 400°C at 0.001 mbar oxygen pressure while better crystallinity was found obtained at 650°C . The result of the present work on the ZnO plasma and growth film is in agreement with results of Kilini et al [112].

Acquaviva et al [113] have reported optical emission spectroscopic investigations on the plasma ablated (fluence = 8 Jcm^{-2}) of Zn and ZnO targets in KrF excimer laser in vacuum and at very high oxygen gas (10 mbar and 50 mbar) pressure. The emissions corresponding to the UV and green photoluminescence bands of the zinc oxide have been reported. The study of the temporal evolution of ejected atomic and ionic species by space- and time-resolved spectroscopy shows a higher velocity for the species at higher ambient pressure which is contrary to other reports and the present work.

Claeysens et al [114] have carried out an extensive investigation of the plume of ZnO target ablated by 193 nm laser (ArF laser with fluence variation up to 20 Jcm^{-2}) in vacuum. The plume dynamics was studied using wavelength and spatially resolved optical emission spectroscopy and Langmuir probes. The emission intensity of the ablated species exhibited a linear increase with laser fluence. The Zn II registered highest velocity of 31 km /s . The Langmuir probe

measurements showed ions acquiring velocities comparable with the velocity of fast electrons.

The spatial variation of electron temperature, electron density and emission intensity variations of the species in the laser (Nd:YAG, wave length 355 nm) ablated pristine ZnO, which is the PART-I of Chapter III of this thesis, has been reported [31]. Thareja et al [115] studied the temporal evolution of specific emissions at various ambient gas pressures. Zn II emission intensities were found to increase with ambient oxygen gas pressure. The temporal spread of the intensities of species has been found to increase with pressure. Large oxygen pressure (100 mTorr and 900 mTorr) and high laser intensity 2.04×10^{10} W/cm² were used in the investigation which yielded the electron density values in the range of 10^{19} cm⁻³ and electron temperature about 3.6 eV. The velocities of species were calculated of the order of 10^6 cm/sec. These values of plasma parameters are a slightly large compared to the ones obtained in the present work owing to the low laser fluence, ambient gas composition and pressure employed in this work. Namba et al [116] have reported the plasma parameters, such as electron temperature and electron density, were deduced from continuum and line spectra recorded during and immediately after a laser irradiation (up to 140 ns temporal delay). In addition, the expansion velocities of ions and atoms were determined by time-of-flight transients of the emission spectra. Nd:YAG, (355 nm) at 4.5 J/cm² laser fluence was employed in ablating pure ZnO target and the oxygen pressure varied up to 10 mTorr.

The spectroscopic and Langmuir probe analysis of RF plasma generated using xenon and argon sputtering gases in reactive oxygen ambience has been studied [19] with regard to film deposition. The electron density reported is in the 10^{11} cm⁻³ order in accordance with the present work, while the electron temperature

(~15 eV) and plasma potential (~40 V) are very high due to the low electron current observed by Nagata et al [19].

References

- [1] F. F. Chen and J. P. Chang, *Lecture Notes on Principles of Plasma processing*, Kluwer Academics/ Plenum Publishers, New York (2003).
- [2] Brian Chapman, *Glow Discharge Processes-Sputtering and Plasma Etching*, John Wiley & Son, New York (1980).
- [3] R. H. Huddlestone and S. S. Leonard, *Plasma Diagnostic Techniques*, Academic Press, London (1965).
- [4] I. I. Sobelman, L. A. Vainshtein, and E. A. Yakov, *Excitation of Atoms and Broadening of Spectral lines*, 2nd Edition, Springer (1995).
- [5] I. H. Hutchinson, *Principles of Plasma Diagnostics*, 2nd Edition, Cambridge University press, U. K. (2002).
- [6] R. W. P. Whirter, "Spectral Intensities" in *Plasma Diagnostic Techniques*, R. H. Huddlestone and S. L. Leonard, Eds. Academic Press, New York, (1965).
- [7] H. R. Griem, *Plasma Spectroscopy*, p 148, Mc Graw Hill, New York, (1964).
- [8] R. Wilson, *J. Quant. Spectr. Radiative Transfer*, **2**, 477 (1962).
- [9] A. Palmero, E. D. van Hattum, W. M. Arnoldbik, A. M. Vrendenberg, and F. H. P. M. Habraken, *J. Appl. Phys.* **95**, 7611 (2004).
- [10] A. A. Shatas, Y. Z. Hu, and E. A. Irene, *J. Vac. Sci. Technol. A*, **10**, 3119 (1992).
- [11] J. E. Heidenreich III, J. R. Paraszczak, M. Moisan, and G. Sauve, *J. Vac. Sci. Technol. B*: **5**, 347 (1987).
- [12] S. Sunil, A. Kumar, R. K. Singh, and K. P. Subramanian, *J. Phys. D: Appl. Phys.* **41**, 085211 (2008).

- [13] M. Nisha, K. J. Saji, R. S. Ajimsha, N. V. Joshy, and M. K. Jayaraj, *J. Appl. Phys* **99**, 033304 (2006).
- [14] N. V. Joshy, J. Isaac, and M. K. Jayaraj, *J. Appl. Phys* (in press).
- [15] R. M. Clements, *J. Vac. Sci. Technol. A*: **15**, 193, (1978).
- [16] Y. Ohtsu, H. Matsuo, and H. Fugita, *Plasma Sources Sci. Technol.* **5**, 344 (1996).
- [17] S-H. Seo and H-Y. Chang, *J. Appl. Phys.* **96**, 1310 (2004).
- [18] J. Hopwood, C. R. Guarnieri, S. J. Whitehair, and J. J. Cuomo, *J. Vac. Sci. Technol. A*: **11**, 152 (1993).
- [19] T. Nagata, A. Ashida, N. Fujimura, and T. Ito, *J. Appl. Phys.* **95**, 3923 (2004).
- [20] K. D. Varghese and G. M. Rao, *Rev. Sci. Instr.* **77**, 467 (2000).
- [21] S. M. Gorbatkin, L. A. Berry, and J. B. Roberto, *J. Vac. Sci. Technol. A* **8**, 2893 (1990).
- [22] E. V. Shunko, *J. Appl. Phys.* **93**, 3729 (2003).
- [23] J. Sheffield, *Plasma Scattering of Electromagnetic Radiation*, Academic Press, New York (1975).
- [24] V. Bulatov, L. Xu, and I. Schechter, *Anal. Chem.* **68**, 2966 (1996).
- [25] A. V. Bulgakov and N. M. Bulgakova, *J. Phys. D*: **28**, 1710 (1995).
- [26] J. J. Chang and B. E. Warner, *Appl. Phys. Lett.* **69**, 473 (1996).
- [27] P. E. Dyer, A. Issa, and P. H. Key, *Appl. Phys. Lett.* **57**, 186 (1990).
- [28] J. Gonzalo, C. N. Afonso, and I. Madariaga, *J. Appl. Phys.* **81**, 951 (1997).
- [29] S. S. Harilal, C. V. Bindhu, V. P. N. Nampoori, and C. P. G. Vallabhan, *Appl. Phys. Lett.* **72**, 167 (1998).
- [30] A. A. Voevodin, J. G. Jones, J. S. Zabinski, and L. Hultman, *J. Appl. Phys.* **92**, 724 (2002).

- [31] K. J. Saji, N. V. Joshy, and M. K. Jayaraj, *J. Appl. Phys.* **100**, 043302 (2006).
- [32] D. Bauerle, *Laser Processing and Chemistry*, 3rd Ed. Springer, Berlin, (2000).
- [33] R. F. Wood and G. E. Giles, *Phys. Rev. B*: **25**, 2923 (1981).
- [34] R. K. Singh and J. Narayan, *Mat. Sci. Engng B*: **3**, 217 (1989).
- [35] A. Peterlongo, A. Miotello, and R. Kelly, *Phys. Rev. E*: **50**, 4716 (1994).
- [36] S. Amoruso, R. Bruzzese, R. Velotta, N. Spinelli, and X. Wang, *Appl. Surf. Sci.* **138**, 250 (1999).
- [37] H. S. Carslow and J. C. Jaeger *Conduction of Heat in Solids* (Oxford: Oxford University Press) (1959).
- [38] J. F. Ready *Effects of High-Power Laser Radiation*: Academic Press, New York (1971).
- [39] P. R. Willmott and J. R. Huber, *Rev. Mod. Phys.* **72**, 315 (2000).
- [40] R. Kelly and R. W. Dreyfus, *Nucl. Instrum. Methods B*: **32**, 341 (1988).
- [41] R. K. Singh and J. Narayan, *Phys. Rev. B*: **41**, 8843 (1990).
- [42] R. K. Singh, O. W. Holland, and J. Narayan, *J. Appl. Phys.* **68**, 233 (1990).
- [43] Y. B. Zeldovich and Y. P. Raizer, *Physics of Shock Waves and High-Temperature Hydrodynamic Phenomena*, Dover, Mineola, New York, (2001).
- [44] C. R. Phipps and R. W. Dreyfus, in: *Laser Ionization Mass Analysis*, Eds. A. Vertes, R. Gijbels, and F. Adams, *Chemical Analysis Series 124*, Wiley, New York, (1993).
- [45] S. I. Anisimov, D. Bäuerle and B. S. Luk'yanchuk, *Phys. Rev. B*: **48**, 12076 (1993).

- [46] S. I. Anisimov, B. S. Luk'yanchuk, and A. Luches, *Appl. Surf. Sci.* **96**, 24 (1996).
- [47] A. Amoruso, B. Toftmann, J. Schou, R. Velotta, and X. Wang, *Thin Solid Films* **453**, 562 (2004).
- [48] J. Musil and J. Vlcek, *Mater. Chem. Phys.* **54**, 116 (1998).
- [49] M. Brenda and J. Musil, *Vacuum* **55**, 171 (1999).
- [50] J. Kong, H. Shen, B. Chen, Z. Li, W. Shi, W. Yao, and Zh. Qi, *Thin Solid Films* **207**, 51 (1991).
- [51] J. Musil, A. J. Bell, M. Cepera, and J. Zeman, *Surf. Coat. Technol.* **96**, 359 (1997).
- [52] A.S. Asha, M.T. Sebastian and M.K. Jayaraj, *J. Alloys and Comp.* **449**, 68 (2008).
- [53] R. Manoj, M. Nisha, K. A. Vanaja, and M. K. Jayaraj, *Bull. Mat. Sci.* **31**, 49 (2008).
- [54] L. Akkad, A. Punnose, and J. Prabu, *J. Appl. Phys.* **A 71**, 157 (2000).
- [55] L. Pekker, *Thin Solid Films* **312**, 341 (1998).
- [56] A. Palmero, N. Tomozeiu, A. M. Vredenberg, W. Arnoldbik, and F. H. P. M. Habraken, *Surf. Coat. Technol.* **177**, 215 (2004).
- [57] M. Nisha, S. Anusha, A. Antony, R. Manoj and M. K. Jayaraj, *Appl. Surf. Sci.* **252**, 1430 (2005).
- [58] K. M. Krishna, G. Anoop and M. K Jayaraj, *J. Electrochem. Soc.* **154**, J379 (2007).
- [59] F. M. Penning, *Physica*, **3**, 873 (1936).
- [60] J. A. Thornton and A.S. Penfold *Thin Film Processes*, ed J. L. Vossen and W Kern (New York: Academic), 75 (1978).
- [61] R. K. Waits, *J. Vac. Sci. Technol.* **15**, 179 (1978).

- [62] J. A. Thornton, *J. Vac. Sci. Technol.* **15**, 171 (1978).
- [63] G. Y. Yeom and M. J. Kushner, *J. Appl. Phys.* **65**, 3816 (1989).
- [64] W. O. Hofer, *Scan. Microsc. Suppl.* **4**, 265 (1990).
- [65] M. P. Seah, *Thin Solid Films* **81**, 279 (1981).
- [66] Y. Yamamura and N. Itoh, *Ion Beam Assisted Film Growth*, ed T. Itoh (Amsterdam: Elsevier) 59 (1989).
- [67] A. R. Nyaiesh and L. Holland, *Vacuum* **31**, 315 (1981).
- [68] D. L. Smith, *Thin-film deposition*, Mc Graw – Hill Inc, Washington D. C. (1995).
- [69] N.Tomozeiu, , E.E. van Faassen, A. Palmero, W.M. Arnoldbik, A.M.Vredenberg, and F.H.P.M. Habraken, Intern. Conf. “*Metallurgical coating and thin films*”, San Diego, U.S.A. (2003).
- [70] H. R. Griem, *Principles of Plasma Spectroscopy*, Cambridge, New York, (1997).
- [71] E. P. Tijerina, J. Bohigas, and R. Machorro, *J. Appl. Phys.* **90**, 3192 (2001).
- [72] O. Barthelemy, J. Margot, S. Laville, F. Vidal, M. Chaker, B. Le Drogoff, T. W. Johnston, and M. Sabsabi, *Appl. Spectrosc.* **59**, 529 (2005).
- [73] G.Bekefi, *Principles of Laser Plasma*, Wiley, New York (1976).
- [74] C. Colon, G. Hatem, E. Verdugo, P. Ruiz, and J. Campos, *J. Appl. Phys.* **73**, 4752 (1993).
- [75] A. H. Galmed and M. A. Harith, *Appl. Phys. B – Lasers and Optics*, DOI: 10.1007/s00340-008-2971-0
- [76] N. M. Shaikh, B. Rashid, S. Hafeez, Y. Jamil, and M. A. Baig, *J. Phys. D: Appl. Phys.* **39**, 1384 (2006).
- [77] S. S. Harilal, C. V. Bindhu, R. C. Isaac, V. P. Nampoorei, and C. P. G. Vallabhan, *J. Appl. Phys.* **82**, 2140 (1997).

- [78] M. Ying, Y. Xia, Y. Sun, M. Zhao, Y. Ma, X. Liu, Y. Li, and X. Hou, *Laser and Particle Beam*, **21**, 97, (2003).
- [79] M. Ying, Y. Xia, Y. Sun, Q. Lu, M. Zhao, and X. Liu, *Appl. Surf. Sci.*, **207**, 227 (2003).
- [80] B. Fritsche, T. Chevolleau, J. Kourtev, A. Kolitsch, and W. Moller, *Vacuum*, **69**, 139 (2003).
- [81] P. Spatenka, J. Vlcek, and J. Blazek, *Vacuum* **55**, 165 (1999).
- [82] D. J. Field, S. K. Dew, and R. E. Burrell, *J. Vac. Sci. Technol. A*: **20**, 2032 (2002).
- [83] J. A. Tagle, P. C. Stangeby, and S. K. Erents, *Plasma Phys. Controlled Fusion* **29**, 297 (1987).
- [84] D. Buchenauer and A. W. Molvik, *Rev. Sci. Instrum.* **59**, 1887 (1988).
- [85] B. W. Koo, N. Hershkowitz, and M. Sarfaty, *J. Appl. Phys.* **86**, 1213 (1999).
- [86] M. Bagatin, D. Desideri, E. Martines, G. Manduchi, G. Serianni, and V. Antoni, *Rev. Sci. Instrum.* **68**, 365 (1997).
- [87] D. Desideri and G. Serianni, *Rev. Sci. Instrum.* **69**, 2354 (1998).
- [88] M. Spolaore, V. Antoni, M. Bagatin, A. Buffa, R. Cavazzana, D. Desideri, E. Martines, N. Pomaro, G. Serianni, and L. Tramontin, *Surf. Coat. Technol.* **116**, 1083 (1999).
- [89] B. E. Cherrington, *Plasma Chemistry and Plasma Processing*, **2**, 113 (1982).
- [90] N. Hershkowitz, in *Plasma Diagnostics, Volume 1, Discharge Parameters and Chemistry* (eds. O. Auciello and D. L. Flamm), Academic Press, London (1989).
- [91] F. F Chen, *J. Appl. Phys.* **36**, 675 (1964).

- [92] J. Kioke, K. Shimoe, and H. Ieki, *Jpn. J. Appl. Phys., Part 1* **32**, 2337 (1993).
- [93] M. Kadota and M. Minakata, *IEEE Trans. Ultrason. Ferroelectr. Freq. Control* **42**, 345 (1995).
- [94] C. R. Gorla, N. W. Emanetoglu, S. Liang, W. E. Mayo, Y. Lu, M. Wraback, and H. Shen, *J. Appl. Phys.* **85**, 2595 (1999).
- [95] T. Shiosaki, S. Ohnishi, Y. Hirokawa, and A. Kawabata, *Appl. Phys. Lett.* **33**, 406 (1978).
- [96] M. Hiramatsu, K. Imaeda, N. Horio, and M. Nawata, *J. Vac. Sci. Technol. A* **16**, 669 (1998).
- [97] H. Kim, C. M. Gilmore, J. S. Horwitz, A. Pique', H. Murata, G. P. Kuhsto, R. Schlaf, Z. H. Kafafi, and D. B. Chrisey, *Appl. Phys. Lett.* **76**, 259 (2000).
- [98] M. Chen, Z. L. Pei, X. Wang, C. Sun, and L. S. Wen, *J. Mater. Res.* **16**, 2118 (2001).
- [99] Y. R. Ryu, S. Zhu, D. C. Look, J. M. Wrobel, H. M. Jeong, and H. W. White, *J. Cryst. Growth* **216**, 330 (2000).
- [100] Y. R. Ryu, W. J. Kim, and H. W. White, *J. Cryst. Growth* **219**, 419 (2000).
- [101] X. W. Sun and H. S. Kwok, *J. Appl. Phys.* **86**, 408 (1999).
- [102] B. Lin, Z. Fu, and Y. Jia, *Appl. Phys. Lett.* **79**, 943 (2001).
- [103] D. M. Bagnall, Y. F. Chen, Z. Zhu, T. Yao, S. Koyama, M. Y. Shen, and T. Goto, *Appl. Phys. Lett.* **70**, 2230 (1997).
- [104] P. Yu, Z. K. Tang, G. K. L. Wong, M. Kawasaki, A. Ohtomo, H. Koinuma, and Y. Segawa, *J. Cryst. Growth* **184**~~05~~**5**, 601 (1998).
- [105] M. H. Huang, S. Mao, H. Feick, H. Q. Yan, Y. Y. Wu, H. Kind, E. Weber, R. Russo, and P. D. Yang, *Science* **292**, 1897 (2001).

- [106] A. Mitra and R. K. Thareja, *J. Appl. Phys.* **89**, 2025 (2001).
- [107] S. F. Yu, C. Yuen, S. P. Lau, W. I. Park, and G. C. Yi, *Appl. Phys. Lett.* **84**, 3241 (2004).
- [108] H. Cao, J. Y. Wu, H. C. Ong, J. Y. Dai, and R. P. H. Chang, *Appl. Phys. Lett.* **73**, 572 (1998).
- [109] M. Hotzel, S. Urban, D. Egbe, T. Pautzsch, and E. Klemm, *J. Opt. Soc. Am. B* **19**, 2645 (2002).
- [110] Y. Guo, C. K. Kao, E. H. Li, and K. S. Chiang, *Nonlinear Photonics* (Springer, Berlin, 2002).
- [111] M. Joseph, H. Tabata, and T. Kawai *Jpn. J. Appl. Phys.* **38** L1453 (1997).
- [112] A. Klini, A. Manousaki, D. Anglos, and C. Fotakis, *J. Appl. Phys.* **98**, 123301 (2005).
- [113] S. Acquaviva, E. D. Anna, and M. L. De Giorgi, *J. Appl. Phys.* **102**, 073109 (2007).
- [114] F. Claeysens, A. Cheesman, S. J. Henley, and M. N. R. Ashfold *J. Appl. Phys.* **92**, 6886 (2002).
- [115] R. K. Thareja, H. Saxena, and V. Narayanan *J. Appl. Phys.* **98**, 034908 (2005).
- [116] S. Namba, R. Nozu, and K. Takiyama, *J. Appl. Phys.* **99**, 073302 (2007).

CHAPTER II

Experimental techniques and instrumentation

Abstract

This chapter deals with the experimental set-up employed for the characterization of laser induced and RF magnetron sputtered plasmas. The plasma produced by both laser and RF magnetron sources fall in two separate regimes. The former being highly transient, the experimental set-up used was different and discussed separately. Both the plasmas were studied by OES (nonintrusive) and Langmuir probes (intrusive) diagnostic techniques. For RF magnetron plasma, an RF compensated Langmuir probe was used to avoid the RF interference in the I-V measurements. To eliminate error due to fluctuations in the plasma, probe contamination etc, a high speed voltage ramp generator with output voltage swing capability of -40 V to + 40 V, together with PC controlled data acquisition set-up was indigenously constructed for I-V characteristics of the probe measurements. Thin film characterization tools used in the present study are also discussed in this chapter.

2.1 Introduction

The OES and Langmuir probe methods are well established techniques used to find out the plasma parameters of laser (pulsed) induced and RF magnetron sputtered plasmas [1-9]. The plasma production parameters are varied to understand the corresponding changes occurring in the plasma plume. The very idea of the plasma plume investigation is to get an insight in to the spatial and temporal behavior of the plasma plume and hence to optimize the ablation/sputtering conditions to suit the thin film growth and depositions.

The chapter is divided in to four sections, with the first forming the set-up for laser induced plasma, then the for RF magnetron plasma, third being the voltage ramp and finally about thin film characterization tools used to analyze the films deposited by PLD and RF magnetron sputtering. The electronic circuits and other details of voltage ramp generator and computer interfaced data acquisition set-up designed and constructed indigenously for the purpose of I-V measurements of the RF compensated Langmuir probe, is described in detail. The circuitry exhibited excellent performance in terms of ramp speed, repeatability and flexibility. The main advantages are the incredibly low cost and the simplicity of construction. The experimental results obtained with this set-up on RF plasma, are similar to the reports [6], obtained with commercial Langmuir (Hiden Analytic) probe.

2.2 Laser plasma characterization setup

Laser induced plasma is highly transient in nature, as the exciting source used is Q-switched Nd:YAG laser. The plasma evolution and decay takes place within a time of few microseconds (μ sec). The discrete spectral emissions from the plasma plume and electron and ion time of flight studies using Langmuir probe,

have to be monitored instantaneously. Proper care was taken in triggering various instruments. With the knowledge of rise time of various instruments, the optical path travelled by laser pulses and triggering pulses were adjusted, so that the measurements commenced the moment the laser pulse impinged on the target. This way, errors in the data collected from the plume were minimized. The details of the experimental set-up used for laser plasma characterization are discussed in following sections.

2.2.1 OES experimental set-up

The set-up for imaging of the plasma emission spectra at various spatial positions of the plume and recording of the temporal evolution [time of flight (TOF)] of specific emissions from the plume are shown schematically in figure 2.1. The light flux was collected by the optic fiber bundle, which can be moved along the length of the image of the plume using X-Y translator, having the least count of 10 μm . The other end of the fiber bundle abuts at the entrance slit of the monochromator. The wavelength dispersed spectra was imaged either by the CCD or PMT, the former aligned laterally and the later axially to the exit slit of the monochromator. The swing mirror near the exit slit allows the wavelength dispersed light to pass either to the PMT or CCD. The monochromator, PMT and CCD are controlled by software, (Spectramax for Windows).

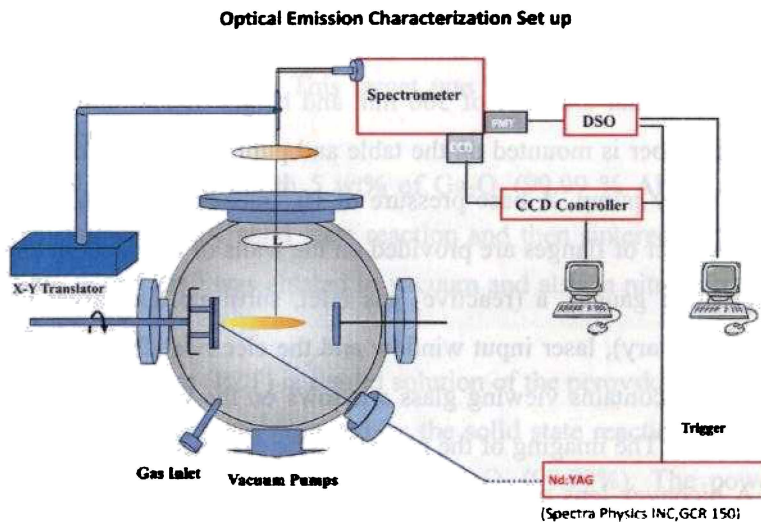


Fig. 2.1 Schematic diagram of OES set-up.

(a) Laser

The laser used for ablation of solid targets is the third harmonic of Q-switched Nd: YAG laser (Quanta Ray, Spectra Physics), operating at 355 nm and having 10 Hz repetition frequency. The laser has Gaussian intensity profile having pulse width (FWHM) of 6 ns. The laser pulse energy can be varied up to 140 mJ. The laser is focused on to the target using a quartz lens (focal length = 300 mm). The spot size of the laser falling on the target can be adjusted so as to get the required laser fluence, measured in J cm^{-2} .

(b) Ablation chamber

The vacuum chamber for laser ablation consists of a cylindrical stainless steel vessel with an internal diameter of 300 mm and height of 250 mm. The basal plane of the chamber is mounted on the table and pumped by a diffusion pump, backed by a rotary pump. A base pressure of 10^{-6} mbar can be attained in the chamber. A number of flanges are provided on the walls of the vacuum chamber to mount pressure gauges, a (reactive) gas inlet, substrate and target holders, backing pump (rotary), laser input window and the electrical feed through. The vacuum chamber contains viewing glass windows on the vertical side and also on the top flat lid. The imaging of the plume can be executed through both these windows. A biconvex lens of focal length 50 mm was kept inside the chamber for creating 1:1 image of the plume. The chamber window and the lens, being inside the chamber, were cleaned or replaced at regular intervals so as to ensure maximum transfer of flux from the plume to the optic fiber bundle. The target holder is rotated at the rate of 20 rotations per minute using an external motor, to avoid pitting. Laser is focused on to the target, at a pre-determined spot size; using a quartz lens of focal length 300 mm. Reactive gases were introduced in to the chamber using respective mass flow controllers. The substrate holder is provided with an electrical heating system.

(c) Target materials

Three targets were ablated at various ablation conditions and the resulting plumes were investigated. The target material basically is zinc oxide (ZnO), which is a very promising two component semiconducting material having tremendous optoelectronic importance. The ZnO basically exhibits n-type conductivity. The conductivity can be enhanced by doping it with third group

elements like Al, Ga etc. The pure ZnO (99.95% purity-Aldrich) powder, which was made in to 1" pellet at a pressure of 7 tons and then sintered at 1000⁰ C for 8 hours was used as the target. This target was ablated in vacuum and also at various oxygen gas pressures.

The ZnO (99.9% Aldrich) with 5 wt% of Ga₂O₃ (99.99 % Alfa Aesar) doped target was synthesized by solid state reaction and then sintered in to 1" pellet. The gallium doped ZnO was ablated in vacuum and also in nitrous oxide (N₂O) reactive ambiances.

Lead zirconium titanate (PZT) is a solid solution of the perovskite lead zirconate and lead titanate. Target was prepared by the solid state reaction of constituent oxides, PbO (99.99%), TiO₂ (99.99%) and ZrO₃ (99.99%). The powder was mixed and heat pressed at 1200⁰ C so as to obtain stoichiometric PZT target.

(d) Charge coupled device (CCD)

Charge Coupled Devices (CCD) is a multichannel silicon array detectors designed using standard MOS architecture. These are array devices in which individual pixel elements are defined by three electrode gates of varied applied potential (3-phase devices). The schematic diagram of a CCD detector is given in figure 2.2. The electrodes are made from vertically stacked, conductively doped poly-silicon and overlay the photosensitive semiconducting silicon. The electrodes are separated from the silicon surface by a thin layer of insulating silicon dioxide. When appropriate voltages are applied to the different electrodes, the electrostatic potentials in the silicon are changed to produce zones of negative potentials surrounding a potential well. Photoelectrons generated by the incident light are then collected and stored in these localized potential wells. CCDs detect and measure light in a three step process [10].

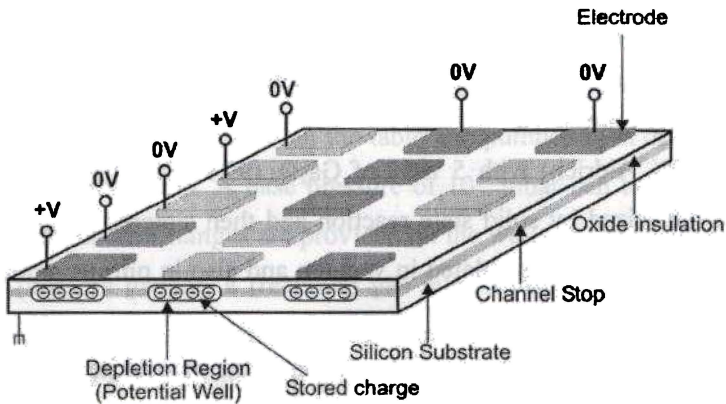


Fig.2.2 Schematic of a CCD detector

1. Absorption of incident photon energy followed by the creation of electron-hole pairs proportional to the number of absorbed photons. The amount of electron-hole pairs generated in each discrete pixel directly depends on the incident light intensity. However the number of the generated electron-hole pairs is a non-linear function of the incident wavelength. As shown in the figure 2.2, the charge resulting from the generated electron-hole pairs in a given pixel is collected in the potential well of that pixel.
2. Transfer of the resulting charge packets within the array from one pixel to the next. At the end of an exposure, the charge integrated in each pixel is transferred from one pixel to the next in a column until it finally reaches the readout registers located along one edge of the chip. This charge transfer is accomplished by sequentially changing the applied potential to the different electrodes as shown in figure 2.3. During this

process of parallel charge transfer, the charge accumulated in one row of pixel is simultaneously transferred to the corresponding pixel in the next row.

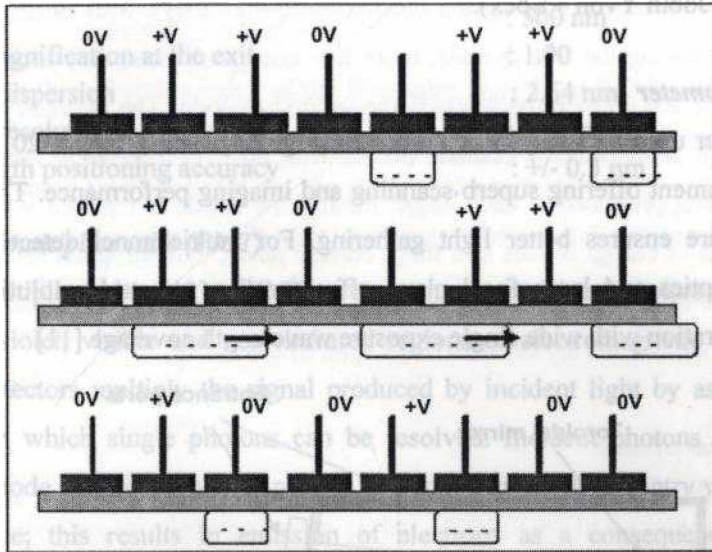


Fig. 2.3 Charge transfer process within a CCD detector

3. The conversion of charge to voltage and subsequent amplification. After the parallel charge transfer process, the charge from each row of pixels is accumulated in the readout registers, located at the edge of the chip. The charge from the individual readout registers is then shifted to an output sense node by an analogous serial charge transfer process. Here the charge is converted to an appropriate voltage. The potential level in this "floating diffusion" sense node varies depending on the amount of

charge present at the node. The sense node is followed by a charge-to-voltage amplifier, which preserves the linear relationship between the generated charge and the voltage output.

The CCD used for the spectral studies is Spectrum One CCD 3000, 1024×256 pixels (ISA Jobin Yvon – Spex).

(e) Spectrometer

Spectrometer used for analysis is Triax 320 (Fig. 2.4). The TRIAX 320 is a 1/3 meter instrument offering superb scanning and imaging performance. The large f/4.1 aperture ensures better light gathering. For multichannel detection, the corrected optics and large focal plane offer excellent spectral resolution and spatial separation with wide single exposure wavelength coverage [11]

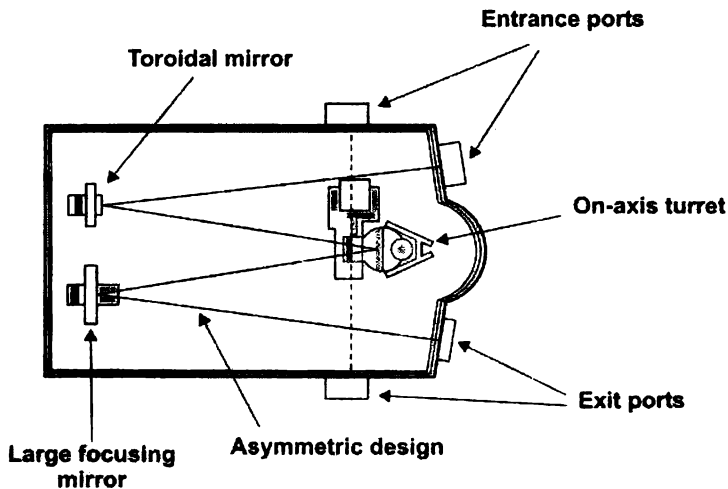


Fig. 2.4 Triax-320 top view

Specifications of Triax 320

| | |
|---------------------------------|---------------------|
| Focal Length f | : 0.32 meters |
| Entrance Aperture Ratio | : $f/4.1$ |
| Grating | : 1200 grooves/mm |
| Grating size | : 68×68 mm |
| Blazed at | : 500 nm |
| Image magnification at the exit | : 1.00 |
| Spectral dispersion | : 2.64 nm |
| Spectral resolution | : 0.06 nm |
| Wavelength positioning accuracy | : ± 0.3 nm |

(f) Photomultiplier tube (PMT)

Photo multiplier tubes [12] or PMTs are extremely sensitive detectors of light in the ultraviolet, visible and near infrared regions of electromagnetic spectrum. These detectors multiply the signal produced by incident light by as much as 10^8 , from which single photons can be resolved. Incident photons strike the photocathode material, which is present as a thin deposit on the entry window of the device; this results in emission of electrons as a consequence of the photoelectric effect. These electrons are directed by the focusing electrode towards the electron multiplier, where electrons are multiplied by the process of secondary emission.

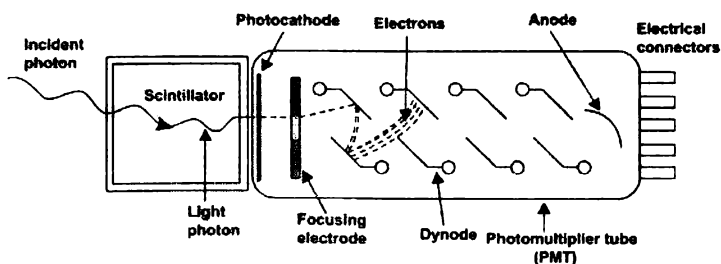


Fig. 2.5 Schematic of a working of a Photomultiplier tube.

The electron multiplier (Fig. 2.5) consists of a number of electrodes, called 'dynodes'. Each dynode is held at a more positive voltage than the previous one. The electrons leave the photocathode, having the energy of the incoming photon (minus the work function of the photocathode). As they move towards the first dynode they are accelerated by the electric field and arrive with much greater energy. On striking the first dynode, more low energy electrons are emitted and these, in turn, are accelerated towards the second dynode. The geometry of the dynode chain is such that a cascade occurs with an ever-increasing number of electrons being produced at each stage. Finally the anode is reached where the accumulation of charge results in a sharp current pulse, indicating the arrival of a photon at the photocathode. The PMT used in the present studies is Hamamatsu, R 5900U-L 16, H 7260 series, with a rise time of 0.6 ns.

(g) Optic fiber bundle

An optical fiber is a glass or plastic fiber, designed to guide light along its length, by confining as much light as possible along its axis. In fibers with large core diameter, the confinement is based on total internal reflection [13]. In core fibers with small diameter, (widely used for most communication links longer than 200 meters) the confinement relies on establishing a waveguide [14]. Light can be guided along the fiber if it enters at an angle, less than the critical angle. For step index fiber, light entering the fiber will be guided, if it falls within the acceptance cone of the fiber. The term 'optical fiber' covers a range of different designs including graded-index optical fibers, step-index optical fibers, birefringent polarization-maintaining fibers and more recently photonic crystal fibers. The fiber consists of a core surrounded by a cladding layer. To confine the optical signal in the core, the refractive index of the core must be greater

than that of the cladding. The boundary between the core and cladding may either be abrupt, [as in step-index fiber], or gradual, [as in graded-index fiber]. For step index multimode fiber, the acceptance angle is determined only by the indices of refraction [15]

$$n \sin \theta_{\max} = \sqrt{n_1^2 - n_2^2} \quad (2.1)$$

where n_1 is the refractive index of the fiber core, n_2 is the refractive index of the cladding and half-angle of the acceptance cone is called the acceptance angle, θ_{\max} . The same relation holds for the numerical aperture (NA) for any kind of fiber. For maximum signal collection, there has to be a match between the NA of the fiber and the lens or system of lenses used. The angular acceptance of a lens is expressed by the f -number f and for a thin lens, imaging an object at infinity, is given by [16]

$$f \approx 1/2NA \quad (2.2)$$

This approximation holds well when the numerical aperture is small. The f number describes the light-gathering ability of the lens. In optical design, the finite distance between the object and the lens must often be considered. In these cases, the “working f -number” is used instead. The working f -number is defined by making the approximate relation above exact:

$$f_w \approx 1/2NA \approx (1-m)f \quad (2.3)$$

where f_w is the working f -number and ‘ m ’ is the lens's magnification for an object a particular distance away [17].

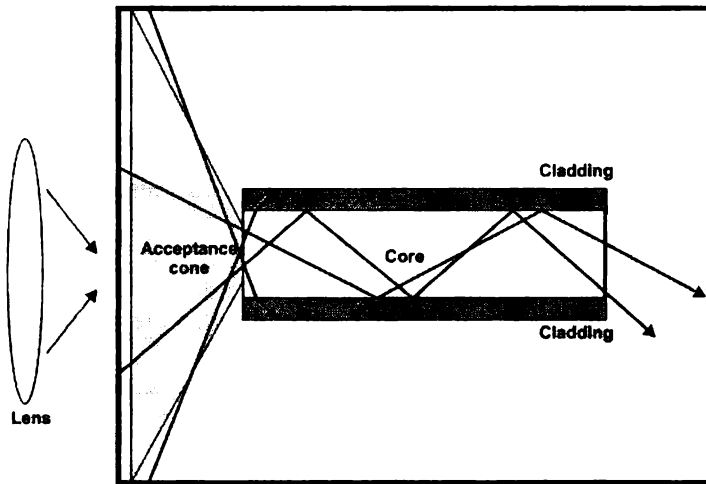


Fig. 2.6 Propagation of light through a multi-mode optical fiber.

The emitted radiation can be collected by using a system of lens and optical fibers which constitute the signal collection system (Fig. 2.6). Emission signals are allowed to fall in the acceptance cone with the help of a lens or a combination of lenses. This combination of the lenses and optic fiber is called “fiber optic collimator”.

A Reflection fiber probe [with 5 illumination fibers and 1 read fiber, each with a core diameter of $400\ \mu\text{m}$], was used for signal collection in the backscattering mode. The fiber had a flexible metal sheathing that could be fastened to the spectrophotometer. The total length of the fiber was 1 m which allowed flexibility in making the experimental arrangement.

(h) Digital storage oscilloscope

A digital storage oscilloscope (Tektronix TDS 2014, Band width-100 MHz, Sample rate-1GS/s), was used to record the rise and decay of emission intensity profile in OES and the TOF transients of ion and electrons generated when each laser pulse impinges on the target. The oscilloscope was interfaced with a PC through GPIB cable so that data recorded in the oscilloscope could be transferred directly to the computer for storage and further processing.

2.2.2 Langmuir probe-TOF of charged particles- Experimental set-up

The experimental set-up for collecting ion and electron TOF transients in laser ablated plasma plume is schematically shown in the figure 2.7. The metallic tip of the Langmuir probe is positioned perpendicular to the propagation direction of the plume. The probe position can be varied along the direction normal to the target, up to 6 cm distance from the surface. The arrangement allows the recording of TOF transients along the propagation direction of the plume, for various laser fluences and vacuum/ambient gas pressures.

(a) Specifics of the Langmuir probe

The Langmuir probe assembly consists of a Tungsten wire, 125 μm in diameter and 5 mm in length, supported by a glass sleeve. The wire can be biased at voltages in the range of -30 to +30 V, relative to the target and the vacuum chamber, with a stabilized power supply coupled to an electrical circuit, that enables the probe to be maintained at a constant bias, while passing the transient current due to charged material in the ablation plume to the oscilloscope. To ensure a clean probe surface, the probe wire was taken out from the chamber and cleaned at regular intervals although no signal attenuation due to material

deposition on the probe was observed during the experiments. The output of the Langmuir probes was directed to a digital oscilloscope (DSO) and then, via a GPIB interface, to a PC for storage and data processing. The oscilloscope was triggered using a voltage pulse from laser controller so as to set zero time for each acquisition.

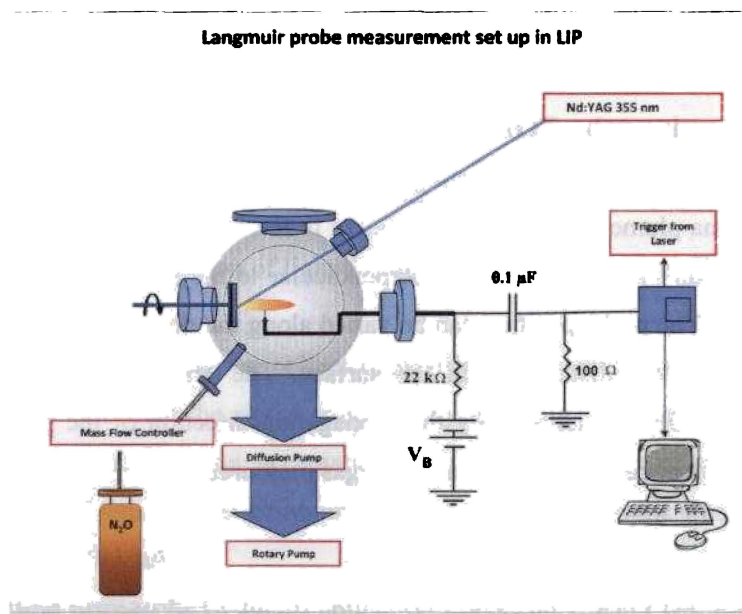


Fig. 2.7 Langmuir probe measurement set-up in LIP

2.3 RF magnetron plasma characterization setup

The RF plasma is characterized by both Langmuir probe and OES techniques [6-9, 18, 19]. The experimental set-up for OES is similar to that used in laser plasma characterization. The Langmuir probe technique has some fundamental difference to that of laser plasma, owing to the difference in the plasma

equilibrium and due to the presence of magnetic field and RF electric field inherent [see section 1.8.2] in the RF magnetron plasma.

The RF plasma characterization using Langmuir probe faces few problems as listed below. Ordinary tungsten fiber, as used in LIP cannot be used here as the probe current recorded will be erroneous due to RF interference. This can be rectified by using an RF compensated probe which filters out the perturbation imposed by the RF frequency, 13.56 MHz and may be its harmonic (27.1 MHz) from the collected probe current. Secondly, Langmuir probe measurement being an intrusive diagnostic technique, the probe tip will get contaminated due to deposits from the target material sputtered. Contamination of the probe tip with the low-conductivity layers introduces additional resistance into the probe circuit that leads to severe suppression, or even absence of current due to low-energy electrons/ions coming on to the probe. Therefore the probe has to be subjected to cleaning processes regularly. The RF plasma, even though time independent, suffers from fluctuation due to small changes in supply voltages in addition to other plasma instabilities. The last two problems can be rectified to a large extent by using high speed voltage ramp generator for biasing the probe, together with fast data acquisition set-up. If the voltage sweep takes place in the order of few milli-seconds the error that may be caused by contamination of the probe becomes negligible. Also, high ramp speed and the provision for multiple sweeps averaging of probe currents eliminates/reduces the possibility of error occurring in the probe current data, due to plasma instabilities.

(a) Sputter chamber

The sputtering chamber is a semi-cylindrical stainless steel chamber and houses two magnetrons (balanced magnetron – Sierra Applied Sciences, USA). This

enables the deposition of thin films by co-sputtering method. The co-sputtering is realized either with two RF sources or with RF and DC sources simultaneously connected to each magnetron. In the present work, the plasma plume generated by single RF sputtering of ZnO powder target was investigated. The vacuum is established in the chamber with six-inch diffusion pump backed by a rotary pump (HindHivac Bangalore). The RF generator (Huttinger Electronics, Germany) is coupled to the magnetron through capacitive matching network. The non-reactive sputtering gas (argon) introduced in to the chamber is controlled by mass flow controller (Aalborg, USA).

(b) RF compensated probe

A tungsten metal tip of length 5 mm and radius 0.5 mm which is supported by glass sleeves act as the Langmuir probe. RF filter circuits to eliminate the interference of fundamental RF (13.56 MHz) and its first harmonic (27.1 MHz) from the measured probe currents are connected along with the tungsten metal tip and enclosed in cylindrical Teflon tube. All probe circuits and other connecting wires are effectively shielded so that no RF interference occurs in the data acquisition.

2.4 Voltage ramp and data acquisition set-up

A block diagram of the whole experimental setup is shown figure 2.8. The PC generates a staircase waveform in the range -10V to +10V with a step size of 0.05V through a 12 bit digital to analog converter.

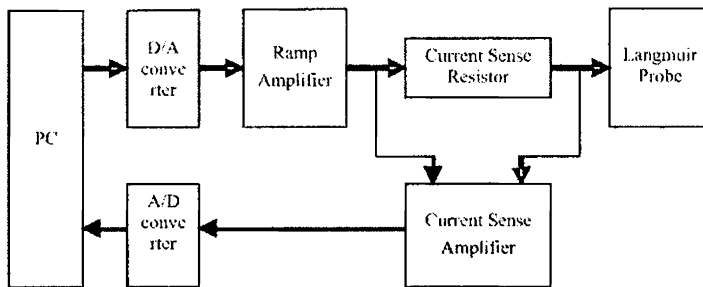


Fig. 2.8 Block diagram of measurement set-up

The ramp amplifier boosts the voltage and current levels and fed to the probe through a current sense resistor. The voltage drop across the resistor is suitably amplified and read by the PC through a 12 bit analog to digital converter. The computer controls both the generation of ramp voltage and measurement of the probe current. The circuit used for the generation of the voltage ramp is shown in figure 2.9 This is essentially an inverting amplifier with enhanced output voltage swing capability of -40V to +40V using OP AMP U1 and transistors Q1 to Q4. Common emitter stages Q1 and Q2 provide the required additional voltage gain and complementary transistors Q3 and Q4 serves as the final output stage capable of delivering a current of up to 100 mA. Feedback resistors R1 and R2 fixes the overall voltage gain at 4. The input is -10V to +10V in steps of 0.05V send from the D/A channel of an analog interface card inserted into one of the expansion slots of a personal computer which controls the entire measurement process and data acquisition.

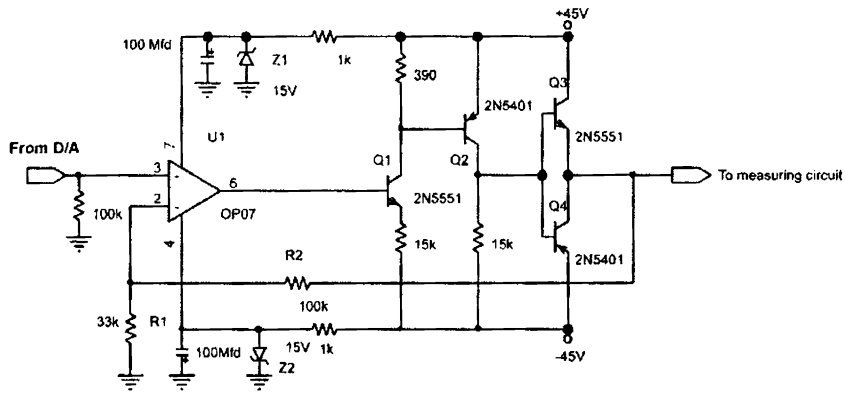


Fig. 2.9 Circuit for voltage sweep amplification.

The output of the amplifier is fed to the Langmuir probe through a current measuring resistance of $1\text{K}\Omega$ (for currents not exceeding 10 mA) and the voltage across the resistor is detected using the circuit formed by OP AMPS U2 to U4 shown in figure 2.10. U2 and U3 are used as attenuators to reduce the common mode voltage and this eliminates the need of expensive isolation amplifiers. U4 compensates for the attenuation and its output is connected to one of the A/D channels of the same interface card. The output of U3 is also measured through another A/D channel to obtain the actual applied voltage and to make correction to the probe current due to the $100\text{ K}\Omega$ resistor associated with U3.

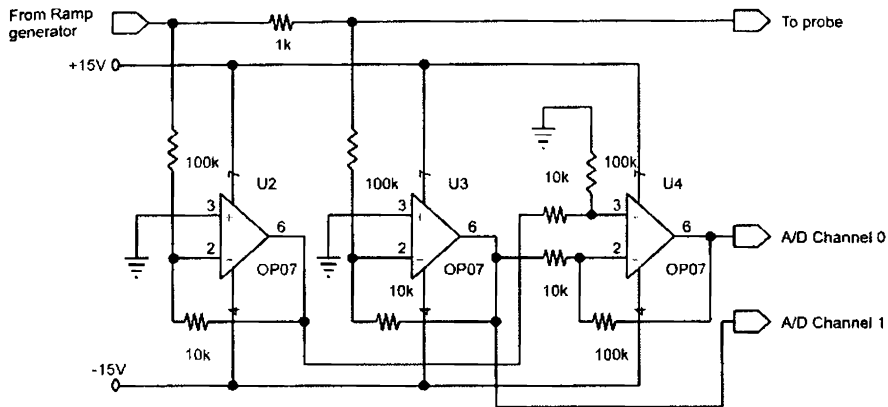


Fig. 2.10 Circuit for probe current measurement.

The program to control the ramp generation and measurement is written in Visual Basic and includes features like Base-line subtraction and averaging. Averaging can be done either within a single sweep by repeated measurement at each data point or by conducting a number of consecutive sweeps and taking point by point average. The time taken for a single sweep without averaging is 20 ms which is essentially the analog to digital conversion time for 400 data points included in one sweep.

2.5 Thin film characterization techniques

Numerous thin films were deposited on Al_2O_3 and glass substrates from the plasma generated by both laser ablation and RF magnetron sputtering with an idea to correlate the plasma properties with thin film deposition. The films were deposited at various input parameters of laser ablation and sputtering. The other deposition parameters were the substrate temperature and target – substrate distance.

Surface morphology is an important property since while going for multilayer devices roughness of the thin film surface play an important role. Scanning electron microscope (SEM -JEOL JSM 5600) is one of the characterization tools which clearly demonstrate an idea about the surface of the thin films. The SEM is a microscope that uses electrons rather than light to form an image. There are many advantages for using the SEM instead of a light microscope [20, 21].

Film thickness is one of the most important thin film properties to be characterized since it plays an important role in the film properties unlike a bulk material. Reproducible properties are achieved only when the film thickness and the deposition parameters are kept constant. The thicknesses of the thin films prepared for the work presented in this thesis were measured by a stylus profiler (Dektak 6M). The stylus profiler takes measurements electromechanically by moving the sample beneath a diamond tipped stylus.

The structural characterization was done by recording the X-ray diffraction (XRD) pattern of the samples. XRD pattern was taken using Rigaku X-ray diffractometer with Cu-K_α radiation ($\lambda=1.5414 \text{ \AA}$). Diffraction analysis is useful whenever it is necessary to know the state of chemical combination of the elements involved or the particular phase in which they are present. Compared with ordinary chemical analysis the diffraction method has the advantage that it is usually much faster, requires only very small quantity of sample and is non destructive [22, 23]. Ref. 21 and 24 provide elaborate discussions of thin film characterization techniques.

References

- [1] A. A. Voevodin, J. G. Jones, J. S. Zabinski, and L. Hultman, *Journal of Applied Physics* **92**, 724 (2002).
- [2] K. J. Saji, N. V. Joshy, and M. K. Jayaraj, *J. Appl. Phys.* **100**, 043302 (2006).
- [3] J. J. Chang and B. E. Warner, *Appl. Phys. Lett.* **69**, 473 (1996).
- [4] P. E. Dyer, A. Issa, and P. H. Key, *Appl. Phys. Lett.* **57**, 186 (1990).
- [5] J. Gonzalo, C. N. Afonso, and I. Madariaga, *J. Appl. Phys.* **81**, 951 (1997).
- [6] A. Palmero, E. D. van Hattum, W. M. Arnoldbik, A. M. Vrendenberg, and F. H. P. M. Habraken, *J. Appl. Phys.* **95**, 7611 (2004).
- [7] J. E. Heidenreich III, J. R. Paraszczak, M. Moisan, and G. Sauve, *J. Vac. Sci. Technol. B*: **5**, 347 (1987).
- [8] M. B. Hopkins and W. G. Graham, *Rev. Sci. Instrum.*, **57**, 2210 (1986).
- [9] M. Nisha, K. J. Saji, R. S. Ajimsha, N. V. Joshy, and M. K. Jayaraj, *J. Appl. Phys.* **99**, 033304 (2006).
- [10] Spectrum One, *CCD Manual*, ISA Jobin Yvon-Spex.
- [11] Triax 320, *Spectrometer Manual*, ISA Jobin Yvon-Spex.
- [12] R. W. Engstrom, *Photomultiplier Handbook*, RCA (1980).
- [13] A. Ghatak and K. Thyagarajan, *Optical Electronics*, Cambridge University Press, New Delhi (1991).
- [14] D. R. Vij, *Luminescence in Solids*, Plenum Press, NY (1998).
- [15] M. J. Adams, *An Introduction to Optical Waveguides*, John Wiley and Sons, (1981).
- [16] B. Michael (ed), *Hand book of Optics. Devices, Measurements, and Properties*, Vol II, 2nd edition, McGraw Hill, NY (1998).
- [17] J. E. Greivenkamp, *Field Guide to Geometrical Optics*, SPIE Field Guides vol. FG01, p. 29. (2004).

- [18] P. Lecœur, B. Mercey, and H. Murray, *J. Appl. Phys.* **78**, 1247 (1995).
- [19] V. von der Gathen, J. Ropcke, T. Gans, M. Kaning, C. Lukas, and H. F. Obele, *Plasma Sources Sci. Technol.* **10**, 530 (2001).
- [20] P. E. J. Flewitt and R K Wild, *Physical methods for materials characterisation*, IOP Publishing Ltd, pp 138 (2003).
- [21] D. K. Schroder, *Semiconductor material and device characterization*, A Wiley-interscience publication, pp 700 (1998).
- [22] B. D. Cullity and S.R. Stock, *Elements of X ray diffraction*, Third edition, New Jersey, Prentice Hall pp 170 (2001).
- [23] M. J. Buerger, *X-ray Crystallography*, John Wiley & Sons, New York chapter 3 (1962).
- [24] C.R. Brundle, C. A. Evans, and S. Wilson, *Encyclopedia of materials characterization*, Manning Publications Co. Greenwich (1992).

CHAPTER-III

Optical emission spectroscopic studies of laser ablated zinc oxide plasmas

Abstract

This chapter is presented in two parts. PART-I deals with the optical emission spectroscopic (OES) studies performed on the plasma produced by the ablation of pure ZnO, using the third harmonic of Nd:YAG laser. The plasma plume behavior was investigated for ablation carried out under vacuum and also in oxygen ambience. The electron density, electron temperature and intensity variations of spectral emission from the species in the ablated plume are discussed as a function of ambient gas pressure and distance along the direction normal to the target.

PART-II is the detailed study performed on LIP of ZnO sample doped with gallium (ZnO:Ga), and ablated in nitrous oxide (N₂O) ambient pressure. Apart from the studies similar to those presented in PART-I, the plasma behavior was also studied in the presence of a substrate maintained at high temperatures and positioned 5 cm away facing the target, a typical configuration employed for thin film growth. The temporal and spatial behavior of various species in the plasma was studied by recording time of flight (TOF) transients along the propagation direction of the plume. ZnO thin films were deposited at different temperatures on Al₂O₃ substrates placed at 5 cm distance from the target. The growth rate of ZnO films as a function of temperature of the substrate is corroborated with the plasma behavior.

3.1 Introduction

Laser ablation is being widely used in various applications of material processing, such as thin-film deposition, chemical reactions, surface modifications and synthesis of nano-clusters. The interaction of laser beam with solid matter and the subsequent plasma generation has actively been studied for the last decade [1-7]. Despite great efforts to exploit the laser matter interaction for material processing and diagnostic purposes, many aspects still need to be elucidated and clarified. In particular, the plasma induced by ultraviolet and visible nanosecond laser is successfully employed for thin film deposition of a wide range of classical and novel materials [8-10] and for in situ qualitative elemental analysis [11-13]. However, to improve the quality of the deposited films for desired application, a sound understanding of the plume dynamics, and physical and chemical properties of the ablated species is required. The properties of thin films deposited by pulsed laser ablation (PLA) are closely related to the dynamics and to the composition of the laser generated plasma.

The stream of atoms, ions, molecules, and clusters ejected from the target surface, is composed of excited neutral and ionized species, which emit radiation that can be analyzed to gather information about its composition and dynamics. The optical emission spectroscopy is a most powerful nonintrusive diagnostic tool, with the help of which the radiations from the plasma plume are analyzed for both qualitative and quantitative determination of the plasma parameters. The dynamic behavior of the plume thus deciphered from the study, together with judicious manipulation of the various input parameters of laser ablation processes, can be utilized for the optimization of deposition conditions of thin films of specific requirement. This chapter is divided in to two parts. In the first part, plasma of pure ZnO is analyzed to derive the electron number density and electron

temperature with small variations of ambient oxygen pressure and low laser fluence. In the second part results of more rigorous plume investigation (spatial and temporal evolution) is discussed with ZnO:Ga sample ablated in N₂O ambience and incorporating wider input parameters of laser ablation.

PART- I:

Pristine ZnO plasma

Optical emission spectroscopic (OES) studies were performed on pure ZnO plasma, generated by ablation using the third harmonic of Nd:YAG laser. The plasma plume behavior was investigated by ablation under vacuum and also in oxygen ambient gas pressures. The electron density, electron temperature and intensity variations of spectral emission from the species in the ablated plume were studied as a function of ambient gas pressure and distance from the target, along the propagation direction of the plume.

3.2 Experimental conditions

3.2.1 Laser ablation parameters

The pure ZnO target [Section 2.2.1 (c)] surface was polished and irradiated by the Nd:YAG laser. The plasma plume was imaged using proper optics and wave length dispersed spectra recorded. The spectra of the plume generated in vacuum ($\sim 10^{-6}$ mbar) and also in ambient gas (oxygen) pressures of 0.003, 0.006 and 0.01 mbar were recorded. The optic fiber bundle was moved along the direction of propagation of the plume (z-axis) from the target surface to a distance of 20 mm using an X-Y translator. Low laser fluence (1.27 Jcm^{-2}) was employed in the

ablation. The experimental set-up for this study is discussed previously [Section 2.2.1].

3.2.2 Monochromator calibration

To ensure the accuracy of results, it is important to consider the influence of broadening of spectral lines affecting resolution. We have used a mercury lamp to measure the resolution of spectrometer. Spectrum of the mercury lamp, in the wavelength range 570 – 580 nm was recorded. The two mercury emission lines at 576.964 nm and 579.109 nm (Fig. 3.1) were used for the determination of resolution ($\Delta\lambda$) of the spectrometer. The peaks were identified and compared with standard wavelength [14]. The resolution of the spectrometer is given by the equation

$$\Delta\lambda = \frac{FWHM}{a} \times \Delta A \quad (3.1)$$

where, ΔA (the difference between the standard wavelength) = 579.065 – 576.965 = 2.1 mm. Here the FWHM of Hg (I) line ($\lambda = 576.964$ nm), is about 0.2725 nm and a , the distance between the two peaks in the figure (Fig.3.1), recorded using the spectrometer, is about 2.145 mm. Thus, resolution of the spectrometer has been calculated as $\Delta\lambda = 0.267$ nm

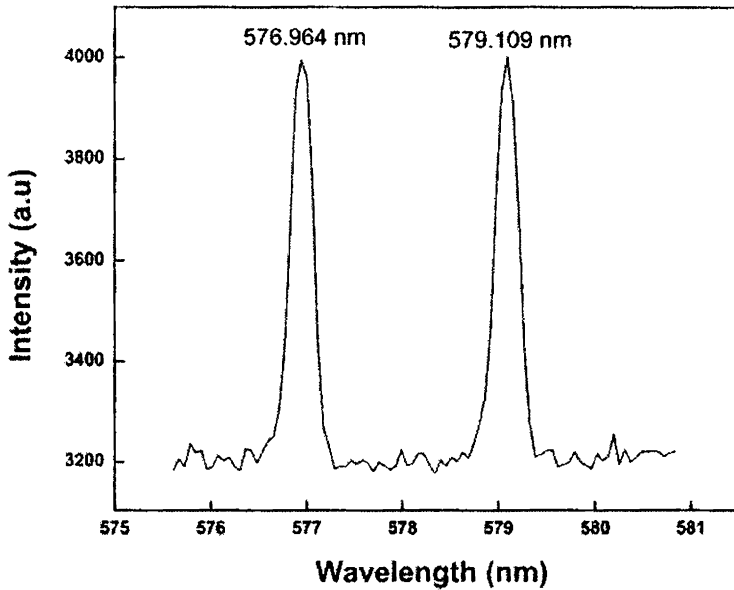


Fig. 3.1 Emission spectra of Hg

3.3 Results and discussions

The spectra arising out of the ablation of ZnO was scanned from near UV to near IR (350 nm – 850 nm). Strong emission lines of neutral zinc (Zn I), singly ionized zinc (Zn II) and neutral oxygen (O I) were obtained. Figure 3.2 shows the wavelength dispersed emission spectrum of the plume accompanying the ablation of the ZnO target in vacuum at laser pulse energy of 1.27 Jcm^{-2} and recorded at a distance of 6 mm from the target surface. The strong, unmarked line at 710 nm is due to the harmonic of the exciting laser wavelength (355 nm). The plasma arising from pulsed laser ablation (PLA) is in the local thermodynamic equilibrium (LTE). The minimum criterion for the plasma equilibrium under LTE approximation in the present study was verified as discussed in section 1.4.2. The

necessary criterion for the validity of as given by Eq. (1.29) was verified for this plasma.

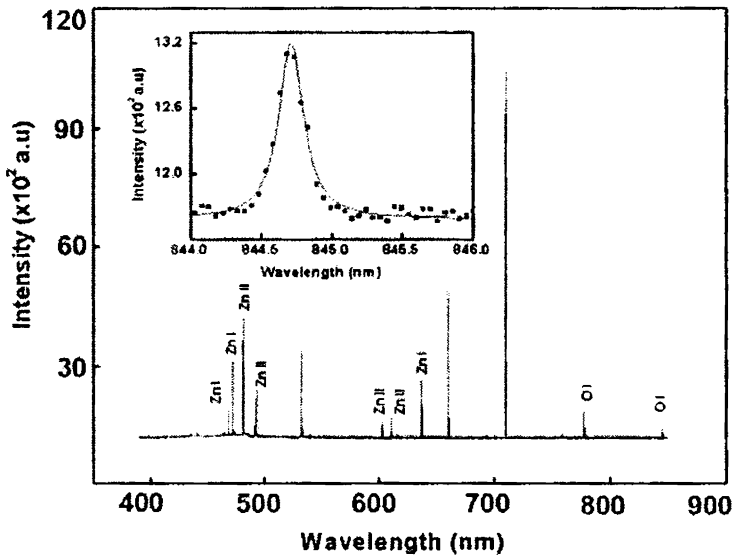


Fig. 3.2 Emission spectra of the ZnO plasma plume produced by laser fluence of 1.27 Jcm^{-2} in vacuum, recorded at a distance of 6mm from the target. Inset shows a typical Stark broadened profile of 844.64 nm O I line and the Lorentzian fit (solid line).

3.3.1 Electron Density and Temperature

For the investigation of plasma parameters like electron temperature (kT_e) and electron density (N_e), optical emission spectroscopic (OES) technique as described in section 1.6.1 was used. The main factors which contribute to line broadening of the emission lines, in LIP are Doppler broadening, and pressure or resonance broadening. These broadening mechanisms have been analyzed and compared with Stark broadening of the spectral lines, which was used for

deriving N_e . For ablation in vacuum, where ablated species exhibit high expansion velocities, one of the dominant contributions to spectral broadening is Doppler broadening, which is due to Doppler shift. The propagation velocities of oxygen has been obtained to be $\sim 10^6 \text{ cms}^{-1}$ in laser ablated ZnO plasma, discussed in the second part of this chapter. The FWHM of Doppler broadening is Gaussian [15] and is calculated using the formula,

$$\Delta\lambda_{1/2} = \sqrt{\frac{8kT_e \ln 2}{mc^2}} \lambda_0. \quad (3.2)$$

With O I emission line at 844.64 nm (λ_0) and for maximum kT_e value (1.3 eV) obtained in this investigation, the $\Delta\lambda_{1/2}$ due to Doppler broadening becomes smaller than 0.15 Å and hence the effect of Doppler broadening can be ignored. The pressure or resonance broadening is proportional to the ground state number density of the corresponding species and transition oscillator strength. As only a small transition oscillator strength is reported [16] for O I at 844.64 nm ($f_{j,j'} = 0.111$), the resonance broadening part can be safely neglected. The Stark broadening is therefore relatively significant in LIP. The FWHM of stark broadened emission line is widely used by various investigators for determining the electron density [14, 16-19].

The electron density was calculated from the FWHM of the Stark broadened lines $\Delta\lambda_{1/2}$ [Eq. (1.42)] described in chapter I. The stark broadened emission line profile is generally Lorentzian and the spectral lines obtained in the present study (inset of Fig. 3.2) fit well with the typical Lorentzian profile. The approximate electron temperature was calculated by the method of Boltzmann plot method, discussed in section 1.6.1 (ii) (a) and was employed for the evaluation of electron impact parameter W and which in turn for the calculation of N_e . Since the value of W is

not very much affected by the variations in T_e , it is presumed that the electron density calculated by this method gives a fairly good result. The 844.64 nm emission line of O I was used for electron density calculations.

For accurate evaluation of T_e the ratio of line intensities from successive ionization stages of the same element is preferred over Boltzmann plot method. In local thermodynamic equilibrium, the ratio of line intensities from successive ionization stages of the same element is given by Eq. (1.45). For these calculations the line intensities corresponding to emission lines of 481.05 nm and 491.16 nm respectively of Zn I and Zn II have been used. The optical data required for the above calculations were taken from reference [16] and NIST atomic spectra database [20].

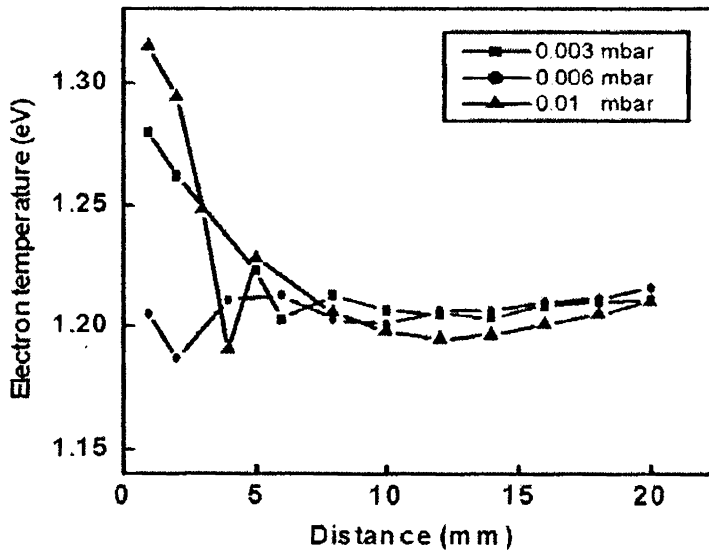


Fig. 3.3 Variation of electron temperature with distance from the target surface for different ambient gas pressures.

The line shape analyses were performed at different distances from the target surface. The spatial variations of electron density and electron temperature give an insight into the basic ionization processes taking place during the pulsed laser ablation. The estimation of electron temperature and electron density of the plasma plume was carried out for distances up to 20 mm from the target surface in a time-integrated manner. The spatial dependence of electron temperature and electron density of the plume is given in figures 3.3 and 3.4. The temperature and density exhibited a decreasing behavior with distance. With increasing distance from the target surface, the electron temperature variation is minimal. kT_e varied about 0.13 eV up to 10 mm distance from the target and thereafter maintained steady behavior while electron density variation is about $1.1 \times 10^{17} \text{ cm}^{-3}$ over a distance of 20 mm.

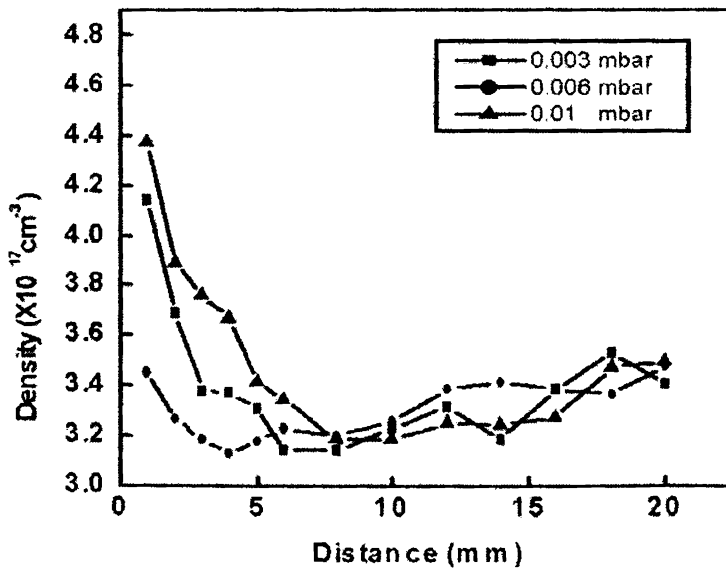


Fig.3. 4 Variation of electron density with distance from the target surface for different ambient gas pressures.

It is seen that the increase in ambient gas pressure decreased the electron temperature however in a small manner as expected. The increase in the ambient gas pressure will cause the collision of the ablated species with the oxygen atoms at the plume edge. This could cause a small reduction in plume expansion rate. As the plume expands in an adiabatic manner after the termination of the laser pulse, the decrease of N_e and T_e can be expected in the ablation of ZnO, quite like the case of exponential decrease reported in the ablation of pure metal targets [21, 22]. The steady nature of T_e from about 10 mm distance indicates that the cooling due to adiabatic expansion is compensated by energy released due to recombination of ions and electrons within the plume.

It is interesting to note that in the vicinity of 20 mm distance from the target surface there is a small tendency for T_e to increase. This could be due to the fact that at this distance, the adjoint mass of the ambient gas at the plume edge impedes the plume expansion, resulting in a large deviation from the free expansion when the mass of the gas surrounding the leading edge of the plume becomes comparable with the plume mass [23]. This impedance in the plume expansion could cause a redistribution of kinetic and thermal energies between the plume and ambient gas leading to a transfer of particle flux velocity into plume thermal energy, resulting in plume heating [24].

Figure 3.4 shows the variation of electron density with distance for three different pressures. It exhibits rapidly decreasing behavior in the neighborhood of the target surface and then remains more or less steady. Similar to the observation of T_e in the vicinity of 20 mm, N_e also shows an upward trend, however, not very significant. The dependence of N_e with background gas pressure is significant only in the regions closer to the target surface.

3.3.2 Intensity variation with pressure

The integrated emission intensity of O I line (844.64 nm) as a function of distance from the target surface is shown in the figure 3. 5. The integrated yield has been obtained by integrating the whole area under the emission profile. This gives a measure of the relative amount of excited species within the plume, arriving at a given point.

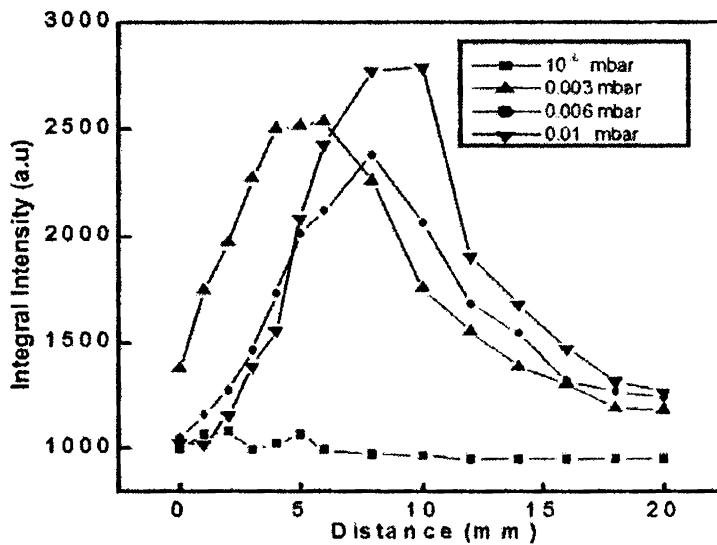


Fig. 3.5 Variation of integral intensity of 844.64 nm line of O I with distance from target surface. Integral intensity of O I without oxygen ambient gas is very small and almost insensitive of distance from the target.

The emission intensity of O I picked up with distance from the target surface up to around 10 mm and then decreased monotonically with distance in all the cases of ambient gas pressures over which the investigations were carried out. This is due to the increase in the excitation of oxygen atoms by collision with the

particles in the plume in the early stage of plume expansion. In the later stage, the collision probability decreases due to the increase in the mean free path and hence the observed decrease in intensity. However it should be noted that the increase in oxygen pressure increases the emission intensities. For ablation in vacuum, the oxygen line intensities were found to be very small and insensitive to distance variations. The integral intensities of the emission lines of both Zn I and Zn II (Fig.3.6 and 3.7) exhibited a steady behavior from around 10 mm distances from the target surface.

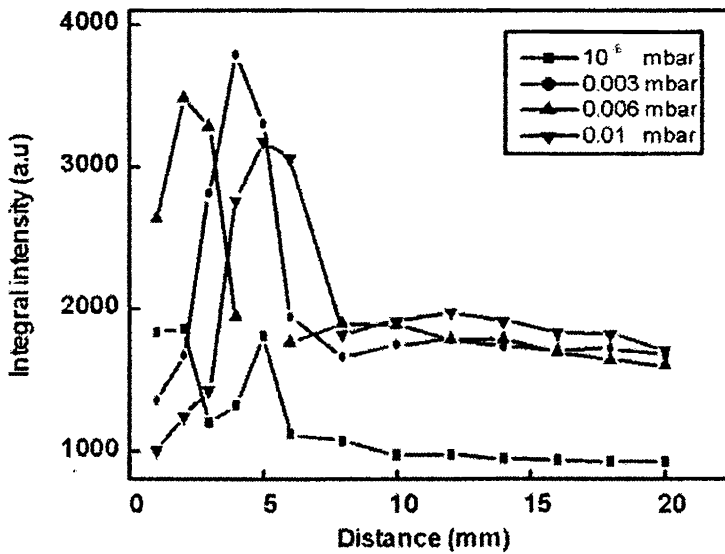


Fig. 3.6 Variation of integral intensity of 636.23 nm line of Zn I with distance from target surface. Increasing the ambient gas pressure increases the populations of excited Zn I.

The integral intensity variations of the ablated species show that zinc ions are many folds large compared to oxygen and neutral zinc when ablated under high

vacuum. This means that plasma stoichiometry differ from that of the target when ablated in vacuum. Hence ZnO thin films with 1:1 stoichiometry cannot be expected under this condition and this is in agreement with the observations of Claeysens *et al.* [25]. Increase in oxygen pressure increased the integral intensities of the excited states of neutral Zn and neutral oxygen while that of Zn ions decreased. This could be attributed to the fact that increase in pressure will decrease the mean free path of particles in the plume; thereby probability of collision of Zn ions with electrons in the plume increases. This will enhance the rate of electron-ion recombination, leading to the increase in the number of excited neutral zinc atoms. Also the neutral Zn atoms themselves could be raised to the excited state by collisions (refer section 1.3).

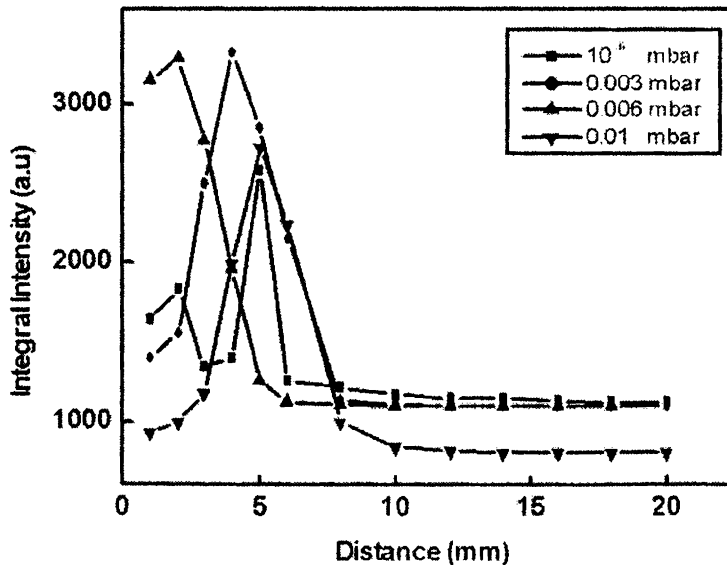


Fig. 3.7 Variation of integral intensity of 491.16 nm line of Zn II with distance from target surface. The increase in ambient gas pressure decreases the population of excited Zn II after 8 mm distance from the target.

The steady behavior of electron density, electron temperature and integral intensities of Zn and Zn ions, and high oxygen line intensities above 10 mm from the target surface suggests that high quality ZnO thin films can be expected when substrate is placed beyond this distance. However the reports show that stoichiometric and crystalline films are formed at a few centimeter distances from the target surface [26]. This may be due to the fact that even at relatively low laser intensities near the threshold for ablation, it has been observed that the ablated materials are significantly ionized [27,28] and the ions in the plasma plume can have energies ranging up to several hundred eV [29]. So when the substrate is placed at a closer distance to target there is the chance of sputtering from the substrate by these highly energetic particles and thereby affecting the qualities of the films deposited. Hence for proper nucleation and adherence and thereby for the formation of crystalline thin films, larger target to substrate distance and heating of substrate are suggested.

3.4 Conclusions

The electron temperature and electron density in ZnO laser plasma show almost similar spatial behaviour. Both decrease with distance from the target surface and become more or less steady from 10 mm distance from the target with electron temperature being at 1.2 eV and electron density at $3.2 \times 10^{17} \text{ cm}^{-3}$. A small rise in both N_e and T_e are observed at around 20 mm distance from the target. In the context of ZnO thin film formation the present investigation suggests that the films will invariably be non-stoichiometric when target is ablated in high vacuum. Ablating the target in the oxygen atmosphere and keeping the substrate beyond 10 mm from the target could improve the stoichiometry.

PART-II:

Gallium doped ZnO plasma

Zinc Oxide generally exhibit n-type conductivity which can further be enhanced by doping with aluminum or gallium. There are reports of ZnO thin films with p-type conductivity when doped with gallium and ablated in N₂O or NH₃ ambience [30]. In this section we report the electron number density variations in terms of (i) laser fluences, (ii) distance from the target, (iii) ambient gas pressures and (iv) substrate temperature with the substrate placed at 5 cm from the target. The kinematics of emitting species in the plasma has been studied by taking TOF transients of respective species under various ablation conditions. The choice of input parameters of laser ablation is in accordance with the conditions used typically for the deposition of thin films. The information gathered from the plasma investigation is corroborated with the deposition of ZnO thin films.

3.5 Experimental set-up

The target, gallium doped zinc oxide (ZnO:Ga), was prepared by solid state reaction method as described in the section 2.2.1(c). The laser beam was focused on to the target to a spot size of 1.0 mm diameter and laser pulse energy varied from 10 mJ to 50 mJ. This corresponds to laser fluence variations of 1.27 Jcm⁻² to 6.35 Jcm⁻². The ablations were carried out at 0.01 mbar, 0.02 mbar and 0.03 mbar nitrous oxide (N₂O) ambient gas pressures. In order to study the effect of temperature on the plasma, an Al₂O₃ substrate was kept at 5 cm away from the target and was electrically heated. The plasma produced at various laser fluences and ambient gas pressures was studied at substrate temperatures of 500 °C, 600 °C and 700 °C.

The time evolution of specific emitting species of the plume was investigated using the fiber bundle – monochromator – PMT assembly, by recording the TOF transients, spatially at various laser fluences and ambient gas pressures. TOF transients were recorded at 1 mm interval across the spatial range from 1 mm to 12 mm, from the target surface. For TOF studies the ambient gas pressure was varied over a wider range (0.0001 mbar to 0.1 mbar) and the laser fluence increased up to 7.62 Jcm^{-2} . The experimental set-up for this study is discussed in section 2.2.1. ZnO thin films were deposited on Al_2O_3 substrates at various substrate temperatures. The films were analyzed for the structural properties using x-ray diffraction (Rigaku, with Cu-K α radiation, 1.5414 Å) and thickness, by (Dektak 6 M) Stylus profiler.

3.6 Result and discussions

3.6.1 Spectral emissions

To ensure the accuracy of spectral recording, the resolution of the spectrometer, $\Delta\lambda = 0.267 \text{ nm}$ was determined using standard emission lines of mercury as discussed in 3.2.2. The optical emission spectra of plasma plume were recorded in the wavelength range from 400 nm to 850 nm at various positions of the plume along the target-normal. Significant variations in the intensities of emission lines of various atomic and ionic species of the plasma were observed with changes in laser fluence, ambient gas pressures, substrate temperature and distance from the target surface. A typical wavelength dispersed spectrum of plasma recorded at 5 mm distance from the target surface for a laser fluence of 3.81 Jcm^{-2} is shown in figure 3.8. Spectra were composed of numerous Stark broadened lines superimposed on continuous background. The background emission is due to

bremsstrahlung of electrons heated by interaction with laser radiation, and /or black body emission from the large particulates ejected from the target.

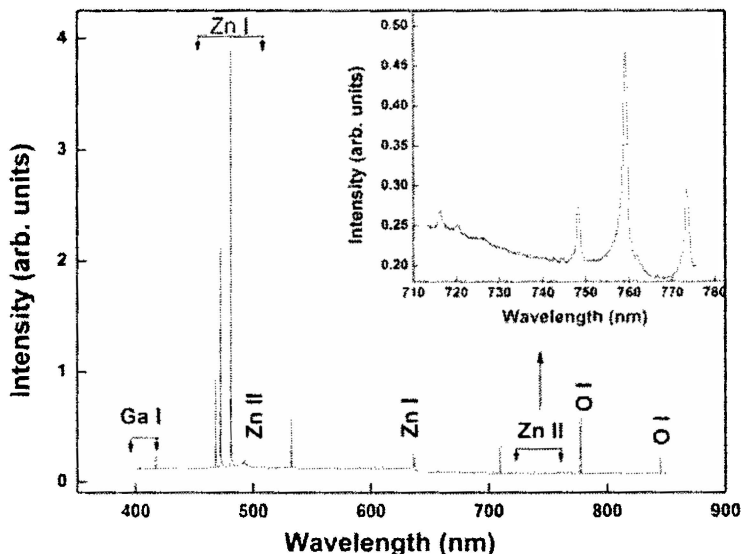


Fig. 3.8 Wavelength dispersed emission spectrum of plume recorded at 5mm away from the target surface, laser fluence being 3.81 Jcm^{-2} . Inset: Zn II lines in the range 740 nm to 775 nm.

Oxygen emission lines have been detected only in its atomic state in this investigation. Oxygen emission lines in its ionic state have not been reported in laser ablated ZnO plasma even at higher laser fluence or with different laser sources [25,31-34]. The O I emission triplet centered at 777.5 nm could not be resolved with our spectrometer. The Stark broadened O I emission line at 844.64 nm [$2s^2 2p^3 ({}^4S^o) 3s {}^3S_1 - 2s^2 2p^3 ({}^4S^o) 3p {}^3P_2$] was used for determining electron density of the plasma. The Zn I emission lines at 468.01 nm [$4s 4p {}^3P_0 - 4s 5s {}^3S_1$], 472.21 nm [$4s 4p {}^3P_1 - 4s 5s {}^3S_1$], and 481.05 nm [$4s 4p {}^3P_2 - 4s 5s {}^3S_1$] were

recorded with very high intensity while the 636.23 nm [$4s\ 4p\ ^1P_1 - 4s\ 4d\ ^1D_2$] emission was recorded with very low intensity in comparison with other Zn I emissions. Spectral emissions from neutral gallium at 403.29 nm [$4s^2\ 4p\ ^2P^0_{1/2} - 4s^2\ 5s\ ^2S_{1/2}$] and 417.20 nm [$4s^2\ 4p\ ^2P^0_{3/2} - 4s^2\ 5s\ ^2S_{1/2}$], even though weak compared to Zn I or O I lines, were recorded at all spatial positions along the target normal. The intensity of zinc ionic (Zn II) emission lines in the plume was weak [$492.401\ \text{nm}, 4d\ ^2D_{5/2} - 4f\ ^2F_{7/2}$]. Weaker Zn II lines at 747.88 nm, 758.85 nm, 761.29 nm and 773.25 nm were diagnosed at the initial stage of plume expansion. [See the inset of Fig. 3.8]. The spectral intensities increased with increase in laser fluences and ambient gas pressures.

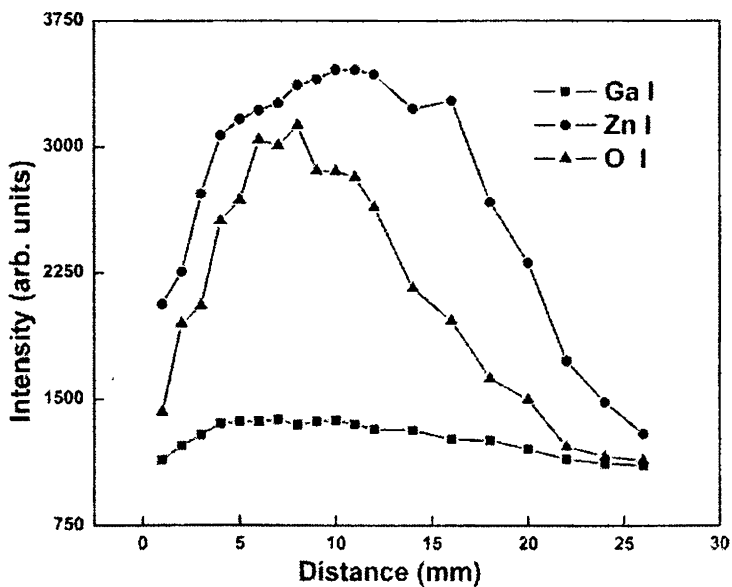


Fig. 3.9 The spatial variation of integral intensities of Zn I (468.01 nm), Ga I (417.20 nm) and O I (777.5 nm) obtained from spectra recorded at a laser fluence of $2.54\ \text{Jcm}^{-2}$ at nitrous oxide partial pressure of 0.03 mbar.

Figure 3.9 shows the spatial variation of integral intensities of Zn I (468.01 nm), Ga I (417.20 nm) and O I (777.5 nm) obtained from spectra recorded at a laser fluence of 2.54 Jcm^{-2} and nitrous oxide partial pressure of 0.03 mbar. The nature of intensity variations of all emitters were found to be similar with intensity reaching maximum approximately at 10 mm distance from the target. One of the weak lines, 468.01 nm of Zn I, was selected here so as to have intensity comparable with those of O I and Ga I. The oxygen emission intensity variation plotted here is with the triplet line centered at 777.5 nm which was more intense compared to 844.63 nm emission line of oxygen. The growth and decay of Zn I intensity emission was gradual and occupied greater spatial coverage compared to our earlier report [31] discussed in PART-I, where comparatively low laser fluence was used in the ablation. The high emission intensity of all species at points closer to the target is due to the possibility of high excitation of the species due to collisions and laser plasma interaction, taking place in the beginning of plasma expansion. In further expansion of plasma plume, the excitation by collision decreases due to the increase in the mean free path, accounting for the reduction in the emission intensities of all the species. The increase in temperature of the substrate and the increase in N_2O partial pressure enhanced the spectral emission intensities of the species in the plume

3.6.2 Electron density (N_e)

The electron density is an important parameter of the plasma which is numerically equal to ion density, as the plasma is electrically neutral. The measurement of N_e provides the knowledge of basic ionization process taking place in plasma. The information regarding the spatial variations of N_e with variations in the ablation conditions is important in the purview of film deposition

by laser ablation. The contribution of the line broadening mechanism like Doppler broadening, pressure or resonance broadening have been evaluated and found to be too small and insignificant as compared to the line width of emission lines in the plasma plume. The nature of line broadening in this experiment can therefore totally be assigned to Stark broadening mechanism. Since the perturbation caused by ions is negligible compared to that due to electrons, the full width at half maximum (FWHM) of Stark broadened lines $\Delta\lambda_{1,2}$ is related to the electron density by the Eq.(1.42). W in the expression is the electron impact parameter which is a slowly varying function of electron temperature (kT_e). Under the assumption of local thermal equilibrium (LTE), the approximate electron temperature of the plasma can be determined by the ratio of emission line intensities of the same atomic or ionic species, as given by the equation 1.44 [section 1.6.1 (ii) (b)]. The O I emission lines centered at 777.53 nm and 844.64 nm were used for determining the approximate electron temperature required for the evaluation of electron impact parameter W . The validity of LTE approximation of the plasma was verified for the ablation conditions employed in the electron density measurements using McWhirter criterion [Eq. (1.29)]. The FWHM of the emission line at 844.63 nm was used for electron density calculations. With the excitation energy $\Delta E_{mn} = 10.94$ eV for the above emission line, the lowest limit for N_e obtained in this experiment as per the criterion, is $1.6 \times 10^{17} \text{ cm}^{-3}$. This is well below the calculated values of electron density at all distances and ablation conditions used in this investigation implying that LTE approximation is valid. The optical data required for the above calculations were taken from Ref. [16] and NIST atomic spectra data base [20].

(a) Effect of substrate temperature (T_s)

The increase in the temperature of the substrate, placed 5 cm away from the target, resulted in an increase in electron number density at all ablation conditions. Figure 3.10 shows the spatial variations of electron density of the plasma with the variations in temperature of the substrate (T_s). The ablation conditions employed for this plot were the N_2O ambience of 0.01 mbar and laser fluence of 6.35 Jcm^{-2} . The electron density increased from $6.48 \times 10^{17} \text{ cm}^{-3}$ to $7.01 \times 10^{17} \text{ cm}^{-3}$ at 10 mm distance from the target for the increase of T_s from $500 \text{ }^\circ\text{C}$ to $700 \text{ }^\circ\text{C}$. The nature of spatial variations of electron density was identical at all T_s . The intensities of spectral emissions were also found to increase with increase in substrate temperature. This is also an indication of the presence of greater number of emitting species in the plume at elevated T_s .

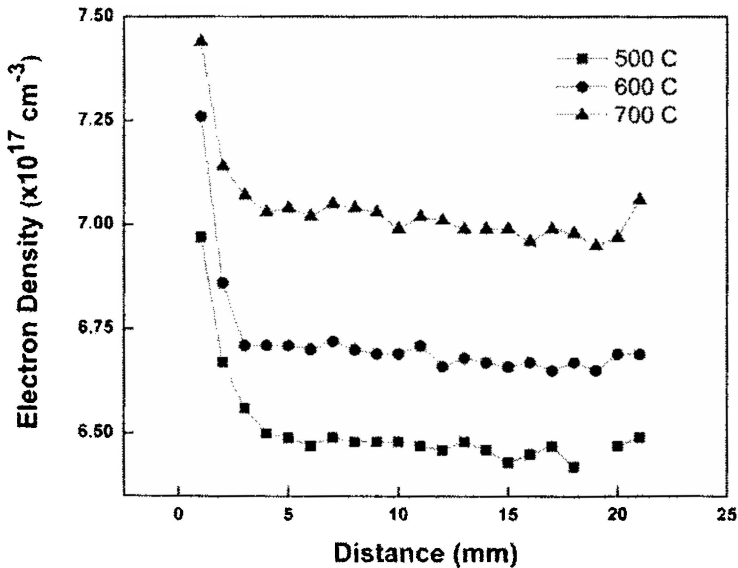


Fig. 3.10 Spatial variations of electron density (N_e) as a function of substrate temperature (T_s).

Even though ZnO plume has higher electron density at higher T_s , the thickness of ZnO film deposited was found to decrease with increase in T_s (see inset of Fig. 3.14). The vapor pressure of Zn is high and increases rapidly with the increase in temperature, resulting in re-evaporation of Zn atoms from the substrate before being oxidized [35,36]. The oxygen content in the chamber is small for oxidation to take place at the substrate, as the ZnO target is ablated in N_2O ambience and there is no indication of the dissociation of N_2O during the ablation. Moreover the oxygen deposited at the substrate also starts evaporating at substrate temperature. The evaporation takes place at all temperatures of the substrate and the rate of evaporation increases with increase substrate temperature. This cause the zinc species to return to the main body of the plume before being oxidized thereby is increasing the number density.

The increase in N_e at points adjacent to the target calls for elaborate considerations. We have obtained the increase in the intensity of spectral emissions and electron density with increase in substrate temperature, at all points starting from the target surface. There are reports (Ref. 25) on back scattering of zinc from laser ablated ZnO plume and the irradiated spot on the target surface becoming Zn rich. This point has been verified in our laboratory also. The increase in surface temperature may also be causing an increase in back scattering of Zn atoms or ions thereby increasing the density at points in the immediate vicinity of the target surface. Elaborate surface morphological studies of the ablated target (using XPS or EDAX) as a function of the number of laser shots, with all the input laser ablation parameters is needed to ascertain this effect. This is a scope for further study. The effect of increase in N_e with increase in T_s was observed at all ambient gas pressures and laser fluences.

(b) Effect of Pressure

The electron density was found to be rapidly decreasing initially over spatial variation from the target surface and remained almost constant value beyond 5 mm distance from the target surface (Fig. 3.10). Similar variations of N_e are reported in literature on laser ablated plasma [31,37,38]. The spatial variations of N_e were identical at all ambient gas pressures and N_e increased with increase in pressure. The plume shrinks with increase in pressure and hence the ejected particles emitting radiation occupy smaller volume thereby increasing the integral intensity and hence N_e . The increase in laser fluence caused increase in electron density at all ambient gas pressures and distances from the target surface. The electron density varied from $6.58 \times 10^{17} \text{ cm}^{-3}$ to $7.20 \times 10^{17} \text{ cm}^{-3}$ for laser fluence variations from 1.27 Jcm^{-2} to 6.35 Jcm^{-2} at 2 mm distance.

3.6.3 Time of flight (TOF) measurements

TOF transients of Zn I (472.21 nm) emission at 5, 8 and 12 mm from the target surface is shown in figure 3.11. Similar TOF transients were recorded for gallium (Ga I) and oxygen (O I) neutrals having emission lines respectively at 417.20 nm and 777.5 nm. The behavior of TOF transients revealed that the early part of all Zn I transients were very similar to those of Ga I transients. However, the Ga I transients displayed a tail extending to later time.

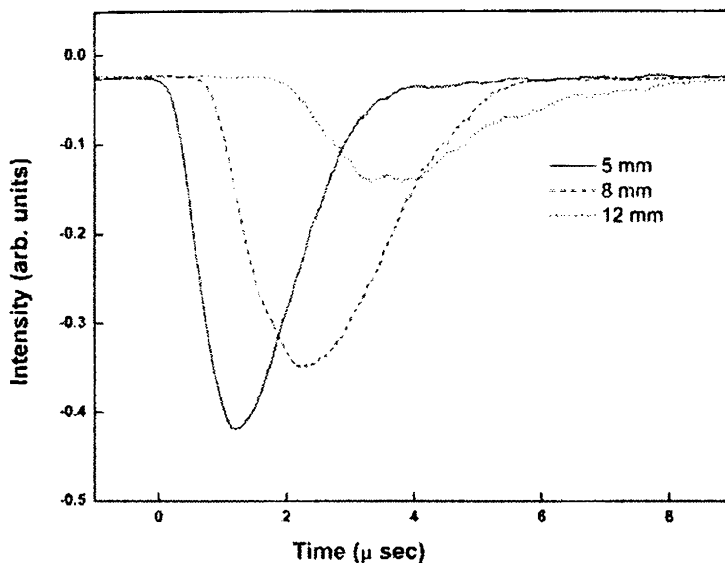


Fig. 3.11 The spatial variations of TOF transients of Zn I (472.215 nm) spectral emission recorded at 3.81 Jcm^{-2} and 0.1 mbar N_2O pressure

The expansion velocities of all the emitters in the plume were deduced from their respective TOF transients. Among the neutral species, the zinc atoms were found to have maximum velocity followed by gallium and then oxygen. All the species were found to attain maximum velocity of propagation at 5 mm distance from the target with Zn I, Ga I and O I having velocities respectively of 4.14 km/s, 3.92 km/s and 3.53 km/s. Beyond 5 mm distance the velocities of all the species decreased and reached 3.36 km/s, 2.77 km/s and 2.52 km/s respectively at 12 mm distance from the target. Figure 3.12 represents the spatial variations of velocity of neutral zinc, gallium and oxygen deduced from the TOF transients recorded at laser fluence of 3.81 Jcm^{-2} and 0.1 mbar N_2O pressure. The decrease in velocity of the species beyond 5 mm indicates that the pressure gradient of the plume

begin to decrease beyond 5 mm distance, which eventually reduced the forward thrust and hence the velocity of the species of the plume.

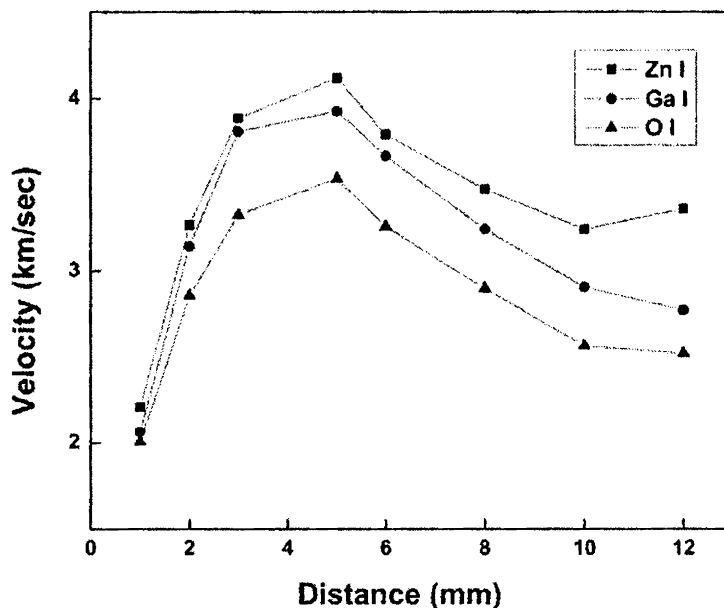


Fig.3.12 The spatial variations of velocities of zinc, gallium and oxygen neutrals deduced from the TOF transients recorded at 3.81 J/cm^2 and the ambient gas pressure of 0.1 mbar.

The increase in ambient gas pressure caused reduction in the propagation velocities of the plume. The TOF transients of all the species were recorded for nitrous oxide pressures ranging from 0.0001 mbar to 0.1 mbar at various laser fluences and distances. The increase in pressure greatly impeded the plume propagation as evident from the TOF peaks shifting towards longer time regime when pressure was increased (Fig. 3.13). The propagation velocity of gallium registered a decrease from 6.45 km/s to 3.87 km/s at 4 mm away from the target

at the extremes of the above pressure range when ablated at a laser fluence of 3.81 J/cm^2 . This amounts to nearly 40% reduction in the velocity of plume propagation. Figure 3.13 is the TOF transients of 417.20 nm emission line of Ga I recorded in the above ablation conditions. Similar TOF transients were obtained for other species also. The inset of figure 3.13 shows the dependence of velocity of the species with ambient gas pressure deduced from TOF transients recorded at 4 mm distance from the target. All the species exhibited large reduction in the velocity as the pressure was increased. It was also observed that decay tail of all TOF transients extended to later time with increase in pressure.

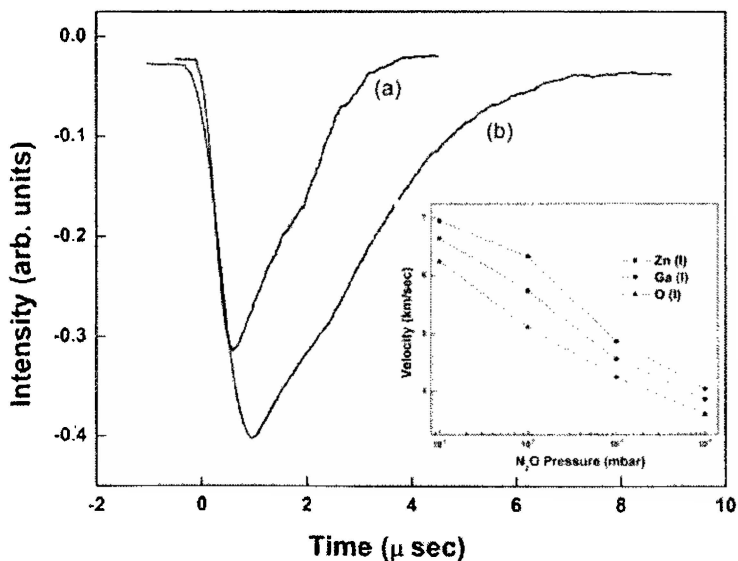


Fig. 3.13 The TOF transients of 417.20 nm emission line of Ga I recorded at (a) 0.0001 mbar and (b) 0.1 mbar N_2O ambient gas pressures and laser fluence of 3.81 J/cm^2 . Inset: The variation of velocities of Zn I, Ga I and O I with ambient pressure.

The TOF signal intensity increased with increase in pressure. The increase in pressure impedes the plume propagation [39] and causes shrinkage [40] of plume. Therefore the plume will have increased number of emitters per unit volume as evident from the increase in ion density with increase in pressure. This accounts for the broader and temporally elongated TOF transients at increased ambient pressures.

Finally, the forward velocity of propagation of the plume is enhanced with increase in laser fluence. Gallium neutrals registered intermediate velocity (Fig.3.12) compared to other two neutral species. The velocity of gallium increased from 3.895 km/sec to 5.19 km/sec when laser fluence was increased from 3.81 Jcm⁻² to 7.62 Jcm⁻², ambient gas pressure being 0.1 mbar. That is the velocity of the particle increased nearly 33% when the laser fluence was doubled.

3.6.4 Thin film analysis

Temperature dependence of the ZnO film growth was studied by depositing films on Al₂O₃ (c-axis oriented) substrates placed at a target to substrate distance of 5 cm at various temperatures ranging from 400 °C to 700 °C. The ablation was carried out with a fixed laser fluence of 2.54 Jcm⁻², 0.001 mbar N₂O atmosphere and deposition time of 30 minutes. The deposition conditions used in this investigation correspond to the ablation conditions frequently employed in pulsed laser deposition of ZnO [41-45]. Increase in temperature of the substrate improved the crystallinity of thin films. The x-ray diffraction (XRD) patterns of the films (Fig. 3.14) showed a decrease in the full width at half maximum (FWHM) with increase in temperature of the substrate and was minimum at 600 °C. The FWHM increased for films deposited at 700 °C. Zinc has high vapour pressure at this temperature leading to highly nonstoichiometric film growth and

thereby high FWHM. The growth of ZnO thin films was difficult at the substrate temperature of 800°C. All XRD patterns showed that films deposited were of (002) orientation with the deposition rate decreasing steadily with rise in temperature of the substrate (inset of Fig.3.14).

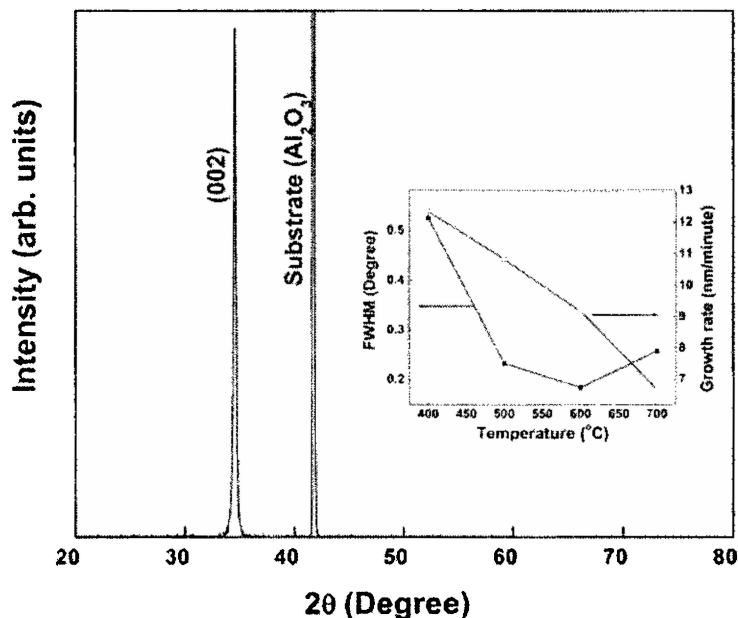


Fig. 3.14 The XRD pattern of ZnO film deposited on Al₂O₃ at substrate temperature of 600 °C. The inset shows the variation of FWHM of XRD pattern and growth rate of ZnO films deposited at various temperatures.

The observations of reduction of film thickness with temperature of the substrate substantiates our earlier contention [Section 3.6.2 (a)] that the evaporation of particles from the films takes place at elevated temperatures and are pushed back in to the plume, contributing to increase in the ion density of the plasma plume. Jejurikar et. al [41] have also reported the reduction in film thickness with

increase in substrate temperature for ZnO films deposited by laser ablation. The substrate temperature of 600 °C provided films with best crystallinity under the above deposition conditions.

3.7 Conclusion

The spatial variation of electron density was evaluated as a function of laser fluence, ambient gas pressure and temperature of the substrate. The electron density registered increase with increase in all the three parameters. The increase in the number density in the plume with increase in temperature of the substrate is the direct indication of the evaporation of deposits taking place from the substrate at elevated temperature. The film thickness decreased while the crystallinity improved with increase in substrate temperature.

The wavelength dispersed spectra of the plume contained very intense emission lines corresponding to zinc neutral and moderately intense oxygen neutral lines. The gallium emission lines were obtained in the blue region of the visible spectra with low intensity. The emission lines of ionic species were those of singly ionized zinc and were obtained with very weak intensity. The integral intensity of various species of the plume increased with increase in laser fluence, ambient gas pressure and temperature of the substrate at all spatial points along the propagation direction of the plume.

3.8 Comparison of OES studies of ZnO and ZnO:Ga plasmas

The electron number density is higher in the ZnO:Ga plasma even when ablated at similar laser fluence as done in pure ZnO. This may be due to difference in the

reactive ambient gas composition and pressure compared to the ablation of pristine ZnO. The increase in the laser fluence in ZnO:Ga ablation did not bring large increase in N_e . A considerable portion of the laser energy appears to have been used up to acquire kinetic energy of the ejected particle, as evident from TOF studies which shows a 33% increase in velocity of the species when laser fluence was doubled from 3.81 Jcm^{-2} . This increase in the velocity corresponds to more than 1.5 times increase in kinetic energy of the particles. With this in mind and the knowledge of impedance of particle velocity with increase in ambient gas pressure, for gradual and fissure free thin film growth low laser fluence and high ambient pressure are found desirable.

Oxygen in its ionic state was not found in both investigations. The oxygen emission intensity was lower in the gallium doped ZnO plume as it was ablated in N_2O ambience. The zinc ionic emissions intensity was very weak in ZnO:Ga plume as compared to ZnO plume. This may also be due to the increase in the collisional recombination [Eq. (1.17)] occurring in the former due to three component reactive gas ambience. No nitrogen emission lines detected in the ZnO:Ga plume indicating that the laser-plume interaction did not bring about the dissociation of N_2O molecule, so as to have nitrogen species in any excited state. The increase in temperature of the substrate seems to have effected a gradual transformation of the plasma in to the same stoichiometry as the target. This is evident from better nucleation and crystallinity of the deposited films at elevated substrate temperatures. More sophisticated thin film characterizations like Hall measurements, energy dispersed x-ray diffraction etc. are needed to ascertain the type of conductivity, percentage content of elements etc in the films deposited by ZnO:Ga ablation.

References

- [1] R. Kelly and R. W. Dreyfus, Nucl. Instrum. Methods Phys. Res. B: **32**, 341 (1988).
- [2] R. Kelly, A. Miotello, B. Braren, A. Gupta, and K. Casey, Nucl. Instrum. Methods Phys. Res. B: **65**, 187 (1992).
- [3] R. Kelly and A. Miotello, Appl. Phys. B: **57**, 145 (1993).
- [4] S. Amoruso, Appl. Phys. A: **69**, 323 (1999).
- [5] G. Colonna, A. Casavola, and M. Capitelli, Spectrochim. Acta Part B : **56**, 567 (2001).
- [6] J. Perrière, E. Millon, W. Seiler, C. Boulmer-Leborgne, V. Craciun, O. Albert, J. C. Loulergue, and J. Etchepare, J. Appl. Phys. **91**, 690 (2002).
- [7] R. E. Leuchtner, Appl. Surf. Sci. **127**, 626 (1998).
- [8] P. R. Willmott and J. R. Huber, Rev. Modern Phys. **72**, 315 (2000).
- [9] A. D. Giacomo, V. A. Shakhmatov, G. S. Senesi, and F. Prudenzeno, Appl. Surf. Sci. **186**, 533 (2002).
- [10] D. P. Norton, M. Ivill, Y. Li, Y. W. Kwon, J. M. Erie, H. S. Kim, K. Ip, S. J. Pearton, Y. W. Heo, S. Kim, B. S. Kang, F. Renc, A. F. Hebard, and J. Kelly, Thin Solid Films, **496**, 160 (2006).
- [11] S. Yalcin, D. R. Crosley, G. P. Smith, and G. W. Faris, Appl. Phys. B **68**, 121(1999).
- [12] A. Ciucci, M. Corsi, V. Palleschi, S. Rastelli, A. Salvetti, and E. Tognoni, Appl. Spectrosc. **53**, 960 (1999).
- [13] F. Capitelli, F. Colao, M. R. Provenzano, R. Fantoni, G. Brunetti, and N. Senesi, Geoderma **106**, 45 (2002).

- [14] M. Ying, Y. Xia, Y. Sun, Q. Lu, M. Zhao, and X. Liu, *Appl.Surf. Sci.* **207**, 227 (2003).
- [15] W. L. Wiese, “*Line Broadening*”, in “*Plasma Diagnostic Techniques*”, R. H. Huddleston and S. L. Leonard, Eds. Academic Press, New York, p 268 (1965).
- [16] H. R. Griem, *Plasma Spectroscopy*, Mc Graw Hill, New York, p 238 (1964).
- [17] G. Bekfi, “*Principles of Laser Plasmas*”, Wiley, New York, (1976).
- [18] R. K. Thareja, H. Saxena, and V. Narayanan, *J. Appl. Phys.* **98**, 034908 (2005).
- [19] S. S. Harilal, C. V. Bindhu, R. C. Isaac, V. P. N Nampoori, and C. P. G. VAllabhan, *J. Appl. Phys.* **82**, 2140 (1997).
- [20] J. R. Fuhr, and W. L. Wiese, “NIST Atomic Transition Probability Tables” in *Handbook of Chemistry and Physics*, 79th Edition, ed. By D.R. Lide (CRC press, Boca Raton, FL, pp 10-126, 10-146 (1998).
- [21] F. J. G. Vazquez, A. Perea, J. A. Chaos, J. Gonzalo, and C. N. Afonso, *App. Phys. Lett.* **78**, 7 (2001).
- [22] A. A. Voevodin, S. J. P. Laube, S. D. Walck, J. S. Solomon, M. S. Donley, and J. S. Zabinski, *J. Appl. Phys.* **78**, 4123 (1995).
- [23] Y. B. Zeldovich and Yu. P. Raizer, “*Physics of Shock waves and High-Temperature Hydrodynamic Phenomena*”, Academic Press, New York (1966).
- [24] N. Arnold, J. Gruber, and J. Heitz, *Appl. Phys. A: Mater.Sci.Process.* **69**, S87 (1999).
- [25] F. Claeysens, A. Cheesman, S. J. Henley, and M. N. R. Ashfold, *J. Appl. Phys.* **92**, 6886 (2002).

- [26] R. Manoj, A. Antony, C. Vineeth, and M. K. Jayaraj, Proc.of DAE-BRNS National Laser Symposium, India, P423 (2002).
- [27] P. E. Dyer, Appl. Phys. Lett. **55**, 1630 (1989).
- [28] T. N. Hansen, J. Schou, and J. G. Lunney, Europhys. Lett. **40**, 441 (1997).
- [29] T. N. Hansen, J. Schou, and J. G. Lunney, Appl. Phys. Lett. **72**, 1829 (1998).
- [30] M. Joseph, H. Tabata, and T. Kawai Jpn. J. Appl. Phys. **38** L1453 (1997).
- [31] K. J. Saji, N. V. Joshy, and M. K. Jayaraj, J. Appl. Phys. **100**, 043302 (2006).
- [32] R. K. Thareja, H. Saxena, and V. Narayanan J. Appl. Phys. **98**, 034908 (2005).
- [33] A. Kilini, A. Manousaki, D. Anglos, and C. Fotakis, J. Appl. Phys. **98**, 123301 (2005).
- [34] S. Acquaviva, E. D'Anna, and M. L. De Giorgi, J. Appl. Phys. **102**, 073109 (2007).
- [35] *Semiconducting Transparent Thin films*, edited by H.L. Hartnagel, A.L. Dawar, A.K.Jain, and C. Jagadish, Institute of Physics, London, p. 116 (1995).
- [36] V. Ratnikov, R. Kyutt, T. Shubina, T. Paskova, E. Valcheva, and B. Monemar, J. Appl. Phys. **88**, 6252 (2000).
- [37] M. Ying, Y. Xia, Y. Sun, M. Zhao, Y. Ma, X. Liu, Y. Li, and X. Hou, Laser and Particle Beam, **21**, 97, (2003).
- [38] N. M. Shaikh, S. Hafeez, B. Rashid, S. Mahmood, and M. A. Baig, J. Phys. D: Appl. Phys. **39**, 4377 (2006).
- [39] S. Amoruso, A. Sambri, and X. Wang, J. Appl. Phys. **100**, 013302 (2006).

- [40] S. Amoruso, A. Sambri, M. Vitiello, and X. Wang, *Appl. Surf. Sci.*, **252**, 13, 4712 (2006).
- [41] S. M. Jejurikar, A. G. Banpukar, A. V. Limaye, S. K. Date, S. I. Patil, K. P. Adhi, P. Misra, L. M. Kukreja, and R. Bathe, *J. Appl. Phys.* **99**, 014907(2006).
- [42] R. S. Ajimsha, M. K. Jayaraj, and L. M. Kukreja, *J. Elelctron. Mater.* (DOI: 10.1007/s11664-007-0365-4)
- [43] R. S. Ajimsha, K. A. Vanaja, M. K. Jayaraj, P. Misra, V. K. Dixit, and L. M. Kukreja, *Thin Solid Films*, **515**, 7352 (2007).
- [44] A. Suzuki, T. Matsushita, T. Aoki, Y. Yoneyama, and M. Okuda, *Jpn. J. Appl. Phys.* **38**, L71 (1999).
- [45] P. Misra, T. K. Sharma, S. Porwal and L. M. Kukreja, *Appl. Phys. Lett.* **89**, 161912 (2006).

CHAPTER IV

Spatial investigations of ion and electron time of flight in laser ablated ZnO plasma

Abstract

The time of flight (TOF) spectra of ions and electrons of laser ablated ZnO:Ga plasma plume were recorded. The laser fluence was varied from 2.55 Jcm⁻² to 17.85 Jcm⁻² and the ablation was carried out in vacuum and N₂O ambient pressure ranging from 0.0001 mbar to 0.1 mbar. The TOF spectra were recorded at positions along the direction normal to the surface from 10 mm to 50 mm distance from the target surface. Ion acceleration and corresponding electron deceleration were detected in the plasma due to the formation of electric double layer during plasma expansion. Twin peaks were recorded in the ion TOF spectra, corresponding to the accelerated and thermal ions, while two categories of thermal electrons were detected in electron TOF spectra. The behavior of these ions and electrons were studied as a function of laser fluence, ambient gas pressure and distance from the target surface.

4.1 Introduction

The kinematics of charged particles (electrons or ions) in laser ablated plasma is an important aspect in the purview of structural composition, surface morphology, thermal and electrical properties of thin films, deposited by laser ablation. The phenomenon of ion acceleration/electron deceleration taking place in laser induced plasma plume of ZnO:Ga target, ablated at conditions used typically for deposition of thin films, is the subject of this chapter. This behavior of charged particles is attributed to the occurrence of a self consistent ambi-polar electric field arising in the expanding plasma. Hairapetian and Stenzel [1] have given a comprehensive study of double layer (DL) formation with a detailed picture of the ion dynamics and electric field evolution during plasma expansion. The potential, electric field and space charge density vary qualitatively within the layer. This happens as a consequence of breaking the quasi-neutrality of the plasma. The ions, those enter the region of potential drop, experience acceleration. In effect the DL divides the expanding plasma in to regions with thermal and accelerated ions.

Early works on LIP with Langmuir probe measurements have yielded double peak [3-5] or multi-peak structure of ion signals [6], indicating that ion acceleration is an integral part of laser ablated plasma. The multi-peak structure of ion signals is reported to be due to the presence of differently charged ions in the plasma. These experiments were performed at very high laser power in which emission of soft x-rays [3] is also reported. In the event of plasma production by pulsed laser ablation splitting of ion flux in to two or several components have been reported [7-10]. As in high fluence experiments, the reports [11,12] on ion acceleration are related to the ambi-polar electric field, which invokes the concept of DL. Recently Sunil et al [13], reported multiple

peak structure in ion current transients and temporally elongated multiple peak electron current transients in the plasma produced by high fluence (40 Jcm^{-2}) irradiation of lithium fluoride target. In the present work the LIP of ZnO:Ga is studied by recording the TOF of ions and electrons and are discussed in conjunction with ion acceleration and corresponding electron deceleration initiated by DL effect in the plasma.

4.2 Mechanism of DL formation

The plasma is in general quasi-neutral and hence field free. Localized strong electric field arises due to the formation of so called double layer (DL) which is consisting of two equal but oppositely charged, essentially parallel but not necessarily plane space charge layers having separation of the order of Debye length. The production of a double layer requires regions with a significant excess of positive or negative charge, where quasi-neutrality is violated. In general, quasi-neutrality can only be violated on scales of the order of the Debye length. The charge distribution in a double layer is such that the charge density is located in two very thin layers, and inside the double layer the density is constant and very low compared to the rest of the plasma. In this respect, the double layer is similar to the charge distribution in a capacitor. The ions entering at the high potential side of the double layer are accelerated while; the electrons entering at this region are decelerated and successively reflected. Although electric double layers have been studied for many decades, the understanding of the occurrence and the effect produced by this in laser ablated plasma are still far from complete.

The double layer is actually called “double layer” because it is composed of a layer of positive charge, “bending” the plasma potential like a normal sheath, and a layer of negative charge, “bending” the plasma potential back in the other direction, in order to join to the null-electric-field plasma. On each side of the double layer, the plasma may be perturbed by extended pre-sheaths, matching the conditions at the edges of the double layer to those of the undisturbed plasma, in the same fashion as a normal sheath. A typical double-layer potential profile and the associated electric field and charge density profiles are shown schematically in figure 4.1.

The figure 4.1 also illustrates how the thermal (slow) electrons are getting pushed back or severely decelerated in the main body plume on the basis of formation of DL in expanding plasma. Space charge neutral plasma in region C is expanding against vacuum A. From the plasma surface area B, the electrons of the same temperature as the ions are leaving faster due to their small mass letting behind a positive ion cloud such that the charge density due to the Gauss law produces a potential $\Phi(x)$ depending on the depth x and the derivative of Φ results in an electric field $E(x)$ within B. It is assumed that the thickness (l) of the double layer B is equal to the Debye length [λ_D] [14],

$$l = \lambda_D = \left(\frac{kT_e}{4\pi e^2 N_e} \right)^{1/2} \quad (4.1)$$

where, k is the Boltzmann constant, T_e is the plasma temperature, e is the charge of the electron, and N_e is the electron density.

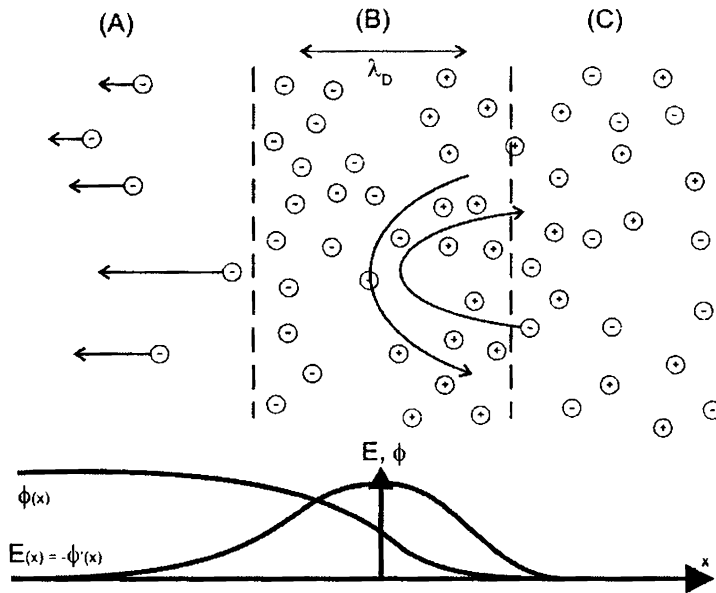


Fig. 4.1 Expansion of quasi-neutral plasma (region C) of temperature T_e into vacuum (region A). An Interface is created by the faster electrons leaving the surface area of region B letting behind positive charges in a double layer of thickness of the order of λ_D .

The positive charge in B causes that after the fast electrons have left, that the following electrons from the plasma interior are either driven back or severely decelerated (see the bent arrows in the figure). The electric double layer of B is acting like a work function for the electrons of which the fast ones of the Maxwellian distribution have to overcome the potential step Φ to reach the vacuum resulting in the well known thermionic Richardson equation as known for the electron emission of hot surfaces.

It is generally accepted that double layers must fulfill the three conditions below.

- (i) The double-layer potential drop Φ must obey $|\Phi| > kT_e/e$, where k is the Boltzmann constant, T_e is the downstream electron temperature and e is the elementary charge.
- (ii) The electric field must be much stronger inside the double layer than outside, so the integrated positive and negative charges nearly cancel each other.
- (iii) Quasi-neutrality is locally violated at the position of the double layer.

The formation of the well-developed DL in LIP is associated with the generation of energetic (hot) electrons which advance ahead of the main body of the plasma plume. They gain additional energy from within the expanding plume. For the low energy electrons the terms “thermal” and “cold” are commonly used. Two mechanisms that can be assigned for the formation of hot electrons in laser-ablation plasmas are, (a) three-body recombination [refer section 1.3.1] when an electron is captured by an ion to some level (not to the ground state) with transfer of the excess energy to another electron [15] and (b) absorption of incident laser radiation due to inverse bremsstrahlung [4,16,17] [refer section 1.3.3]. The cold and hot electrons undergo energy changes during the plume expansion which may be explained as follows. The rate of photo-recombination depends on the electron temperature as $T_e^{-1/2}$, whereas the rate of three-body recombination follows a $T_e^{-9/2}$ dependence [15]. Thus, a cold electron has a large chance to recombine in collision with an ion, while a hot electron can take part in three-body recombination as a third particle, so that it gets additional energy becoming all the more energetic. The total cross section of the electron degradation in the gas phase tends to decrease with E_e at $E_e > 10$ eV [18]. Hence, the electrons that received an additional energy are more capable of surviving compared to cold ones. These electrons move ahead faster leaving

behind the dense plasma and reach the region A (refer figure 4.1) creating situation conducive for DL formation in LIP.

A number of theoretical models [19-21] are available to understand the DL formation in expanding plasmas. These theoretical and numerical models are designed for collisionless and one dimensional expansion of plasma. In the laser ablated plasma from solid target, the degree of ionization decreases during expansion due to recombination process and hence cannot be treated collisionless. Here, the ambi-polar electric field responsible for ion acceleration/electron deceleration apparently varies in a much greater range than it can be described in the framework of a collisionless model.

In this chapter, Langmuir probe measurement of ion/electron TOF transients are recorded in laser ablated ZnO plasma over a range of fluence typical for thin film deposition [22-26]. The spatial dependence of TOF signals in vacuum and various N₂O ambiances have been studied to elucidate the kinematic behavior of charged particles in the plume.

4.3 Experimental set-up

Using cylindrical Langmuir probe TOF experiments were carried out in a vacuum chamber evacuated to a base pressure of 10^{-6} mbar. The ion and electron TOF transients averaged over 5 laser shots were recorded on a fast digital storage oscilloscope and stored in a PC for further processing. In order to examine the effect of ambient gas on the plasma expansion, the nitrous oxide (N₂O) gas at various pressures was introduced in to the chamber. The target preparation, Langmuir probe specifications and other circuit details for signal acquisition and processing are discussed in the section 2.2.2. The laser beam was focused on to the target to a spot size of 1.0 mm radius and laser pulse energies

varied from 20 mJ to 140 mJ. This corresponds to laser fluence variations of 2.55 Jcm^{-2} to 17.85 Jcm^{-2} . The laser ablations of ZnO:Ga target were carried out in high vacuum (10^{-6} mbar) and at four different ambient gas (N_2O) pressures in the range from 0.0001 mbar to 0.1mbar. Experiments were performed for target-to-probe distances varying from 1 cm to 5 cm. The Langmuir probe was placed along the target normal and oriented parallel to the target surface. The probe bias voltage was suitably varied to record the ion and electron TOF transients.

4.4 Results and discussion

4.4.1 Ion time of flight

Ion current signals were recorded in high vacuum at various distances from the target surface for laser fluence varying from 2.55 Jcm^{-2} to 17.85 Jcm^{-2} . The probe bias voltage was fixed at -20 V for recording the ion current signals as at this voltage the TOF signals became independent of the probe bias. Now the probe will be biased in the ion saturation region. Figure 4.2 shows the TOF spectra recorded for various laser fluences at 1 cm distance from the target surface. The two distinct peaks in the spectra correspond to those of fast (accelerated) ions and slow (thermal) ions respectively. Both peaks of the ion current pulse gained intensity and both categories of ions became faster with increasing laser fluence. The twin peaks were more distinct and possessed large temporal separation at low laser fluences [Fig. 4.2 (a)] while at high laser fluences the slow ion peak got suppressed due to the intensity of fast ion peak [Fig. 4.2 (b)].

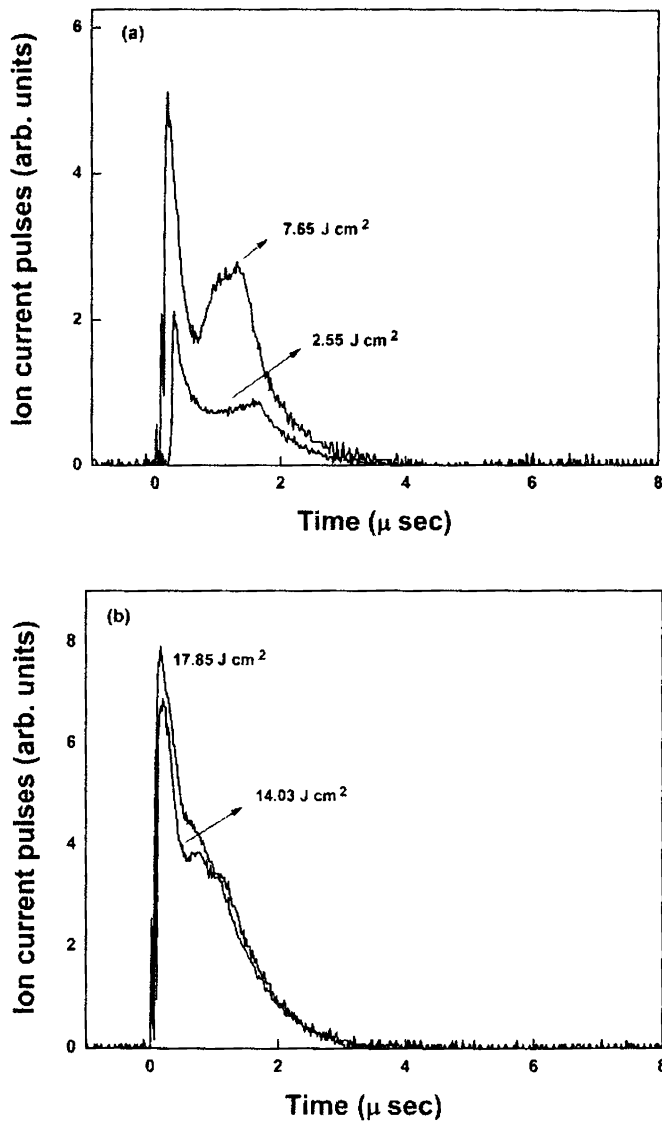


Fig. 4.2 Ion TOF spectra recorded when ablated in vacuum with probe placed at 1 cm from target. (a) Twin peaks are distinct at low laser fluences. (b) At high laser fluences both peaks tend to merge.

The area enclosed by the time of flight spectrum is proportional to the charge collected by the probe. The sharp fast ion peaks suggest that only relatively fewer ions from the plasma bulk undergo acceleration due to DL. The peak position corresponds to the average arrival time of the ions from which the average velocity was derived. With increase in laser fluence, large number of ions is ejected from the target with increased energies which in turn increased the forward propagation velocity of the plume. The TOF behaved as if the ions transfer gradually from slow to fast peak with increase in the laser fluences.

Bulgakova et al [27] have reported the occurrence of twin peaks in the TOF spectra of ions recorded using ion probe in the laser ablated plasma plume of graphite. The phenomenon of ion acceleration initiated by the electric field of DL has been attributed for this effect. The DL causes some ions to acquire additional energy and reach the probe faster. As the ions gain energy due to the DL, they exhibit fast decaying TOF spectrum at points closer to the target at all laser fluences. The electrons in the quasi-neutral region of the plume on the other hand subsequently suffer deceleration and hence show extended TOF spectra compared to those of ion. This is discussed in detail in the later sections.

Mannion et al [28] have reported the occurrence of twin peaks in the ion TOF spectra of plasma plume in the ablation of silver target. They have observed the fast peak diminishing in intensity with successive laser shots and altogether disappearing after a certain number of laser shots. Contamination of the target surface has been quoted as the reason for this phenomenon. Ultra fast peaks (along with slower ones) are reported in the ion TOF some LIP [6] due to the presence of ions of higher degree of ionization states in the plume. In the present

investigation no variations in the intensity of hot ion peak was observed with more number of laser shots impinging on the target. Moreover the wavelength dispersed optical emission spectra of the plume taken using the monochromator - CCD assembly neither showed any spectral emission line other than those corresponding to the target material nor emissions corresponding to any doubly ionized species. Thus the possibility of contamination of the target surface or simply the presence of species of second or higher ionization states as the reasons for the occurrence of fast peak is ruled out in the present study.

The figure 4.3 shows the ion TOF spectra recorded at various laser fluences and probe positions when ablation was carried out in vacuum. Close to the target the fast and slow peaks in the TOF spectra were very sharp and distinct for all laser fluences. This substantiates the fact that the DL is very prominent in the early stages of plume expansion. At probe positions away from the target the fast ion peak intensities are weak and since thermal ion peaks are still weaker they become hardly distinguishable at low laser energies but gain prominence only at very high laser pulse energies [thermal ion peak shown with arrow mark Fig.4.2 (b)]. Both slow and fast ion peaks shift to shorter time regime as laser fluence is increased.

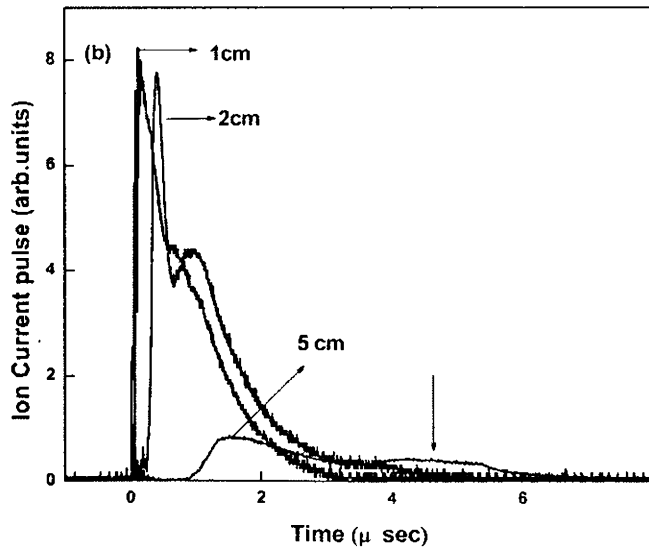
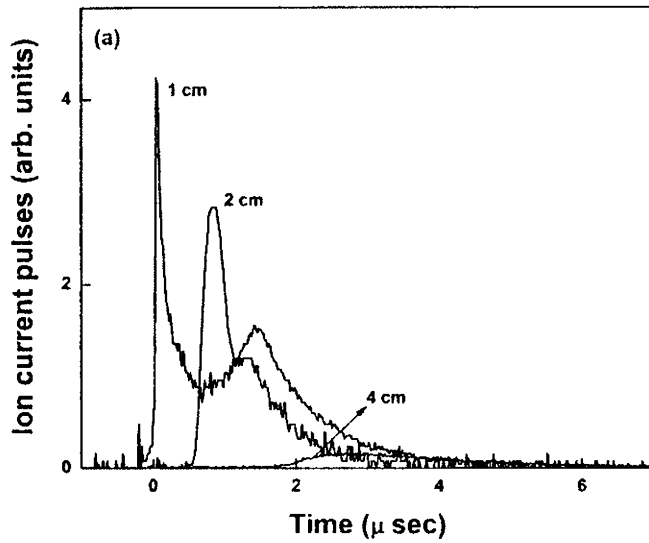


Fig.4.3 Spatial variations of ion TOF recorded in vacuum and its dependence on laser pulse energy, (a) 3.825 Jcm^{-2} , and (b) 17.85 Jcm^{-2} Twin peaks at large distances are visible only at very high laser fluence. [Thermal ion peak is shown with arrow mark in (b).]

The fast and slow ion current peaks show wide temporal separation and both kinds of peaks are suppressed very much when Langmuir probe was positioned at large distances from the target surface. The absence of clear twin peaks at larger distance is due to the following reasons.

- (i) The DL gets degraded as the plume advances. This is because the charge separation becomes wider due to the difference in the velocities of ions and electrons causing the field due to DL to diminish as the plume advances in space. The ambi-polar electric field thus apparently varies in a much greater range.
- (ii) The thermal ions suffer more scattering due to collision with particles in the plume compared with fast ions and hence only a very few thermal ions reach the probe.
- (iii) There exists a greater electron – ion recombination probability for thermal ions which further reduces its number reaching the probe.

The figure 4.4 shows the variations of fast ion peak position with laser fluence in vacuum. The spatial variations of velocities of fast ions were deduced from the respective TOF transients. The ion velocity varied from 34.50 km/s to 80 km/s for laser fluence variations from 2.55 Jcm⁻² to 17.85 Jcm⁻², the probe being placed at 1 cm distance from the target. This corresponds to zinc ion energy variations in the range of 400 eV to 2220 eV. In the event of laser ablation of pure ZnO in vacuum [29], oxygen ambiances [30,31] and in the present study, the only ion species detected in the plume is singly ionized zinc (Zn I). Hence the ion kinetic energies referred here are assigned solely to singly ionized zinc.

The ion velocity obtained here is one order higher compared to the velocity of neutrals found in laser ablated ZnO by optical emission spectroscopy (refer Fig.

3.5 where the velocity is plotted for laser fluence of 3.81 J cm^{-2}). Thus the hot ions even though fewer in number, as deciphered from the narrow peak are accelerated to a large extent compared to the neutrals or thermal ions due to the electric field of DL. The velocities of these hot ions have been drastically brought down due to collisions (a predominant feature of LTE) with other particles in the plume, as they propagate.

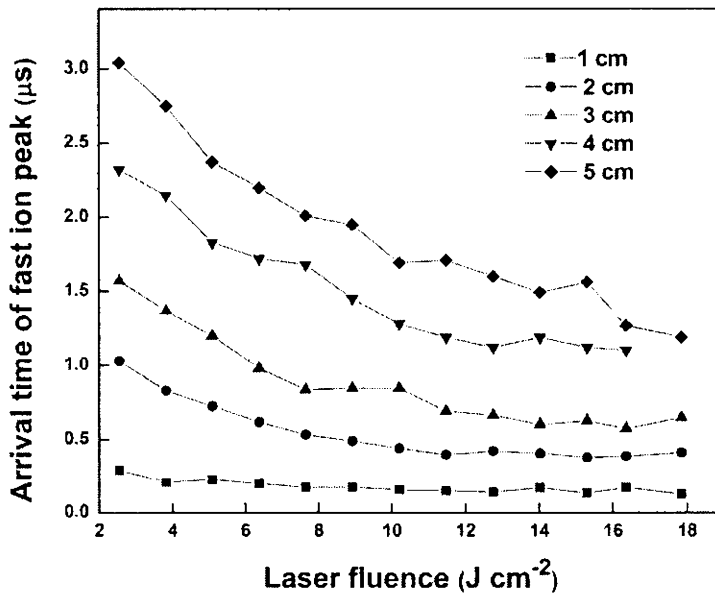


Fig. 4.4 Variation of arrival time of fast ion peaks with laser fluence

The hot ion velocities at 4 cm distance from the target are respectively 13 km/s and 33 km/s for the above laser pulse energies and corresponding ion energies are 59 eV and 386 eV. The order of zinc ion energy at this distance agrees with the observations of Claeysens et al [29]. They also have reported that zinc ions in the plume have greater velocities compared to neutral zinc and neutral oxygen

present in the plume, justifying the contention that ions gain additional velocity over neutral particles due to the phenomenon of DL occurring in laser ablated plasma. Ions with energies in the range of 900 eV [32] have been reported for laser produced plasma. TABLE 4.1 illustrates a comparison of the energies of fast and thermal ions in vacuum at various laser fluencies and distances.

TABLE 4.1 Fast ion kinetic energies (E_f) and thermal ion kinetic energies (E_t) at 1 and 4 cm distance for various laser energy.

| Laser Fluence (Jcm^{-2}) | 1 cm | | 4 cm | |
|---------------------------------|------------|------------|------------|------------|
| | E_t (eV) | E_f (eV) | E_t (eV) | E_f (eV) |
| 7.65 | 19.6 | 1160 | 8.57 | 135 |
| 10.2 | 23.8 | 1410 | 9.5 | 192 |
| 12.75 | 47.5 | 1750 | 12.7 | 214 |
| 15.3 | 59.2 | 1960 | 17.3 | 225 |
| 17.85 | 74 | 2220 | 23.4 | 386 |

The thermal ions on the other hand exhibited very low energies compared to fast ions but in reference to the energy (or velocity) of the neutrals, the energies of the thermal ions are nearly double (refer Fig. 3.5). At 1cm distance from the target thermal ion energies varied from 13.5 eV ($\sim 6.33 \text{ kms}^{-1}$) at 2.55 J cm^{-2} to 74 eV ($\sim 14.6 \text{ kms}^{-1}$) at 17.85 J cm^{-2} laser fluence. This means that ions are in general accelerated due to the ambi-polar electric field with very few of them acquiring very high velocities (hot ions). The forgoing discussions suggest that the leading edge of the expanding LIP plume is predominantly populated with

ions of both kind, following behind are neutrals of varying propagation velocities and at the rear with thermal electrons.

ZnO thin films grown by PLD in vacuum were highly amorphous and non-uniform when substrate was placed closer to the target and also when high laser power was used for ablation. The film gained crystallinity, stoichiometry, and transparency when substrate placed at 6 cm distance and ablated at low laser powers [33]. At points near to the target and at high laser powers the ion energy is of the order of keV. The high energy ions bombard the substrate and may cause re-sputtering from the substrate, defect formation etc. The substrate placed beyond 5 cm from the target surface and the ablation at low laser powers favors the film growth.

(a) Effect of pressure

The ion TOF spectra in the N₂O ambience do not show twin peaks as distinct as those obtained in vacuum. The increase in ambient gas pressure decreases the flux of thermal ions reaching the probe. The cross-section for scattering of ions due to collision with particles in the plume follows inverse relationship with ion energy [34]. Hence the fast ions having very high energy are scattered less and they literally plough through the plume and reach the collector. When the pressure is increased the thermal ions are scattered more and hence the thermal ion current become too small, along the target normal, to be detected along with that of fast ions.

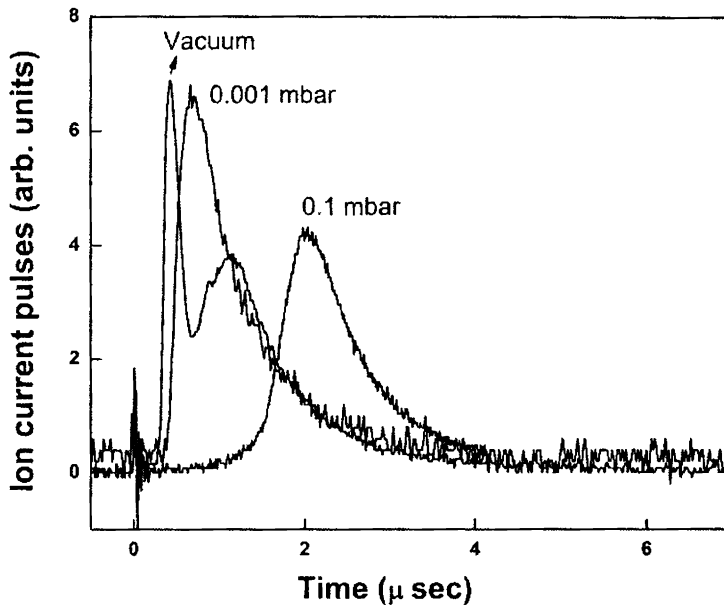


Fig. 4.5 Variations of ion TOF with ambient gas pressure at 2 cm distance from the target and laser fluence of 12.75 Jcm^{-2} .

The peak positions are shifted to the longer time regime and pulse heights diminished with increase in ambient gas pressures. That is the average velocity and fast ion flux decreased with ambient gas pressure. The Fig. 4.5 represents influence of various N_2O ambiances on TOF spectra at 2 cm away from the target and laser fluence of 12.75 Jcm^{-2} . The fast ions reaching the probe are delayed with increase in the N_2O ambient pressure. The fast ion peak of the TOF in vacuum is very sharp as compared to those in N_2O atmosphere. Thus the ambient gas pressure produces large spread in the kinetic energies of ions in the plume. The delay in the arrival of ions to the probe can be attributed to the impedance offered by the presence of gas [30, 35-37] to the forward propagation

velocity of the plume. The absence of thermal ion peak with increase in ambient pressures may also be due to the reasons listed below.

- (i) As the pressure is increased the mean free path of electrons and ions in the plume is reduced due to shrinking of the plume thereby causing greater probability for electron- ions recombination.
- (ii) There occurs change in the shape of the plume with increase in gas pressure. In vacuum the plume is highly forward directional so that the ions are all confined to small solid angle, while as the pressure is increased the plume shrinks and assumes hemi-spherical shape [37,38], thereby increasing the angular distribution of ions. Therefore in the later case ion flux reaching the probe, positioned along the target normal collects lesser number of ions compared to that in vacuum or at low ambient pressures.

The Fig. 4.6 represents the arrival time of hot ion peak at various probe positions for TOF spectra recorded when ablated at 0.001 mbar N_2O pressure. Comparison of this with Fig. 4.4, where TOFs were taken in vacuum and similar laser fluences, shows the delay in the arrival of fast ion to the probe. This can be attributed to the impedance offered by the N_2O ambience on the plume propagation. This delay increased with increase in ambient pressures. At very high ambient pressure (~ 0.1 mbar) the ion current pulses were very weak and hence comparison of peak arrival time with those in vacuum was difficult beyond 2 cm distance from the target. This substantiates the phenomenon of increase in the electron-ion recombination processes leading to suppression of twin peaks in the ion TOF spectra recorded in the background gas.

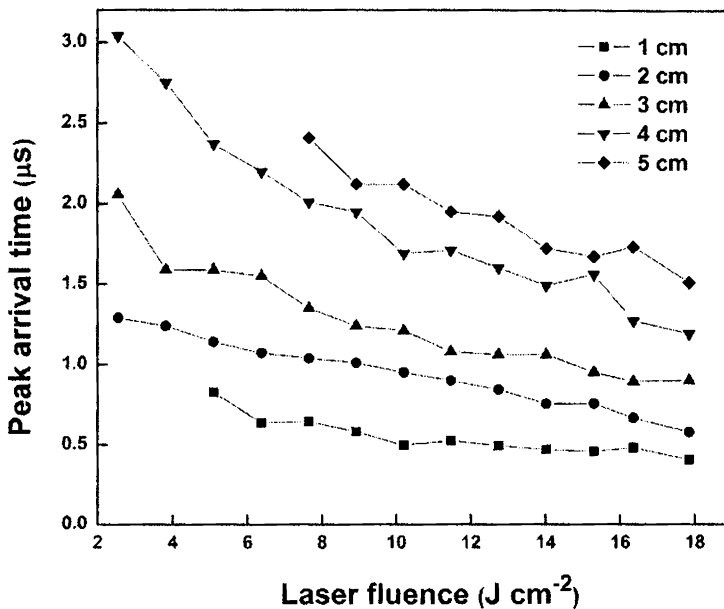


Fig. 4.6 Variations of average arrival time of fast ions with laser fluence at various spatial positions of the probe from the target and TOF spectra recorded under the N₂O ambient pressure of 0.001 mbar.

4.4.2 Electron time of flight

The TOF spectra of electrons accompanying pulsed laser ablation in vacuum and also in the N₂O ambiances, its behavior with variations in laser fluence and Langmuir probe positions merit elaborate considerations. All TOF spectra of electrons were recorded with the probe bias voltage of + 30 V as at this voltage the electron TOF's became independent of the probe bias (electron saturation regime). As described earlier, DL is formed due to fast (hot) electrons generated in the early stages of plume expansion. These electrons escape from the main body of the plume.

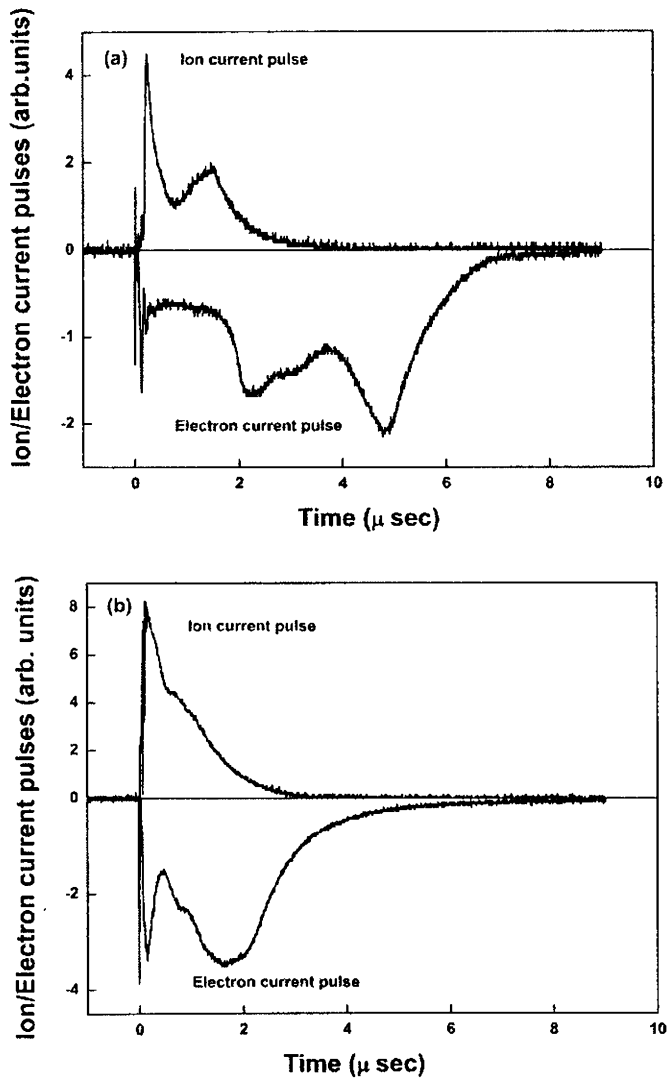


Fig. 4.7 Ion and electron TOF spectra recorded at 1cm distance in vacuum when ablation was carried out at laser fluencies (a) 5.1 Jcm^{-2} and (b) 17.85 Jcm^{-2} .

The TOF spectra of electrons exhibit the presence of slow or thermal electrons of two different energies along with the tail (slower component) of hot electrons. The velocities of hot electrons are in the same order as that of fast (accelerated) ions (Refer Fig. 4.4 and Fig.4.10). Decay of electron current pulses is slow at low laser fluences and at points away from target, compared to ion current pulses.

A comparison of ion and electron TOF spectra recorded in vacuum at 1cm distance from the target for laser fluences of (a) 5.1 Jcm^{-2} and (b) 17.85 Jcm^{-2} is given in figure 4.7. The two types of thermal electron peaks are prominent only at reduced laser fluences. At 1 cm distance from the target, the two species of thermal electrons have velocities 5 km/s and 2 km/s for the laser fluence of 5.1 Jcm^{-2} . These velocities are very small compared to those of thermal ions indicating that electrons are severely decelerated and move behind thermal ions during plume propagation. When ablation was carried out with higher laser fluences the temporal separation of the two kinds of thermal electrons gradually decreased. At the highest laser fluence (17.85 J cm^{-2}), both species of thermal electrons merged into a single broad peak with an average velocity of 6 km/s [Fig. 4.7 (b)]. The hot electron peak is very narrow indicating that hot electrons are ultra fast and short lived and only the tail (slower component) of the hot electrons generated in the ablation process is recorded by our instrument as the rest escapes from the main body of the plume at a very rapid pace.

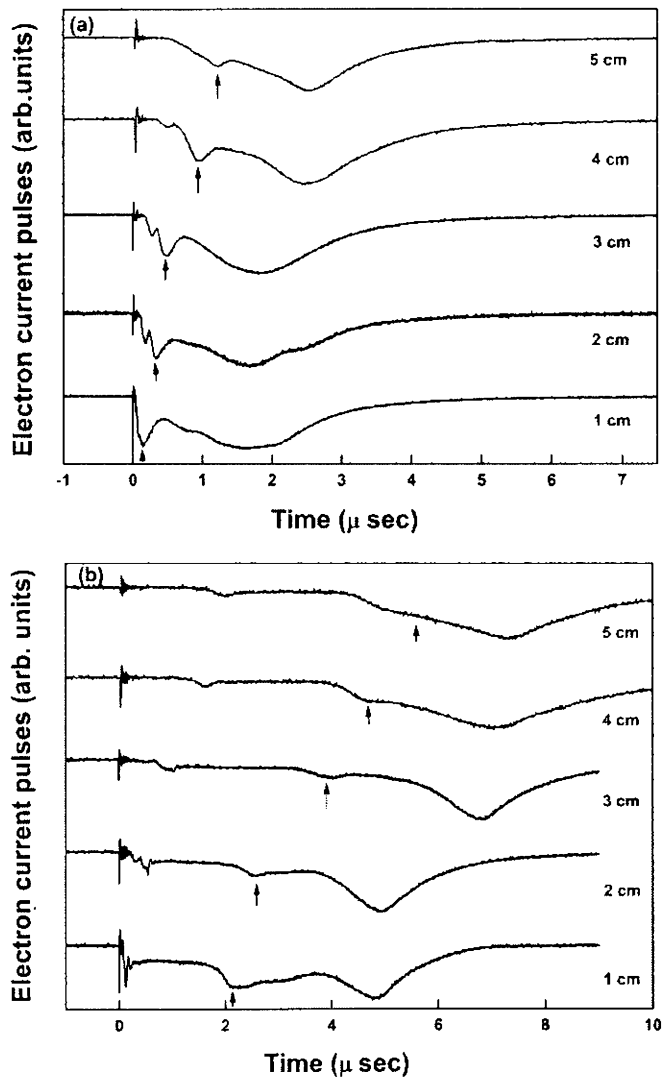


Fig. 4. 8 Spatial behavior of electron TOF spectra recorded in vacuum at laser fluences (a) 17.85 Jcm^{-2} and (b) 5.1 Jcm^{-2} . (Arrows indicate the faster component of thermal ions)

The Figure 4.8 depicts the electron time of flight at various spatial positions of the plume when target was ablated in vacuum at two widely different laser fluences, (a) 17.85 Jcm^{-2} and (b) 5.1 Jcm^{-2} . TOF spectra indicate that majority of the electrons fall on the low energy side of thermal electrons. The arrival of all species of electrons is delayed with increase in probe distance from the target. The faster components of the thermal electron pulses are indicated with arrow marks. The two types of thermal electrons showed large temporal separation at low laser pulse energies and the faster component of thermal electrons becoming less prominent at large distance from the target. The presence of hot electrons, even though small, is detected in the TOF spectra recorded at all spatial positions and laser fluences. The hot electron peak is not well resolved at 1 cm distance from the target, but is better resolved as plume advances in space.

The figures 4.8 (a), where, the TOF's were recorded at high laser fluence the thermal electrons are centered around $2 \mu\text{s}$ in time scale. As the laser fluence is decreased, the thermal electrons get severely delayed with thermal electron peak arrival time approaching $8 \mu\text{s}$ [Fig. 4.8 (b)]. Various TOF spectra suggest that electrons reach the probe several microseconds after the termination of ion current pulse. This means that the electrons were trailing behind the main body of the plume and continue to move forward due to the energy acquired during the ablation process. The reason for the thermal electrons getting pushed back from the plume or severely decelerated can be well substantiated due to the effect of DL in LIP, illustrated in Figure 4.1.

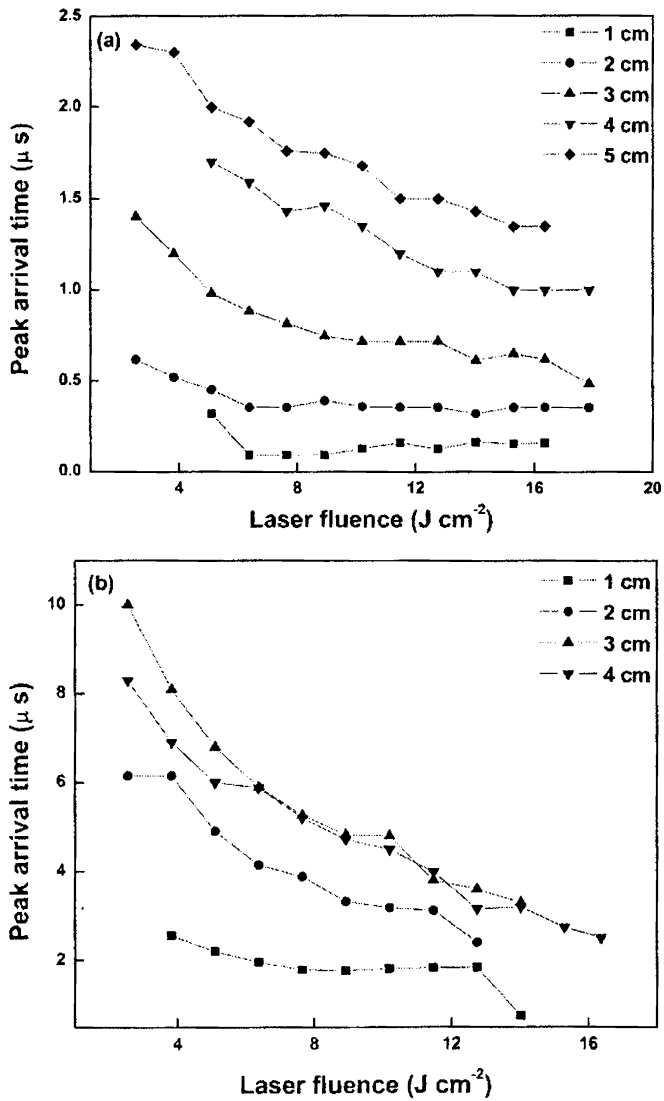


Fig. 4. 9 The spatial variations of average arrival time of (a) fast electrons and (b) thermal electrons with laser fluences in vacuum.

The TOF of electrons recorded at high laser fluences [Fig. 4.7(b)] do not show thermal electrons of two different energies because at this laser fluence the average Maxwellian kinetic energies of all electrons diffusing from region C must be sufficiently high to overcome the potential step Φ of region B [refer Fig. 4.1] and hence form a broader thermal electron peak. As the laser fluence was reduced the temporal separation of the two kinds of thermal electrons increased steadily. Figure 4.7 (a) shows the electron TOF in vacuum for laser pulse energy of 5.1 J cm^{-2} , the electron current persisted up to $8 \mu\text{s}$, very much delayed, even after the termination of ion current pulse. For larger distance of the probe from the target, the electrons were delayed up to $10 \mu\text{s}$ [Fig. 4.8 (b)].

The reduction in the laser fluence results in the reduction of fast electrons and majority of the electrons fall in the thermal electron category. The figures 4.9 (a) and (b) are the plots of peak arrival time of hot and thermal electrons. Both kinds of thermal electrons showed similar spatial behavior. The hot electron peak velocity in vacuum is in agreement with those of fast ions, justifying earlier reports that ions are very much accelerated due to DL and attain velocities comparable with those of fast electrons.

(a) Effect of pressure

The increase in the ambient gas pressure has caused suppression of the thermal electrons and slowing down of the fast electrons. Signature of the presence of thermal electrons is found in the TOF spectra taken at points closer to the target [Arrow marks in Fig. 4.10 (b)]. This kind of thermal electrons were found only at low laser fluence. As the laser fluence was increased the electron TOF spectra exhibited only fast electrons [Fig. 4.10 (a)].

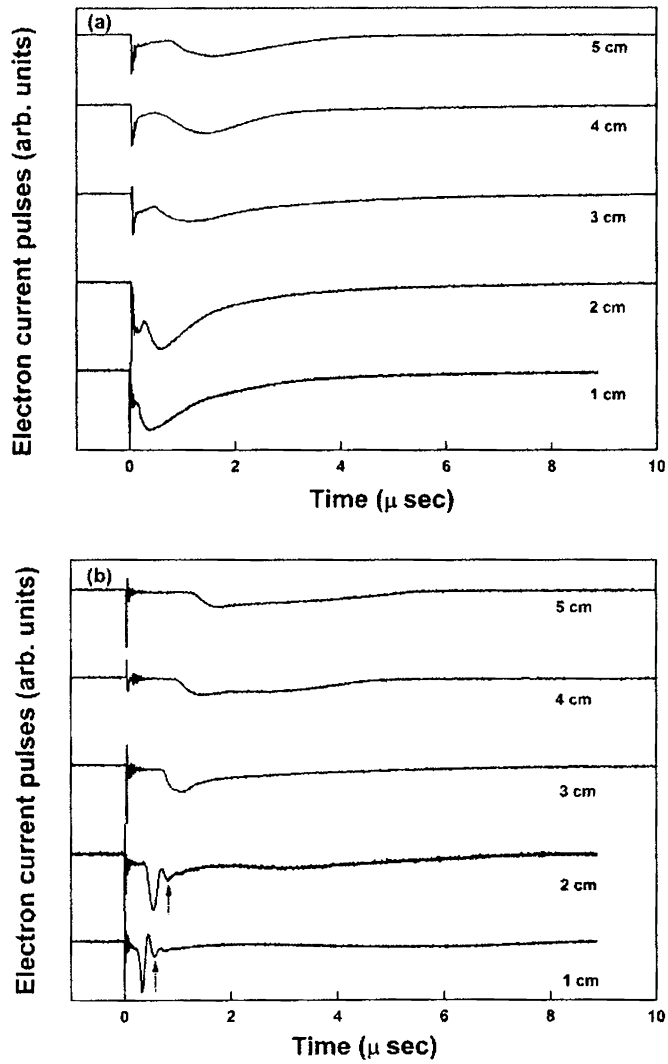


Fig. 4.10 Spatial behavior of electron TOF recorded in the ambient gas pressure of 0.001 mbar and ablated with (a) 17.85 Jcm^{-2} and (b) 5.1 Jcm^{-2} laser fluences.

Even at low laser fluence as the probe is moved away from the target only fast electrons with delayed TOF were observed. It has been mentioned earlier that the plume expands isothermally from the moment the leading edge of the laser pulse hits the target, to the termination of the pulse. There after the plume expansion is adiabatic and it will have very high pressure gradient directed perpendicular to the target surface. This pressure gradient pushes the front portion of the plume against the impedance of the background gas while the rear portion of the plume which mainly consists of thermal ions, slow neutrals and thermal electrons, owing to less velocity, will receive greater impedance and might get detached from the front portion of the plume. This kind of phenomena, known as plume splitting exists in LIP where high fluence and ambient gas pressure are employed [39-43]. The rear portion of the plume fail to reach the collector placed at large distances from the target, accounting for the absence or suppression of thermal electrons or thermal ions in the respective TOF spectra recorded in ambient gas pressures. The effects of DL formation in the plume add to the probability of occurrence of plume splitting.

The plume density gets reduced as it propagates in space and the pressure gradient of the plume diminishes rapidly. This causes delay in the arrival of electrons and spread in the electron energy distribution as revealed from the elongated temporal profiles of electron TOF spectra at points away from the target surface. Another reason for the suppression of thermal electron in the electron TOF spectrum taken in the presence of high ambient gas is that unlike ions and neutrals present in the expanding plume the electrons in it exhibit greater angular distribution and the angular distribution increases with ambient gas pressure. Most of the thermal electrons move radially outward after the event of ablation and only fast electrons move closer to the target normal. The

fast electrons are less scattered and hence move ahead of the fast ions from the target surface making a small solid angle with propagation direction of the plume.

4.5 Conclusion

The occurrence of ambi-polar electric field due to DL formation in LIP is responsible for the observation of different energies of charged particles within the plume. The ion acceleration has caused some ions to attain energies comparable with that of electrons. The fast ion energy is of the order of keV in the vicinity of the target while at far away from target reduces energy to hundreds of eV when ablated in vacuum at high laser fluences. Thermal electrons continue to reach the probe for few microseconds more after the termination of ion current pulse when ablated in vacuum. They trail behind the main body of the plume and hence are not lost either by scattering due to collision with particles of the plume or by electron-ion recombination, for plume analyzed in vacuum. The presence of ambient gas results in slowing down of the ions and electrons and severe reduction in the number of thermal ions and electrons. In the context of ZnO thin film growth, low laser fluences for ablating the target is advisable. At high laser fluences the ions liberated having energies in the order of keV will hamper the uniformity and stoichiometry as these energetic particles hitting the substrate are capable of causing re-sputtering from the film. High ambient gas pressure is not desirable as the propagation length of the plume decreases with pressure particularly when the target is ablated at low laser fluences. The ambient gas pressure suppresses DL in ZnO plasma.

Reference

- [1] A. A. Plyutto, *Sov. Phys. JETP* **12**, 1106 (1961).
- [2] G. Hairapetian and R. L. Stenzel, *Phys. Fluids B* **3**, 899 (1991).
- [3] P. E. Dyer, S. A. Ramsden, J. A. Sayers, and M. A. Skipper, *J. Phys. D* **9**, 373 (1976).
- [4] J. S. Pearlman, J. J. Thomson, and C. E. Max, *Phys. Rev. Lett.* **38**, 1397 (1977).
- [5] P. Wagli and T. P. Donaldson, *Phys. Rev. Lett.* **40**, 875 (1978).
- [6] A. W. Elher, *J. Appl. Phys.* **46**, 2464 (1975).
- [7] D. B. Geohegan and A. A. Puretzky, *Appl. Surf. Sci.* **96**, 131 (1996).
- [8] R. F. Wood, J. N. Leboeuf, D. B. Geohegan, A. A. Puretzky, and K. R. Chen, *Phys. Rev. B* **58**, 1533 (1998).
- [9] K. Fukushima, Y. Kanke, M. Badaye, and T. Morishita, *J. Appl. Phys.* **77**, 5404 (1995).
- [10] G. Ulmer, B. Hasselberger, H.-G. Busmann, and E. E. B. Campbell, *Appl. Surf. Sci.* **46**, 272 (1990).
- [11] M. Tanaka, Y. Fujisawa, T. Nakajima, and Y. Tasaka, *J. Appl. Phys.* **83**, 3379 (1998).
- [12] A. J. Peurrung, J. P. Cowin, G. Teeter, S. E. Barlow, and T. M. Orlando, *J. Appl. Phys.* **78**, 481 (1995).
- [13] S. Sunil, A. Kumar, R. K. Singh, and K. P. Subramanian, *J. Phys. D: Appl. Phys.* **41**, 085211 (2008).
- [14] S. Eliezer and H. Hora, *IEEE Transactions on Plasma Science*, **17**, 2290 (1989).

- [15] Y. B. Zeldovich and Y. P. Raizer, “*Physics of Shock Waves and High-Temperature Hydrodynamic Phenomena*” (Academic Press), New York, (1996).
- [16] B. Bezzerides, D. W. Forslund, and E. L. Lindman, *Phys. Fluids* **231**, 2179 (1978).
- [17] R. L. Morse and C. W. Nielson, *Phys. Fluids* **16**, 909 (1973).
- [18] M. Kimura, M. Inokuti, and M. A. Dillon, *Adv. Chem. Phys.* **84**, 193 (1993).
- [19] M. Widner, I. Alexeff, and W. D. Jones, *Phys. Fluids* **14**, 695 (1971).
- [20] J. E. Crow, P. L. Auer, and J. E. Allen, *Plasma Phys.* **14**, 65 (1975).
- [21] B. Bezzerides, D. W. Forslund, and E. L. Lindman, *Phys. Fluids* **231**, 2179 (1978).
- [22] R. S. Ajimsha, M. K. Jayaraj, and L. M. Kukreja, *J. Elelctron. Mater.* (DOI: 10.1007/s11664-007-0365-4).
- [23] R. S. Ajimsha, K. A. Vanaja, M. K. Jayaraj, P. Misra, V. K. Dixit and L. M. Kukreja, *Thin Solid Films*, **515**, 7352 (2007).
- [24] S. M. Jejurikar, A. G. Banpukar, A. V. Limaye, S. K. Date, S. I. Patil, K. P. Adhi, P. Misra, L. M. Kukreja and R. Bathe, *J. Appl. Phys.* **99**, 014907 (2006).
- [25] P. Misra, T. K. Sharma, S. Porwal and L. M. Kukreja, *Appl. Phys. Lett.* **89**, 161912 (2006)
- [26] A. Suzuki, T. Matsushita, T. Aoki, Y. Yoneyama and M. Okuda, *Jpn. J. Appl. Phys.* **38**, L71 (1999).
- [27] N. M. Bulgakova, A. V. Bulgakov and O. F. Bobrenok, *Phy. Rev. E* **62**, 5624 (2000).

- [28] P. Mannion, S. Favre, G. M. O Connor, B. Doggett, J. G. Lunney, and T. J. Glynn, Proc. of SPIE, **2827**, 457 (2005).
- [29] F. Claeysens, A. Cheesman, S. J. Henley, and M. N. R. Ashfold, J. Appl. Phys. **92**, 6886 (2002).
- [30] K. J. Saji, N. V. Joshy, and M. K. Jayaraj, J. Appl. Phys. **100**, 043302 (2006).
- [31] S. Namba, R. Nozu, and K. Takiyama, J. Appl. Phys. **99**, 073302 (2007).
- [32] S. S. Harilal, C. V. Bindhu, M. S. Tillack, F. Najmabadi, and A. C. Gaeris, J. Phys. D: Appl. Phys. **35**, 2935 (2002).
- [33] R. Manoj, A. Antony, C. Vineeth, and M. K. Jayaraj, *Proceeding of DAE-BRNS National Laser Symposium, India* (2002).
- [34] M. Kimura, M. Inokuti, and M. A. Dillon, Adv. Chem. Phys. **84**, 193 (1993).
- [35] S. Amoruso, R. Bruzzese, N. Spinelli, and R. Velotta J. Phys. B **32**, R 131 (1999).
- [36] F. J. Gordillo-Vazquez, A. Perea, J. A. Chaos, J. Gonzalo, and C. N. Afonso Appl. Phys. Lett. **78**, 7 (2001).
- [37] S. Amoruso, B. Toftmann, and J. Schou, Phy. Rev. E **69**, 056403 (2004).
- [38] S. Yalçın, Y. Y. Tsui, and R. Fedosejevs, IEEE Transactions on Plasma Science, **33**, 2 (2005).
- [39] S. S. Harilal, C. V. Bindhu, M. S. Tillack, F. Najmabadi and A. C. Gaeris J. Phys. D: Appl. Phys. **35**, 2935 (2002).
- [40] R. F. Wood, J. N. Leboeuf, D. B. Geohegan, A. A. Puretzky and K. R. Chen, Phy. Rev. B, **58**, 1533 (1998).
- [41] A. Amoruso, B. Toftmann, J. Schou, R. Velotta and X. Wang, Thin Solid Films, **453**, 562 (2004).

- [42] S. Amoruso, A. Sambri, and X. Wang, *J. Appl. Phys.* **100**, 013302 (2006).
- [43] R. K. Thareja, H. Saxena and V. Narayanan, *J. Appl. Phys.* **98**, 034908 (2005).

CHAPTER V

Characterization of ZnO plasma in a Radio Frequency sputtering system

Abstract

Plasma generated by the radio frequency (RF) magnetron sputtering of gallium doped zinc oxide (ZnO) has been studied using cylindrical Langmuir probe and optical emission spectroscopy. The electron density and electron temperature were calculated for various RF powers at different spatial positions along the propagation direction of the plume. The electron density was found to increase with argon gas pressure whereas electron temperature decreased. The focusing of the plasma due to the magnetic field of the magnetron was observed at 3 cm distance from the target at low RF powers while shift in the focusing of the plume was observed for high sputtering powers. Plasma potential of the plume was evaluated at all sputtering conditions and its spatial variations determined. Optical emission spectra of the plume were recorded at various spatial positions of the plume to get qualitative estimate of species in the plasma at various sputtering conditions. ZnO thin films were deposited on glass substrates placed at 3 cm and 6 cm distances from the target, at different sputtering conditions. X-ray diffraction (XRD) and scanning electron microscopy (SEM) analysis were carried out to investigate the crystallographic properties and the surface morphology of films.

5.1 Introduction

RF magnetron plasma is altogether a different kind of plasma compared to laser induced plasma (LIP) in terms of the electron density, electron temperature, plume size and kinetic behavior. Even though RF magnetron plasma is not as transient as LIP, there always occur fluctuations in the plasma. The electrons take up spiraling or cycloidal motion above the target, which is placed in the gun fixed at the base of the chamber. These particles undertake numerous collisions, which in turn produces more ionization and hence causes increased sputter rate. The plasma generation is complicated in the sense that proper care and attention should be given in designing of the sputter chamber and the magnetron gun. In addition to the nonreactive gas (argon or xenon) required for the sputtering process, reactive gas (usually oxygen for oxide film deposition) is introduced in to the chamber for assisting proper film deposition. The main advantage of the RF plasma assisted thin film deposition is the large area coverage and relatively low temperature of the substrate compared to thin film deposition by PLA. The plasma produced by RF magnetron with co-sputtering set-up is effectively employed in the fabrication of thin film transistors (TFT's) [1-3]. ZnO based thin films and devices, of opto-electronic importance have also been fabricated in our laboratory [4-7] using RF magnetron sputtering. There are reports of smooth ZnO films deposition at low temperatures [8,9]. The RF magnetron plasma of ZnO:Ga is studied using optical emission spectroscopy and Langmuir probe. This study was taken up to get an insight in to the RF plasma behavior with variations in the RF power, ambient gas and distance from the target so as to optimize the input sputtering conditions.

5.2 Experimental set-up

Target was prepared by doping ZnO (99.9 % pure Aldrich) with 5 wt. % Ga₂O₃ (Alfa Aesar, 99.99 % purity) and sintered at 1000⁰ C for 8 hours. The target holder was of two-inch diameter. The sputter chamber was evacuated to the base pressure of 10⁻⁶ mbar using diffusion pump. The working pressure employed in the sputtering process were 0.001 mbar, 0.005 mbar and 0.01 mbar, maintained using high purity (99.99 %) argon gas introduced in to the chamber using mass flow controller. The RF power at 13.56 MHz was varied from 25 W to 200 W in step of 25 W and the plasma plume was studied using RF compensated cylindrical Langmuir probe (probe diameter 0.5 mm and length 5 mm) positioned perpendicular to the plume propagation direction. Great care was taken to prevent the probe feed wires and glass covering of the probe from being exposed to plasma since this could affect the measured probe current. A high speed voltage ramp for biasing the probe and simultaneous probe data acquisition set-up [described in section 2.4] was used for acquiring graphical representation of probe currents. The ion and electron current data were averaged over 10 voltage sweeps. The sputtering chamber was properly grounded using thick copper strip to eliminate any RF interference during probe biasing and data acquisitions.

A 1:1 image of the plume was obtained using proper optics and the optical emissions from various spatial positions along the propagation direction of the plume were collected using an optic fiber bundle. The wavelength dispersed spectra of the plume were recorded with monochromator-CCD assembly. ZnO thin films were deposited on glass substrates at room temperature, for target to substrate (T-S) distances of 3 cm and 6 cm, at different sputtering conditions. X-ray diffraction (XRD) (Rigaku, with Cu-K α radiation, 1.5414 Å) and scanning

electron microscopy (SEM) (JEOL JSM 5600) studies were carried out to investigate the crystallographic properties and the surface morphology of films deposited at these distances, in relation with the plasma parameters.

5.3 Results and discussions

5.3.1 Langmuir probe measurement

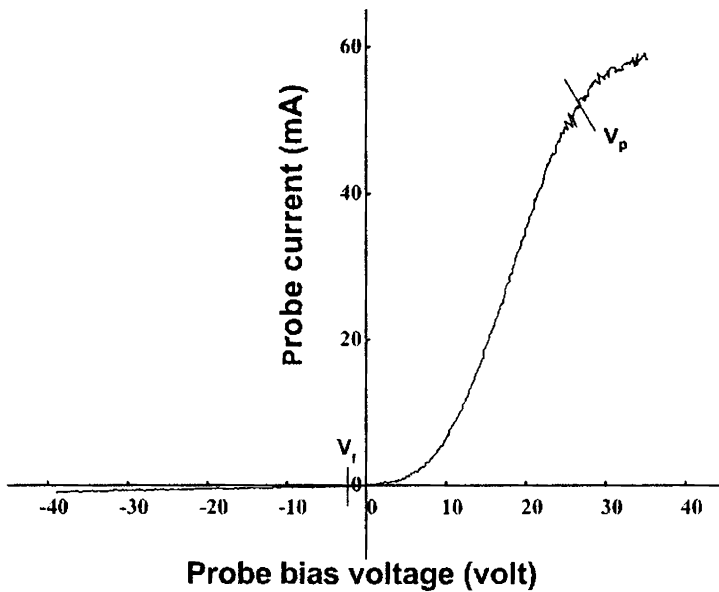


Fig. 5.1 Typical Langmuir probe current – voltage characteristic recorded at 5 cm distance from the target

A typical Langmuir probe current - voltage characteristic of the RF plasma is shown in figure 5.1. The floating potential (V_f) of the plasma is the probe bias for which the ion current equals electron current. This was estimated from the intersection of the characteristic with the voltage axis. When the potential applied to the probe is greater than the space (plasma) potential (V_p), the

electrons from the plasma are attracted to the probe and the ions repelled. The V_p is marked by the change in the slope of the $I-V$ characteristic. The electron temperature (kT_e), ion/electron density (N_e) and plasma potential V_p are calculated respectively using equations 1.48, 1.58 and 1.59. The portion of the $I-V$ characteristic below -10 V was used in the calculation of ion density in order to eliminate the error in the probe current due to the contribution of highly energetic electrons coming on to the probe. The probe theory is discussed in detail in section 1.6.2.

(a) Ion density (N_e)

The plasma plume at 3 to 4 cm distance from the target was found to have maximum ion number density when high RF powers were employed in the sputtering. For low RF powers, the ion density peaked precisely at 3 cm distance from the target. The variation of ion density with distance of the probe from the target is shown in the figure 5.2 (a). The measurements were carried out by varying RF power at an argon pressure of 0.005 mbar.

Similar behavior was exhibited when sputtering was carried out under other ambient argon gas pressures. The variation of ion density with a maximum for each RF power could be attributed to the focusing of the ionic constituents of the plasma by the magnetic field of the magnetron. At high RF powers, the number density as well as the particle kinetic energy increases. This causes a forward thrust which eventually shifts the focal point of the plasma. The increase in kinetic energy of the ion is evident from the increase in the plasma potential with RF power (Fig. 5.4).

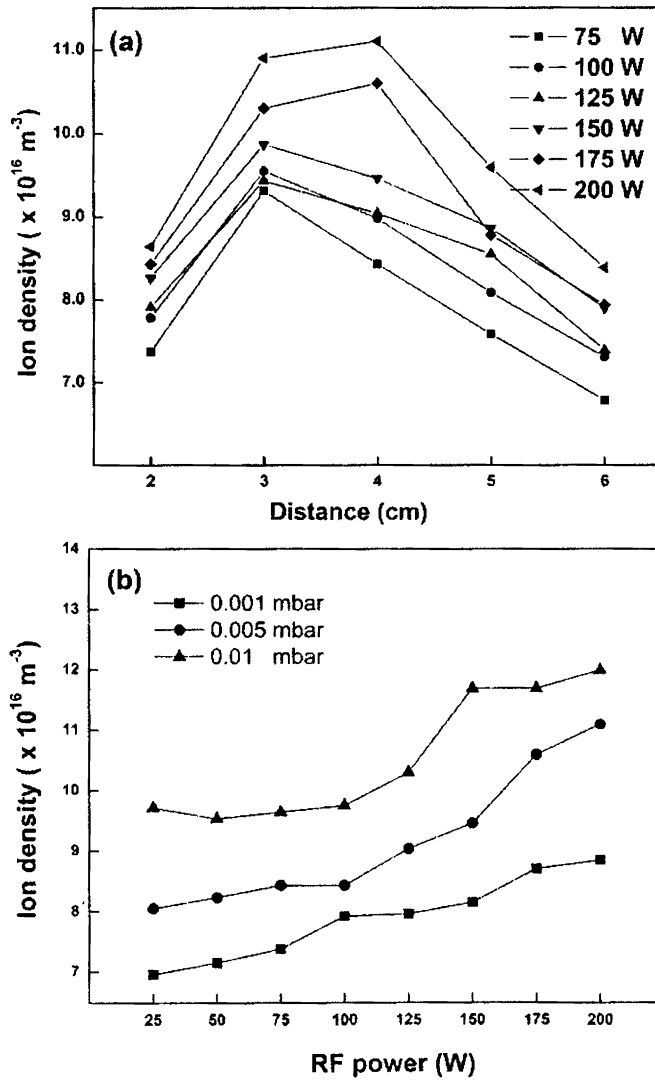


Fig. 5.2 (a) Spatial variation of ion density (N_e) with RF power at 0.005 mbar argon pressure, (b) dependence of sputtering gas pressure on N_e over various RF powers.

The ion density is found to increase with increase in ambient gas pressure [Fig. 5.2 (b)] for all spatial positions of the probe. This behavior is expected, since the increase of sputtering gas pressure increases the collision rate, thereby causing increase in the ionic species of the plume.

(b) Electron temperature (kT_e)

The plasma exhibited a steady increase in electron temperature (kT_e) with increase in RF power at all spatial positions from the target surface and for all argon gas pressures [Fig.5.3 (a) and (b)]. Closer to the target the electron temperature was high but decreased with increase of distance.

The main effect of increasing the RF power is to generate a large number of high energy ions (or electrons). These charged particles having energy above the ionization threshold of argon atom are capable of producing more argon ions which further increase the sputtering rate and thereby produce next generation electrons. As these electrons move up with the body of plasma, continuously lose energy until they become incapable of producing ions further by collision process. The energy loss is less pronounced at points closer to the target. The kT_e values evaluated from the probe characteristics recorded at 0.005 mbar argon pressure for various RF powers and distances from the cathode is shown in figure 5.3 (a). At 2 cm distance from the target, the electron temperature varied from 1.72 eV to 3.25 eV, while at 6 cm the variation was from 0.87 eV to 1.5 eV for the increase of RF power from 50 W to 200 W.

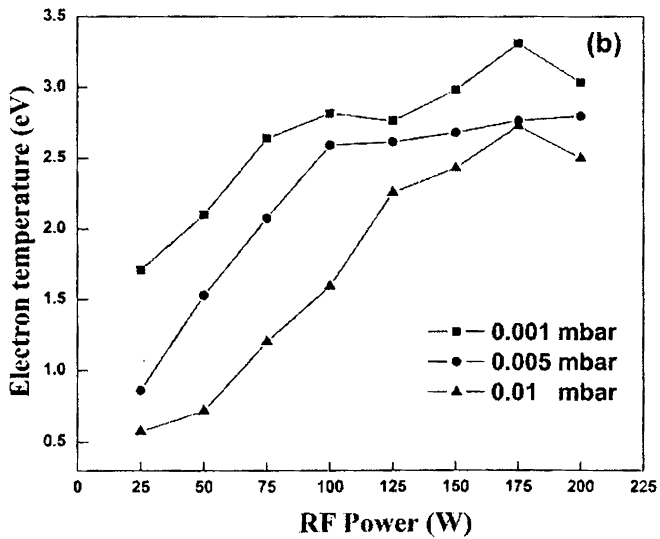
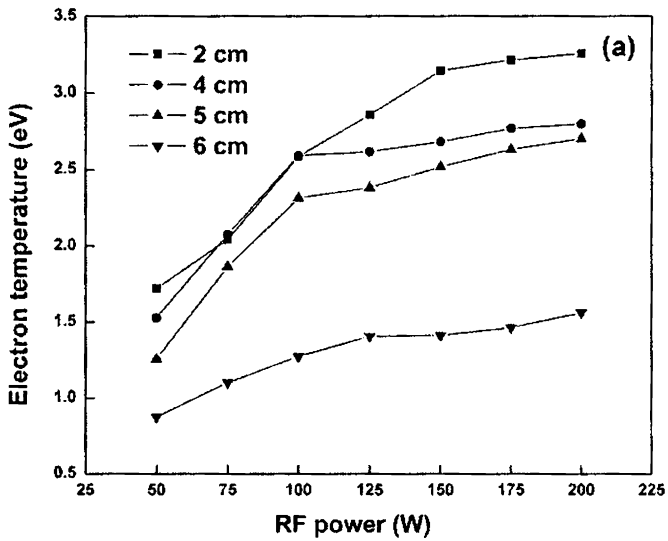


Fig. 5.3 (a) Spatial variation of electron temperature with RF power (argon pressure: 0.005 mbar), (b) dependence of sputtering gas pressure on electron temperature (probe position: 4 cm from the target)

The electron temperature decreased with increase in argon pressure where as the electron density variation was just the reverse. Figure 5.3 (b) shows the variations of electron temperature with argon pressure at 4 cm distance. Similar behavior of kT_e and N_e are reported in RF plasma [10, 11]. The RF sputtering of ZnO reported by Nagata et al [12] have a very high value (above 15 eV) for electron temperature. The electron temperature follows an inverse relationship with probe current [Eq.1.48]. Only very low value of electron current (less than 2 μ A) is reported in their work. The electron currents in corona plasmas are many orders (usually tens of milli-ampere) high [10, 11, 13] yielding electron temperatures around 5 eV.

(c) Plasma potential (V_p)

Plasma potential is an important parameter which gives information regarding the kinetic energies of the ionic species present in the plasma. V_p was found to increase with increase in RF power while the increase in argon gas pressure effected a decrease in V_p . The plasma potential is dependent on the screening of the electric field along the plasma sheath. Hence at high gas pressures more number of charged particles gets in to the plasma sheath, causing the screening of electric field to be more effective. Thus, as the pressure increases, plasma potential decreases. The increase in RF power increases the electric field in the plasma bulk causing less effective screening by the plasma sheath. As a consequence the plasma potential increases with increase in input RF power (Fig.5.4).

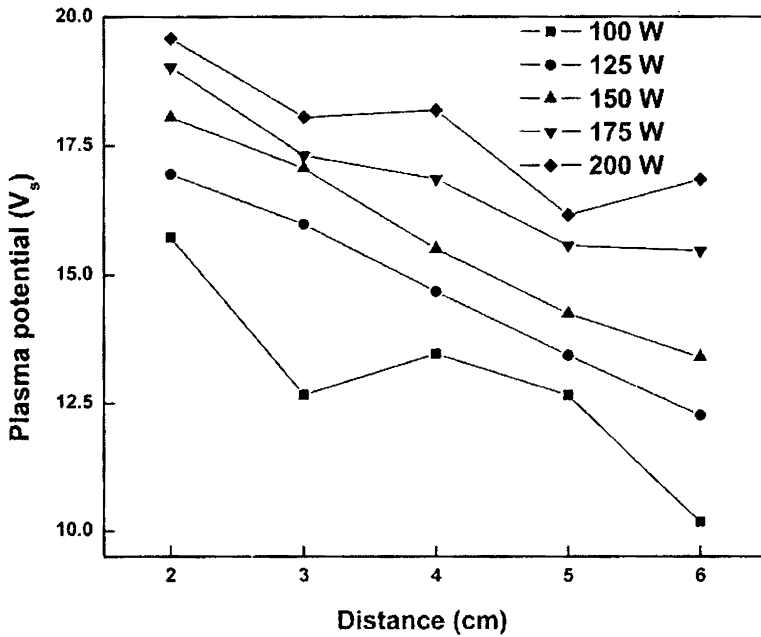


Fig.5.4 Spatial variation of plasma potential at 0.01 mbar argon gas pressure.

The increase in argon pressure results in an overall decrease in the plasma potential [14] in ZnO plasma. At high argon gas pressure the plasma potential showed a steady decrease with increase in distance from the target. However at very low argon gas pressure, the plasma potential was insensitive to spatial variations at all RF powers. The plasma potential gradient $\left(\frac{dV_p}{dz}\right)$ was negative along the propagation direction of the plasma and its magnitude increased with increase of argon pressure.

5.3.2 Optical emission spectroscopic (OES) studies

Optical emission spectroscopic (OES) studies were carried out on the plasma generated at various RF powers in the argon ambient gas pressure of 0.01 mbar. The spatial variations of emission intensities of different species in the plume were investigated as a function of RF power. Figure 5.5 shows typical OES spectra. Several strong emission lines of argon neutral (Ar I) were found in the wavelength range 700 nm to 850 nm. The Ar I emission lines in the green region of the spectrum were found very weak at all RF powers. Emission lines of zinc neutral were also recorded with high intensity.

Spectral emissions from neutral and singly ionized gallium (not marked in the figure) were found with very low intensity. All the prominent lines in figure 5.5 (b) are those of argon neutral. Oxygen emission lines in its atomic or ionic states have not been detected in this investigation. Also the emission line corresponding to Zn II (492.40 nm, $4d^2D_{5/2} - 4f^2F_{7/2}$) was recorded with very weak intensity. The Zn I emission lines at 468.01 nm ($4s\ 4p\ ^3P_0 - 4s\ 5s\ ^3S_1$), 472.21 nm ($4s\ 4p\ ^3P_1 - 4s\ 5s\ ^3S_1$), 481.05 nm ($4s\ 4p\ ^3P_2 - 5s\ ^3S_1$) and 636.23 nm ($4s\ 4p\ ^1P_1 - 4s\ 4d\ ^1D_2$) were recorded for RF powers above 50 W. Unlike the spectra of laser ablated ZnO plasma [15], the 636.23 nm emission line was found to be having greater intensity compared to other Zn I lines. This could be due to the fact that the momentum imparted during collision by argon having atomic weight 39.95 is more suitable for $4s\ 4p\ ^1P_1 - 4s\ 4d\ ^1D_2$ transition involving energy of the order $15713\ \text{cm}^{-1}$ while other zinc atomic transitions involve energy above $20000\ \text{cm}^{-1}$.

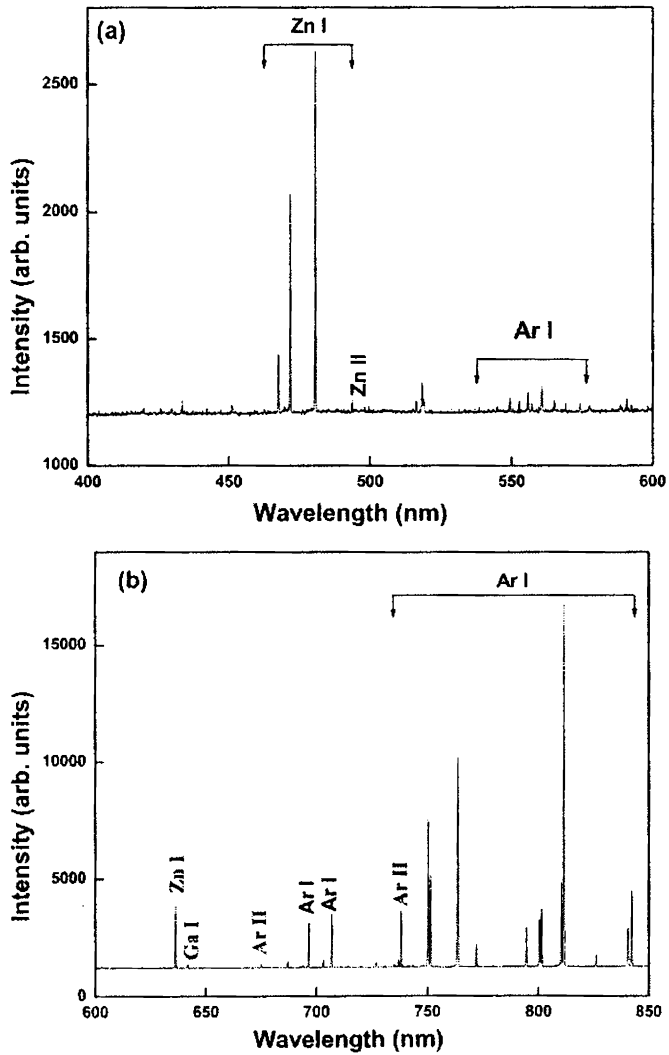


Fig. 5.5: Spectra of the plasma plume recorded at 1 cm distance from the target and the RF sputtering power of 150 W, recorded in the wavelength range (a) 400 nm to 600 nm, (b) 600 nm to 850 nm.

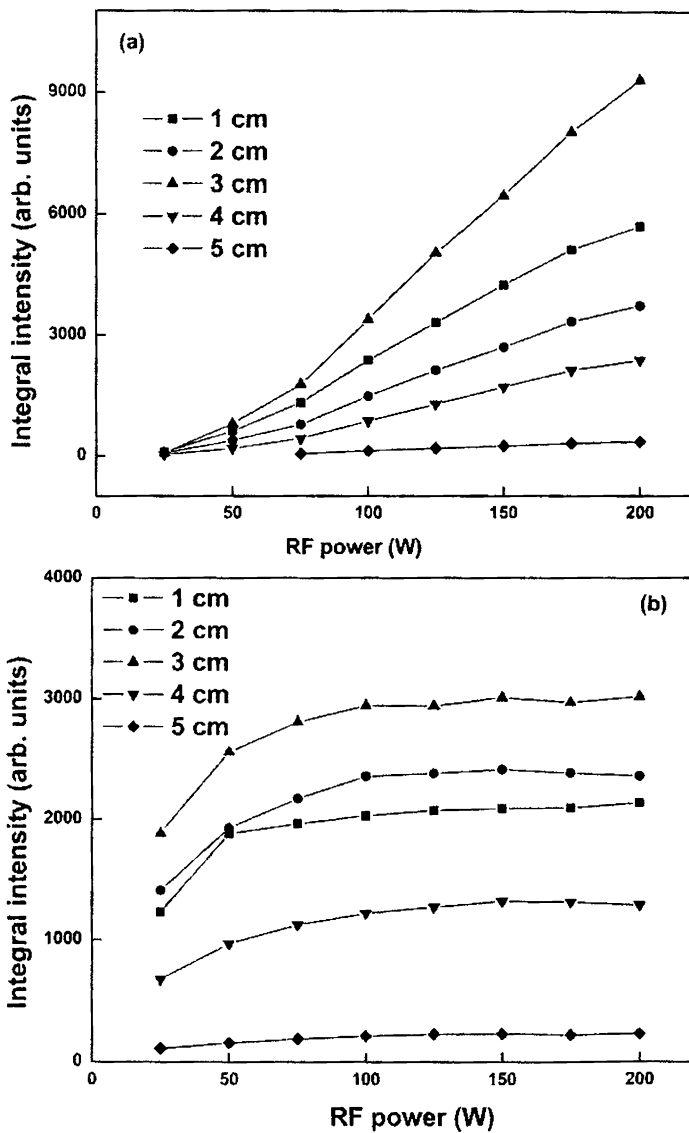


Fig. 5.6 The integral intensity variations of (a) Zn I (636.234 nm, $4s\ 4p\ ^1P_1 - 4s\ 4d\ ^1D_2$) and (b) Ar I (738.39 nm, $3s^23p^5\ (^2P_{3/2}^o) 4s - 3s^23p^5\ (^2P_{1/2}^o) 4p$) over distance and RF power variation

The integral intensity variations of Zn I (636.23 nm) and Ar I (738.39 nm) over distance and RF power variations are given respectively in figure 5.6 (a) and (b). The integral intensity of Zn I lines increased steadily with RF power at all distances from the target while the argon line intensity became almost steady beyond the RF power of 75 W. The integral intensity of all emission lines peaked at around 3 cm distance where the focusing of plume occurs due the magnetic field of the magnetron. This is in accordance with the Langmuir probe measurement of ion density becoming maximum around 3 cm distance from the target surface.

5.3.3 Thin film analysis

ZnO thin films were sputter deposited on glass substrates at room temperature for a target to substrate (T-S) distances 3 cm and 6 cm. These distances were chosen for film growth as the plasma parameters N_e , kT_e and V_s were very high at 3 cm and least at 6 cm. The depositions were carried out in argon ambient for a fixed duration of 20 minutes. The films were structurally characterized by x-ray diffraction analysis. Figure 5.7 (a) gives the XRD patterns of ZnO films deposited at the T-S distance of 6 cm for various RF powers. All the films were oriented along the (002) plane. The full width at half maximum (FWHM) was found to be the least (0.34°) for the film deposited at 100 W.

The films deposited at lower argon pressures were found to exhibit poor crystallinity. Figure 5.7 (b) compares the XRD patterns of the films grown at identical sputtering conditions, but for T-S distances of (i) 3 cm and (ii) 6 cm. It is observed that the XRD peak improved at the higher T-S distance in spite of the lowered deposition rate and subsequent lowering of the thickness of the

films. This ensures that better crystalline films can be grown at the T-S distance 6 cm under argon ambient of 0.01 mbar and RF power of 100 W.

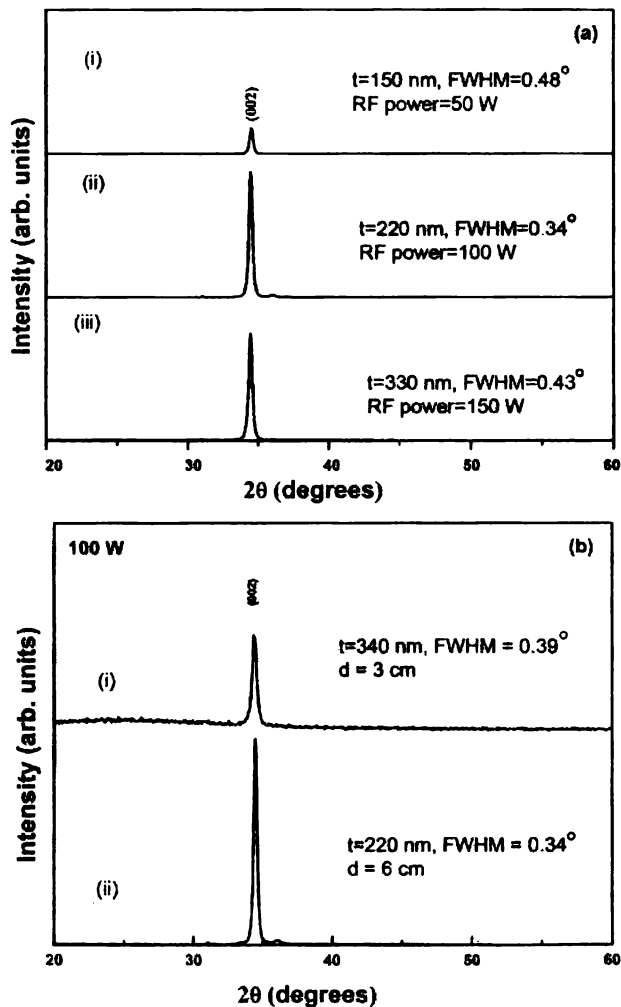


Fig. 5.7 (a) XRD patterns of the films deposited at the S-T distance of 6 cm and RF power of (i) 50 W, (ii) 100 W and (iii) 150 W (argon gas pressure of 0.01 mbar), (b) comparison of the XRD patterns of films grown at 0.01 mbar for an RF power of 100 W and S-T distance of (i) 3 cm and (ii) 6 cm.

SEM analysis of the films suggests that low sputtering power (~ 100 W) and high argon gas pressure (~ 0.01 mbar) are conducive for film growth, irrespective of T-S distance. Figure 5.8 (a-d) is the comparison of ZnO of thin films deposited at the substrate positions of 6 cm and 3 cm from the target for 0.01 mbar and 0.001 mbar argon pressure.

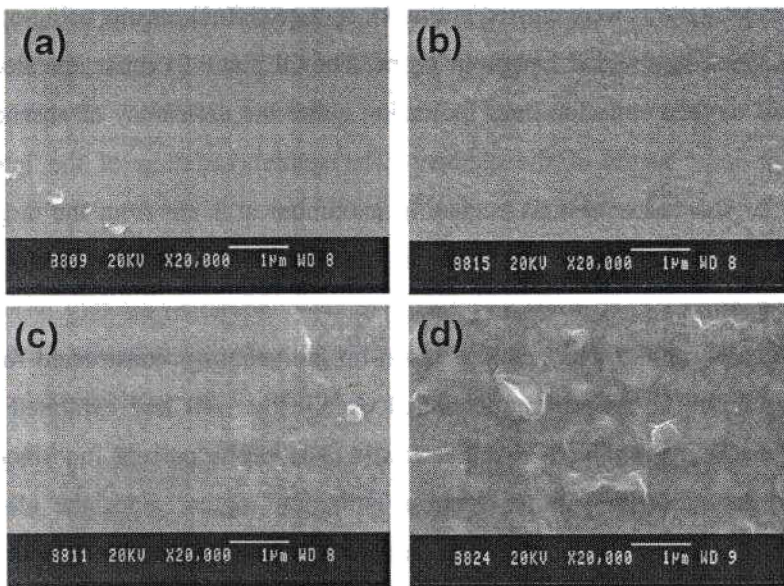


Fig. 5.8 SEM images of the ZnO films grown at 100 W under the sputtering conditions (T-S distance, Argon pressure) (a) (6 cm, 0.01 mbar) (b) (6 cm, 0.001 mbar) (c) (3 cm, 0.01 mbar) and (d) (3 cm, 0.001 mbar).

Smoother films could be grown at the T-S distance of 6 cm. Surface roughness increased with lowering of argon pressure and T-S distance. This may be because at lower T-S distances, the energy of the adatoms are too high that re-sputtering might have occurred, thereby increasing the roughness of the film. At the higher T-S distance of 6 cm, the adatoms reach the substrate with energies

sufficient enough to support smoother film growth with better nucleation. The lower values of the plasma parameters (kT_e and V_s) at 6 cm substantiate these observations. The high ambient gas pressure also helps in reducing the film roughness or fissure during film deposition and nucleation.

5.4 Conclusion

Spatial investigations were carried out in RF sputtered ZnO plasma using optical emission spectroscopy and Langmuir probe. The OES at 0.01 mbar revealed the absence of oxygen emission lines indicating either the deficiency or absence of excited or ionic states of the element. The spatial variation of the integral intensity of spectral emissions becoming maximum at 3 cm from the target is indicative of the focusing of the plume at this distance due to the magnetic field of the magnetron.

The voltage ramp and data acquisition set-up indigenously constructed for the Langmuir probe investigation functioned excellently well and exhibited very good repeatability for the I-V characteristic. The probe current ran smoothly from ion saturation region to electron saturation region. Both the electron density and electron temperature increased with increase in RF power. The electron density increased with increase in argon pressure ($\sim 10^{17} \text{ m}^{-3}$ for 0.01 mbar) and exhibited maximum values between distances of 3 cm and 4 cm from the target. The electron temperature, kT_e at 0.01 mbar was found to be the least, indicating minimum thermal energy for the plasma. The electron temperature also decreased steadily with increase in distance from the target. The plasma potential, which is a measure of ion kinetic energy, was least at 0.01 mbar pressure. Minimum kinetic energy for ion is preferred for fissure free thin film growth so as to eliminate the possibility of re-sputtering from the substrate.

XRD and SEM analysis of the films deposited at various conditions suggests that argon pressure of 0.01 mbar and RF sputtering power of 100 W produces smooth crystalline films when substrates are placed 6 cm away from the target.

References

- [1] M. K. Jayaraj, K. J. Saji, K. Nomura, T. Kamiya, and H. Hosono, *J. Vac. Sci. and Technol. B*: **26 (2)**, 495 (2008).
- [2] K. J. Saji, M. K. Jayaraj, K. Nomura, T. Kamiya, and H. Hosono, *J. Electrochem. society*, **155(6)**, H390 (2008).
- [3] K. J. Saji and M. K. Jayaraj, *Physica Status Solidi A*: (in press).
- [4] G. Anoop, K. Mini Krishna and M. K. Jayaraj, *J. Alloys and Compounds* (In press).
- [5] G. Anoop, K. Mini Krishna, and M. K. Jayaraj, *Applied Physics A: Mat. Sci. and Processing* **90**, 711 (2008).
- [6] G. Anoop, K. Mini Krishna and M. K. Jayaraj, *J. Electrochem. Soc.* **155**, J7 (2008).
- [7] K. Mini Krishna, G. Anoop, and M. K. Jayaraj, *J. Electrochem. Soc.* **154**, J310 (2007).
- [8] M. K. Jayaraj, A. Antony, and R. Manoj, *Bull. Mat. Sci.* **25**, 227 (2002).
- [9] R. O. Ndong, F. P. Delannoy, A. Boyer, A. Giani and A. Foucaran, *Mat. Sci. Engg. B*: **97**, 68 (2003).
- [10] A. Palmero, E. D. van Hattum, W. M. Arnoldbik, A. M. Vredenberg, and F. H. P. M. Habraken, *J. Appl. Phys.* **95**, 7611 (2004).
- [11] J. Hopwood, C. R. Guarnieri, S. J. Whitehair, and J. J. Cuomo, *J. Vac. Sci. Technol. A*: **11**, 152 (1993).
- [12] T. Nagata, A. Ashida, N. Fujimura, and T. Ito, *J. Appl. Phys.* **95**, 3923 (2004).
- [13] A. A. Shatas, Y. Z. Hu, and E. A. Irene, *J. Vac. Sci. Technol. A*: **10**, 3119 (1992).

- [14] J. Hopwood, C. R. Guarnieri, S. J. Whitehair, and J. J. Cuomo, *J. Vac. Sci. Technol. A*: **11**, 152 (1993).
- [15] K. J. Saji, N. V. Joshy, and M. K. Jayaraj, *J. Appl. Phys.* **100**, 043302 (2006).

CHAPTER VI

Spectroscopic investigations of laser ablated PZT plume

Abstract

Lead zirconium titanate (Pb [Zr_{0.52}Ti_{0.48}] O₃) target (PZT) was ablated by the third harmonic of Nd:YAG laser in various oxygen ambient pressures and laser fluences. Optical emission spectroscopic technique was used to characterize the plasma. The qualitative elemental analysis of the plume along the propagation direction of the plume was carried out. The wavelength dispersed spectra contained numerous emission lines of titanium in the neutral and singly ionized states. The emission lines of zirconium (Zr) and lead (Pb) were of feeble intensity and exhibited severe attenuation spatially. The increase in oxygen partial pressure and laser fluence increased the intensities of emission lines of all species. The spatial variations of electron temperature and electron density of the plume were investigated. The time of flight of specific emissions from the plume was performed and kinematics of species studied over the various ablation conditions typically employed in the deposition of PZT thin films.

6.1 Introduction

Pulsed laser ablation is applicable to all solid samples, irrespective of its composition and bulk electrical conductivity [1-3]. It is therefore a widely used technique for either analytical purposes or deposition of thin films of variety of materials. Lead zirconium titanate (PZT) ($\text{Pb} [\text{Zr}_{0.52}\text{Ti}_{0.48}] \text{O}_3$) is a multi-component insulator target material, from which perovskite thin films are grown by laser ablation [4-6]. PZT thin films possess a wide range of ferroelectric properties and have promising potential for applications in optoelectronic devices, dynamic random access memory (DRAM) devices, and non volatile memory devices [7-10]. It also finds applications in the making of ultrasound transducers and other sensors and actuators, as well as high value ceramic capacitors. PZT thin films exhibit high electromechanical coupling coefficients, and possess relatively high dielectric constants [5,7-11]. PZT has attracted wide interest in the recent time because of its potential applications in piezoelectric and pyroelectric devices [5,11]

The growth of perovskite PZT films by pulsed laser deposition is, however, very complicated due to the preferential occurrences of the pyrochlore phase, zirconium rich phase and the susceptibility of these materials to PbO loss. Even though PZT thin films are synthesized by a variety of plasma assisted deposition techniques, there appears to have been little attention paid in the characterization of the plasma from which these films are grown. The appearance of laser induced PZT plume changes markedly with the ablation conditions. Plasma produced has a very short temporal existence and is transient in its nature with a fast evolution of the characteristic parameters that are heavily dependent on irradiation conditions such as incident laser fluence, irradiation spot size, ambient gas composition and pressure. The investigation on the behavior of these plumes is thus of importance for

understanding the mechanism that influences the characteristics of PZT thin films synthesized via PLD process.

The optical emission spectroscopy (OES) has been successfully applied over many years to characterize the plume ejected from the laser ablated metallic, semiconducting or insulator materials [12-15]. These target materials are generally single or two component systems. The plasma plume characterization of multi-component superconducting targets is also reported [2,16]. The plasma characterization of these materials is more challenging than those of single or two components systems owing to the complexities in the dynamics of the species in the plasma. The laser induced plasma plume kinematics is strongly influenced by the presence of species of different atomic masses, their ionization states and occurrence of quasi-stable molecules and their respective relative abundance in the plume. It is therefore essential to study the plume kinematics with variations in the input parameters of ablation processes so as to optimize the conditions favorable for high quality thin films. In this study, the characterization of plasma plume emanating from the ablation of PZT target using third harmonics (355 nm) of Nd:YAG laser, in various oxygen ambient pressures is performed using optical emission spectroscopy.

6.2 Experimental set-up

The PZT target was prepared by solid state reaction as described in section 2.2.1(c). The Q-switched Nd:YAG laser was focused on to the target to a spot size of 1 mm diameter and the fluence was varied from 1.27 Jcm^{-2} to 5.08 Jcm^{-2} . The ablation was carried out at 0.001 mbar, 0.01 mbar and 0.1 mbar oxygen ambient pressures. The plume generation, imaging and simultaneous recording of wavelength dispersed emission spectra and optical TOF transients of emission features from the plume were performed using

the experimental set-up described in section 2.2.1. The monochromator was calibrated using the method described in section 3.2.2 and the spectrometer resolution was determined.

6.3 Results and discussion

6.3.1 Spectral intensity

The spectra of PZT plasma was recorded in the wavelength range 400 nm to 850 nm at various positions of the plume along the target normal. The species emerged from the target spread out, forming a plume that looked like the tail of a comet when the oxygen pressure was low. Significant variations in the intensities of emission lines of various atomic and ionic species in the plasma were observed with changes in laser fluence, ambient gas pressures and positions along the target normal. A typical wavelength dispersed PZT plasma spectrum is shown in figure 6.1 (a) & (b), which was recorded from the emissions close to the target surface (3 mm distance) at the laser fluence of 3.81 Jcm^{-2} and 0.001 mbar oxygen pressure. The spectrum of PZT is composed of numerous Stark broadened emission lines due to various atoms and ions in the plasma, superimposed on a continuous background. The background emission is attributed to the bremsstrahlung of electrons heated by interaction with laser radiation, and /or black body emission from the large particulates ejected from the target. The increased line width are due to the stark broadening caused by the high charge density which is a typical phenomenon in the laser ablated plasma at the fluence range employed in this investigation. Stark broadened emission profile is Lorentzian in nature. The contribution from other line broadening mechanism like Doppler broadening [Eq. (3.2)] has been found to be insignificant as compared to line width of emissions due to Stark broadening. The individual line profiles,

whose FWHM were used for the calculation of plasma parameters have been separately verified for the Lorentzian fit.

Large number of emission lines of neutral titanium (Ti I) are found to be intense compared to those of other species. The spectral emission intensities were found very weak for low laser fluence (1.27 Jcm^{-2}) and showed severe attenuation at large distances from the target for high ambient gas pressures. Singly ionized titanium (Ti II) emission lines were observed at all laser fluences and ambient gas pressures. The emission lines corresponding to zirconium (Zr I) and lead (Pb I) were very feeble and suffered severe attenuation beyond 5 mm distance from the target at all ablation conditions used in this investigation. The oxygen emission lines at 777.5 nm and 844.64 nm were found to have intensity at par with many of the Ti I emissions. The line at 710 nm (unmarked) is due to the harmonic of the laser wavelength used in the ablation.

It has been observed that, for sufficiently high ambient gas pressure (~ 0.1 mbar), the spectral line intensities of all species in the plasma plume exhibited a marked increase at all laser fluences, in the immediate vicinity of the target but suffered severe attenuation beyond few millimeter distance from the target. The plume expansion decreased and the plume showed a tendency to assume hemispherical shape with increase in oxygen ambience, which is discussed in the later section. The emission intensity line profiles increased with increase in laser fluences.

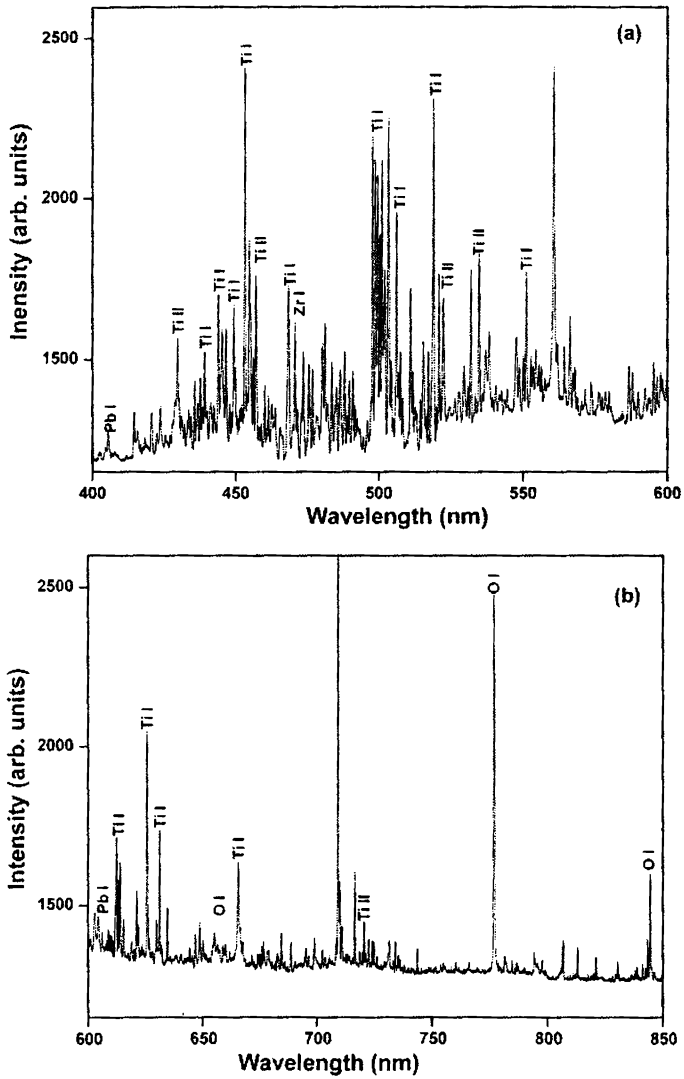


Fig.6.1 Wavelength-dispersed emission spectrum of PZT recorded in the wavelength range (a) 400 nm to 600 nm and (b) 600 nm to 850 nm, at 3 mm from the target along the surface normal at laser fluence of 3.81 Jcm^{-2} and oxygen pressure of 0.001 mbar.

(a) Titanium neutral: [Ti I]

The typical stark broadened emission line profile of Ti I at 453.34 nm recorded at a distance 3 mm from the target when ablated with a laser fluence of 3.81 Jcm^{-2} is shown in figure 6.2.

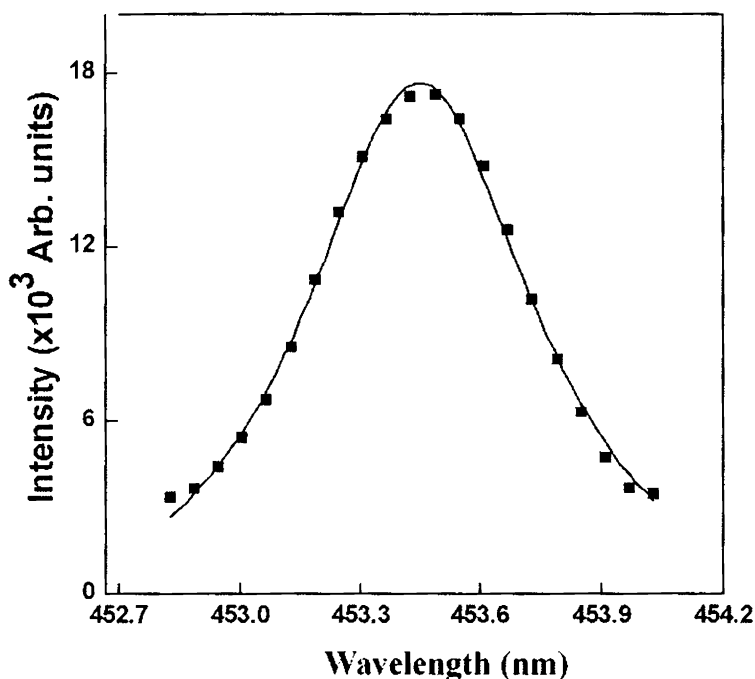


Fig.6. 2 Stark broadened emission profile of 453.34 nm Ti (I) line at 3 mm distance from the target and 3.81 Jcm^{-2} laser fluence, with corresponding Lorentzian fit (solid line).

Spatial variations of the integral intensities of this spectral line have been studied as a function of laser fluence and ambient gas pressure. It has been observed that at low oxygen pressure the intensity variation exhibited exponential or inverse (at low fluence) decay with distance, while at very high ambient pressure (0.1 mbar) nearly linear decay was observed. Fig.6.3 (a, b and c) represent the spatial variation of Ti I emission at oxygen pressures 0.001 mbar, 0.01 mbar and 0.1 mbar respectively for various laser fluences.

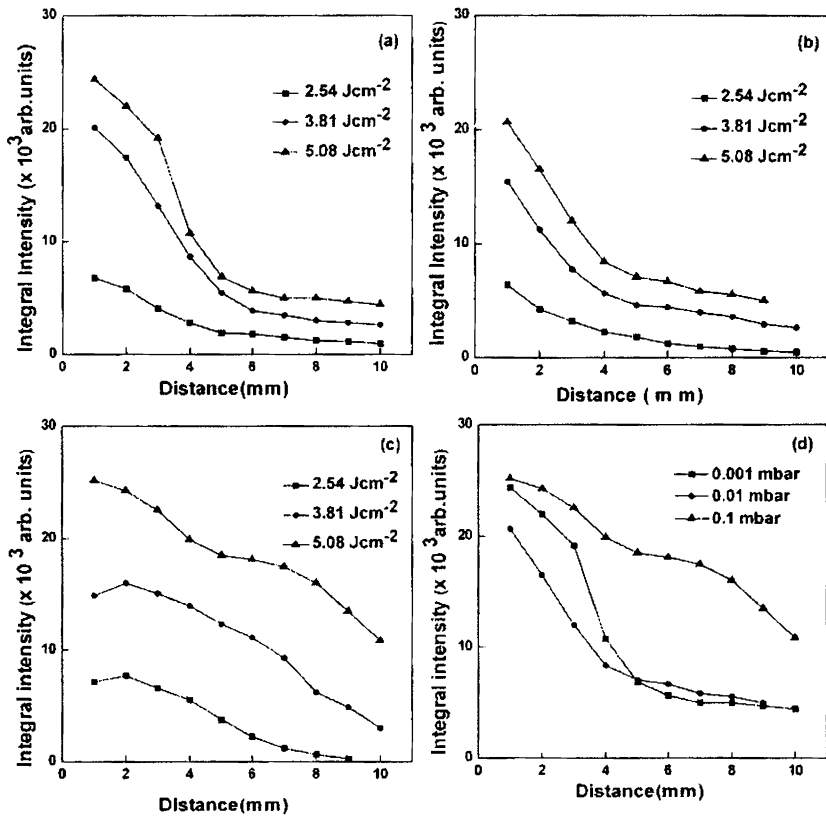


Fig.6.3 The spatial variation of integral intensity of Ti I [453.34 nm] at (a) 0.001 mbar, (b) 0.01 mbar and (c) 0.1 mbar oxygen pressures. (d) The comparison of spectral intensity variation at various oxygen pressures for the laser fluence 5.08 Jcm^{-2} .

The integral intensity of Ti I lines shows a tendency to decrease sharply in the close vicinity of the target at low ambient gas pressure (0.001 mbar and 0.01 mbar) [Fig. 6.3 (a) and (b)]. The intensity decay is rapid up to 5 mm distance from the target surface and there after remained steady for all laser fluences. At the lowest laser fluence (2.54 Jcm^{-2}) the integral intensity of Ti (I) is very low near to the target surface compared to the intensities of emission at higher laser fluences. The rate of decrease of intensity with

distance (dl/dz) is also small at low laser fluences. At high laser fluences, the plasma density as well as plume expansion velocity is high so intensity of lines could be initially high, but are likely to decay fast owing to high expansion velocity associated with the plasma expanding to larger volume. The intensity decay is more pronounced at reduced oxygen pressure. In figure 6.3 (c) the Ti I spectral emission characteristics at high ambient pressure (0.1 mbar) is shown. The gradient of emission intensity decay is almost uniform at all laser fluences. The comparison of a spectral intensity variation at various oxygen pressures for laser fluence of 5.08 Jcm^{-2} is shown in figure 6.3 (d). High emission intensities at high ambient gas pressure is an indication of the back ground gas impeding the free expansion of the plume

(b) Titanium ion: [Ti II]

The spectral emission at 522.54 nm was used to monitor the intensity variations of titanium ion (Ti II). The Fig. 6.4 (a - c) shows its emission intensity variations with respect to the variations in laser fluence and oxygen pressures, 0.001 mbar, 0.01 mbar and 0.1 mbar respectively and figure 6.4 (d) is the comparison of emission line at various pressures. The variations have been found to be similar to those of neutral titanium described above but with reduced integral intensity in each case. The gradient of intensity decay is greater than that of Ti I at all ambient pressures. This shows that the population density of titanium ion decreased with distance from the target and increase of oxygen partial pressure. This is because of the rapid decrease of population of Ti II in the plume due to the electron-ion-recombination process taking place in the plume. The increase in pressure will decrease the mean free path of the particles in the plume; thereby increasing the probability of collision of Ti II with electrons in the plume [refer section 1.3.2]. This will enhance the rate of electron-ion recombination, leading to the increase in the number of excited neutral Ti atoms.

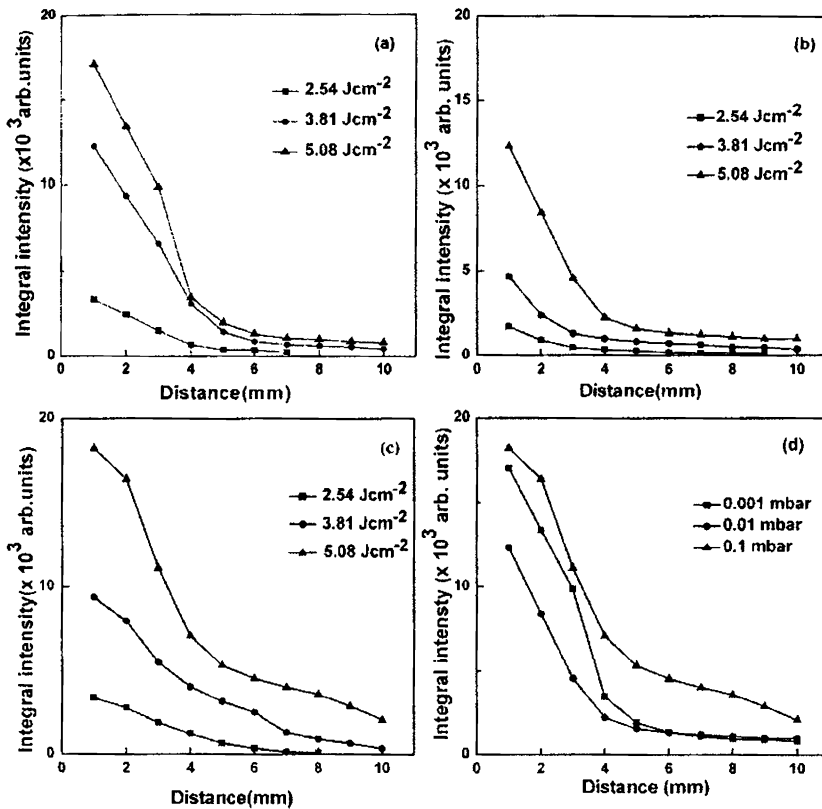


Fig.6.4 The spatial variation of integral intensity of Ti II [522.54 nm] at (a) 0.001 mbar, (b) 0.01 mbar and (c) 0.1 mbar oxygen pressures. (d) The comparison of spectral intensity variation at various oxygen pressures for laser fluence of 5.08 Jcm^{-2} .

(c) Oxygen neutral: [O I]

The oxygen spectral emissions (777.5 nm and 844.64 nm) were recorded at all ablation conditions with intensities at par with many of the Ti I and Ti II emission lines but exhibited different spatial behavior. Emission at 777.5 nm was used to study the spatial variation of integral intensity of spectral emission of oxygen. Spectral emission at 844.64 nm is weak compared 777.5 nm emission. Oxygen only in the neutral state was identified in the PZT plasma plume generated at all laser fluences and ambient pressures. At all

the oxygen partial pressures employed in the ablation, the oxygen emission line intensities increased initially from points closer to the target, attained maximum at a distance few millimeters from the target and then decreased sharply for high partial pressure and slowly for small partial pressures. These features of oxygen spectral emission in PZT plasma are identical with those in the ablation of ZnO in the oxygen and nitrous oxide ambient pressures discussed in Chapter III. The intensity of O I emission obtained in ZnO plasma are many folds higher than those of PZT plasma for similar laser fluence range. After an initial tendency to increase the integral intensity of emission lines along the propagation direction of the plume, it suffered severe attenuation beyond 6 mm distance from the target. Oxygen emission intensity variation exhibited greater spatial coverage in ZnO plasma [refer Fig.3.5 and Fig. 3.9]. The increase in ambient pressure increased the emission intensity of oxygen emission in PZT plasma also. From the

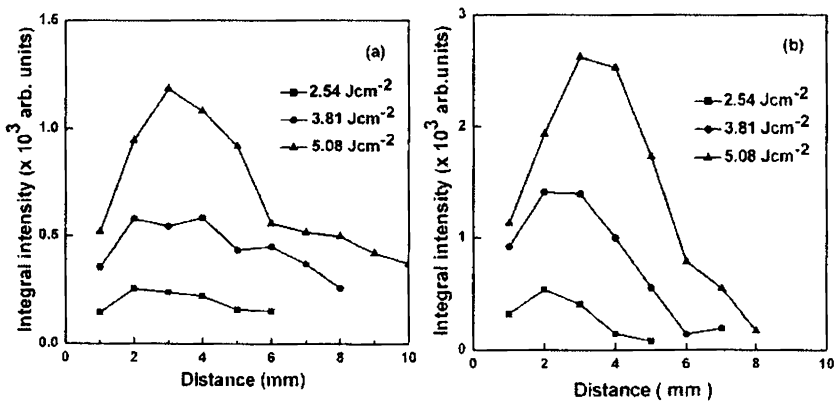


Fig: 6.5 Variation of integral intensity at various pressures and fluences of O I [777.65 nm] spectral line at (a) 0.001 mbar (b) 0.1 mbar.

graph [Fig.6. 5 (a) and (b)] it is clear that emission line intensities were detectable even in the neighborhood of 10 mm from the target when ablated at low ambient gas pressure (0.001 mbar). The intensity values at spatial positions along the target normal, when ablated at 0.1 mbar is more than twice the corresponding values at 0.001 mbar ambient pressure. According to the shock wave (SW) model [17,18] of the laser induced plasma, only after the ambient gas has been compressed beyond a certain threshold, does the shock wave become strong enough to excite the ambient gas [17-21]. The growth of the ferroelectric oxide films is highly dependent on the oxygen partial pressure [5,6]. Therefore to have more oxygen content in the plasma it is advisable to ablate PZT at high oxygen partial pressures.

(d) Zirconium neutral: [Zr I]

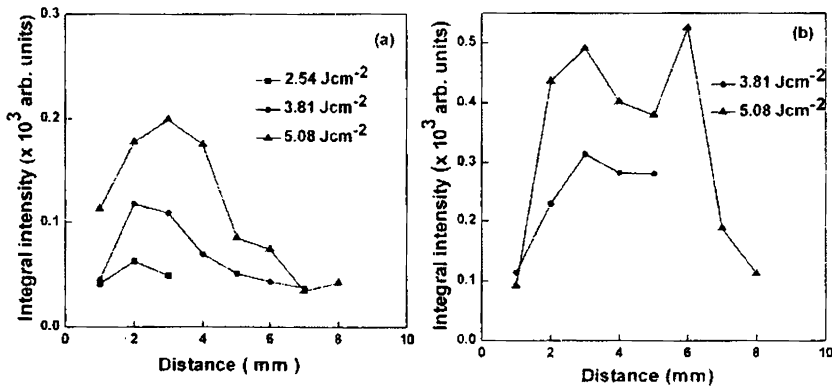


Fig. 6.6 Variation of integral intensity of Zr I [470.98 nm] at (a) 0.001 mbar and (b) 0.1 mbar for various laser fluences.

Analysis of wavelength dispersed spectrum of PZT revealed that the presence of emission intensities of lead and zirconium are very feeble at all laser fluences and ambient gas pressures compared to Ti I, Ti II and O I emission lines. The spatial behavior of intensity is that the severe attenuation took place beyond few millimeters from the target at all ablation conditions.

Still these emission line intensities were found to be enhanced as the ambient pressure was increased. The percentage content of these elements in the target is considerable but the intensity behavior suggests that radiation-less transitions may be mostly taking place from these elements. This phenomenon will enhance the emission of continuum radiation due to inverse bremsstrahlung [refer section 1.3.3]. The continuum emission on which emission lines were superimposed, were strong in the PZT plasma. Figures 6.6 (a) & (b) represent the spatial intensity variations of Zirconium neutral emission at two extremes of oxygen pressures with reference to the fluence variations. Similar behavior was exhibited by emissions from lead neutral (406.21 nm) also. The line intensities get attenuated after few millimeter distances from the target does not mean that the respective species cease to exist after these points along the target normal. It only means that the quantum of light emitted from the species is not sufficient to be detected beyond these points. The species still will have sufficient velocities to move forward and reach the substrate to form thin films as evident from the kinetic energies derived from the time of flight (TOF) studies discussed later (section 6.3.4).

6.3.2 Electron density (N_e)

The N_e in the plasma plume emanating from the pulsed laser ablation of PZT was studied with variations in laser pulse energy and ambient gas pressure. The spatial variation of the electron number density was determined. Line shape analyses of specific emission lines were done at different distances from the target. This provides a direct indication of space evolution of electron density, which gives an insight into the basic ionization process taking place in plasma. Since the plasma is quasi-neutral, the electron number density is a measure of the number of ionic species present in the plasma. The OES technique was used for determining N_e . The full width at

half maximum (FWHM) corresponding to the emission line of oxygen at 844.64 nm was used to calculate electron density N_e . The validity of LTE was established by checking the McWhirter criterion (refer Eq. 1.29). The contribution of Doppler broadening and pressure broadening to the line width of emission lines were analyzed by the method describe in the section 3.3.1. These broadening effects were found to be too small compared to the measured FWHM of emission line (844.64 nm) and hence ignored. This suggests that in LTE the line broadening is predominantly due to electron impact giving rise to Stark broadened lines which are generally Lorentzian. The emission profile of 844.64 nm line exhibited perfect Lorentzian fit. Equation (1.42) was used for the calculation of N_e . The approximate electron temperature (kT_e) value needed for calculating electron impact parameter (W) of equation (1.42) was determined using the ratio of intensities of emissions from the same ionization state given by Eq. (1.44).

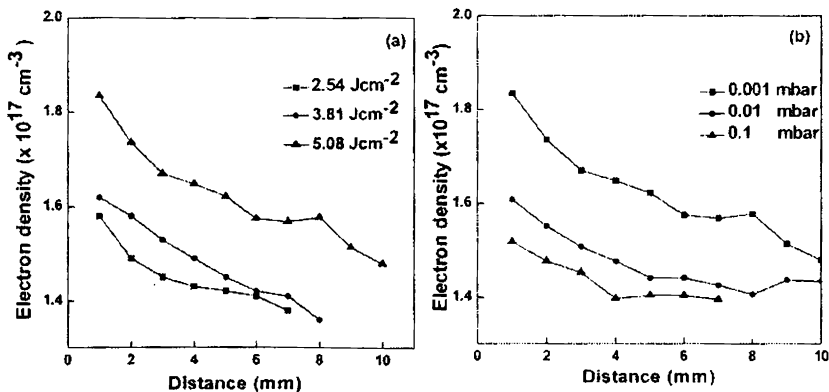


Fig 6.7 Spatial variation of electron density at (a) 0.001 mbar oxygen pressure, various laser fluences and (b) 5.08 Jcm^{-2} laser fluence and various oxygen pressures

The electron density (N_e) exhibited gradual decrease with distance from the target surface at all laser fluences and the rate decreased with decrease in laser fluence [Fig. 6.7 (a)]. The electron density variations over the laser

fluence range has been found to be from $1.58 \times 10^{17} \text{ cm}^{-3}$ to $1.83 \times 10^{17} \text{ cm}^{-3}$ in the vicinity of the target ($\sim 1\text{mm}$) while away from the target ($\sim 10 \text{ mm}$ distance), it varied from $1.37 \times 10^{17} \text{ cm}^{-3}$ to $1.58 \times 10^{17} \text{ cm}^{-3}$ for the same laser fluence range. This indicates that the increase in laser fluence does not appreciably increase electron or ion density in PZT plasma. Similar effect was exhibited by laser ablated ZnO plasma also. This is generally observed in the case of ablation of targets with nano-second laser pulses [15,22-24]. One of the peculiarities exhibited by multi-component PZT plasma as opposed to ZnO plasma is that the N_e values decreased with increase in ambient gas pressure [Fig.6.7 (b)]. The plume propagation length in PZT plasma was found to be less compared to that of ZnO plasma. This is evident from the spatial extent to which OES measurement was possible in both the plasma. In ZnO plasma measurements above 20 mm was possible while in PZT plasma measurements were possible below 10 mm distance from the target in many situations. The PZT plume size was small and shape almost hemispherical at 0.1 mbar oxygen pressure exhibiting restricted forward propagation. The plume shrinkage with increase in pressure is a well known phenomenon in LIP [25,26]. The plasma is confined to smaller volume at increased ambient pressure, so that the probability of electron-ion recombination exceeding the probability of collisional ionization due to reduction in the mean free path may be attributable to PZT plasma for lowering of N_e with increase in oxygen pressure.

6.3.3 Electron temperature (kT_e)

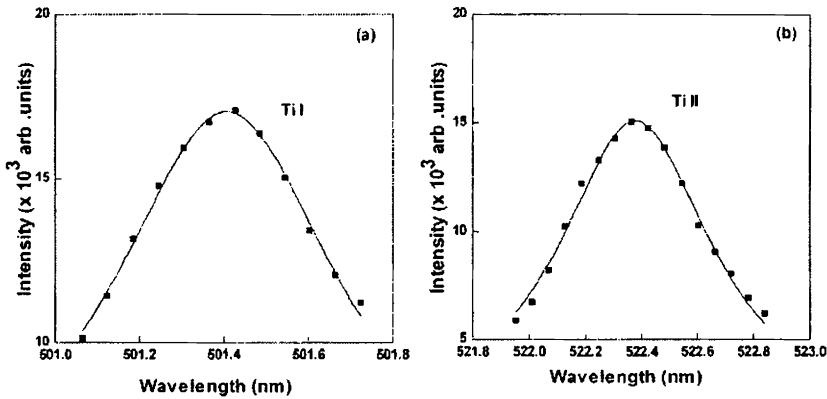


Fig.6.8 The Lorentzian fit (solid line) of emission lines of (a) Ti I (501.41 nm) and (b) Ti II (522.38 nm) at 3 mm from the target and 0.1 mbar oxygen pressure, used for the calculation of electron temperature

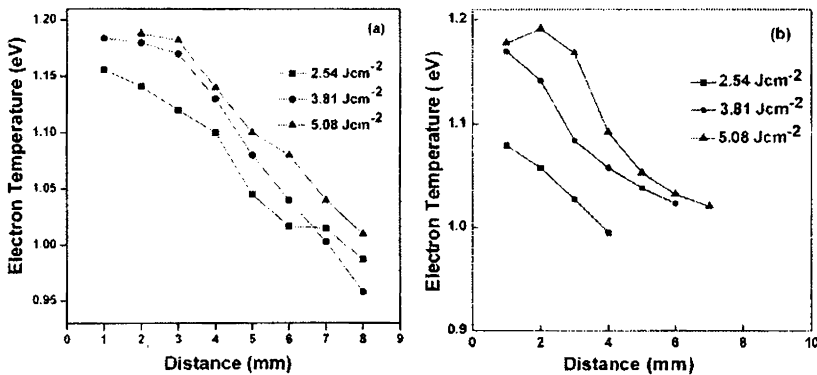


Fig.6.9 Spatial variation of Electron Temperature at (a) 0.001 mbar and (b) 0.1 mbar oxygen ambiances for various laser fluences.

The ratio of emission line intensities of successive ionization states of the same element was used for the accurate determination of electron temperature of the plume [Eq. (1.45)]. The emission line intensities of 501.41 nm and 522.38 nm respectively of Ti I and Ti II have been used for the determination of electron temperature. The optical data needed for the calculation were taken from Ref. 27 and NIST atomic spectra data base [28].

The line shape analysis of the above mentioned lines were performed at different spatial points of the plume in a time integrated manner. The emission lines at all spatial positions were of perfect Lorentzian fit, indicating the occurrence of Stark broadening of emission lines leading to the accuracy of the calculations. The figures 6.8 (a) & (b) are the typical Lorentzian fit of the 501.41 nm and 522.38 nm emission lines of Ti I and Ti II at 3 mm from the target and 0.1 mbar oxygen pressure. The electron temperature values of the plume at various spatial points along the surface normal are determined for 2.54 Jcm⁻², 3.81 Jcm⁻² and 5.08 Jcm⁻² for two very different oxygen partial pressures of 0.001mbar and 0.1 mbar is shown in figures 6.9 (a) and (b) respectively.

In both the ambient gas pressures a slow and steady decrease of electron temperature with distance was observed. The kT_e values have been found to decrease from about 1.2 eV at 1 mm and 0.98 eV at 10 mm distance from the target surface. The electron temperature values of the plasma at all spatial points have been found to increase with increase in laser fluences. But large variations T_e values have not been exhibited in the laser fluence range employed in this study. Hence for slow thin film growth by PLD, small laser irradiation power, high ambient gas pressure and longer ablation time seem to be conducive for film growth using third harmonic of Nd:YAG laser.

6.3.4 Time of flight studies (TOF)

The time of flight (TOF) behavior of various species of the plume was performed by selecting strong emission lines of individual elements using the monochromator and feeding them to the PMT which was optically coupled to the monochromator. The current output from the PMT was dropped across 50 ohm resistor and fed to 100 MHz digital storage oscilloscope. The oscilloscope was interfaced with a computer for storage

and subsequent processing of TOF spectra. The detailed experimental set-up is discussed in section 2.2.1.

As a general tendency, the velocities of all the species in the plume have been found to decrease with distance from the target. The velocities were found to be of the order of 10^6 cm/sec at points close to the target surface and decreased with distance to the order of 10^5 cm/sec. The increase in laser fluence enhanced the velocities at all ambient pressures. Even though the integral intensities of all emission lines attenuated beyond 10 mm distance from the target during plasma expansion, the plasma particle whether ionic or otherwise do not get perished at these distances. The particles will have sufficient energies, as seen from their respective velocities at all ablation conditions; can reach the substrate and deposit. The velocities and the respective kinetic energies of Zr I, Ti I and O I are tabulated in TABLE 6.1.

TABLE 6.1. The spatial variations of velocities and kinetic energies of Zr I, Ti I and O I at 0.001 mbar oxygen ambience and 5.08 Jcm^{-2} laser fluence.

| species | Pressure (mbar) | Distance (mm) | Velocity ($\times 10^5 \text{ cms}^{-1}$) | K.E (eV) |
|---------|-----------------|---------------|---|----------|
| Zr I | 0.001 | 3 | 15.2 | 107.82 |
| | | 5 | 7.79 | 28.94 |
| | | 7 | 6.03 | 17.4 |
| Ti I | 0.001 | 3 | 9.98 | 24.82 |
| | | 5 | 6.34 | 10.02 |
| | | 7 | 6.25 | 9.73 |
| O I | 0.001 | 3 | 7.23 | 4.37 |
| | | 5 | 6.46 | 3.49 |
| | | 7 | 6.40 | 3.43 |

The TOF spectra of Ti (I) and O (I) with respect to various distances and laser fluences of 3.81 Jcm^{-2} and 5.08 Jcm^{-2} are given below [Fig. 6.10 (a, b, c and d)]. The spectral intensities and velocities of both the species increased with increase in laser fluence. Of all the species the kinetic energy of zirconium was found to be maximum with 17.4 eV at 7 mm distance from the target while that of oxygen registered the least energy (3.43 eV) for the laser fluence 5.08 Jcm^{-2} (TABLE 6.1).

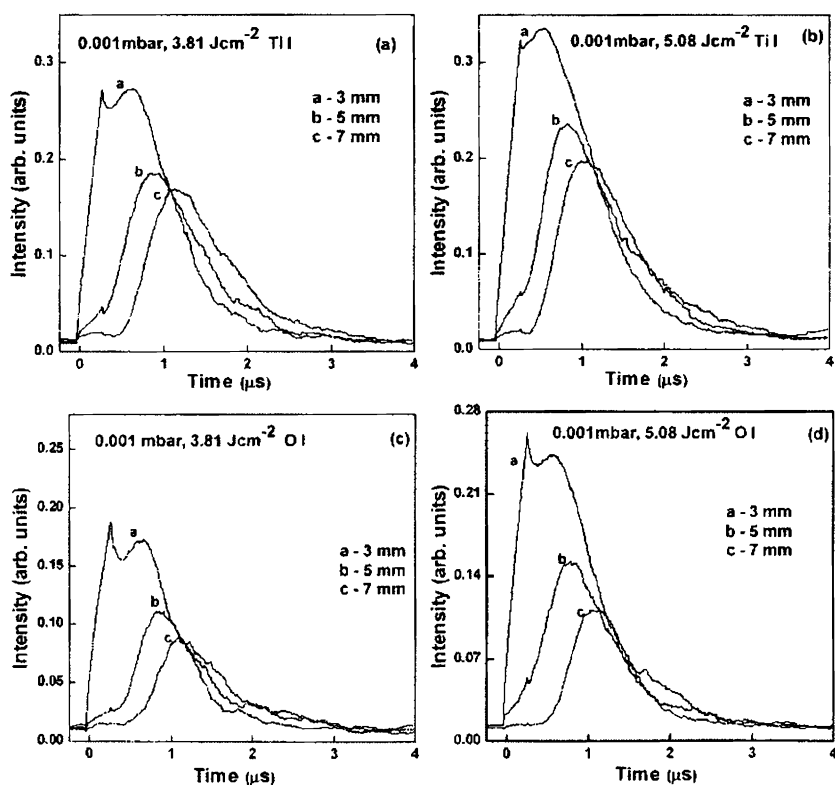


Fig. 6. 10 TOF spectra of Ti I and O I emissions at 0.001mbar pressure and monitored at distance, $d=3 \text{ mm}$, 5 mm , and 7 mm along the surface normal for laser fluences (i) 3.81 Jcm^{-2} and (ii) 5.08 Jcm^{-2}

An initial spike in the TOF of all species is observed at all distances from the target surface irrespective of the kind of species and laser fluence. The appearance of the fast and sharp spikes is due to the initial excitation of ambient gas molecule by the interaction with the laser pulse before the event of ablation process. This becomes less pronounced with increase in distance from the target. The spikes are prominent at low laser power due to the fact that decrease in laser power decreases the emission intensity of the selected lines thereby the spikes gaining prominence.

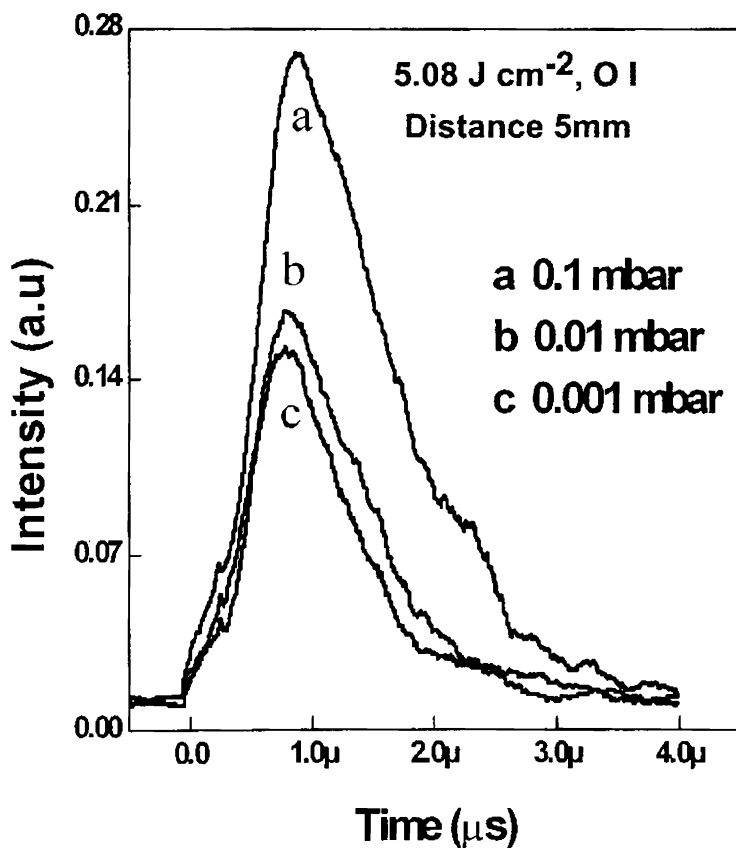


Fig.6.11 TOF spectra of O I recorded at (a) 0.001 mbar, (b) 0.01 mbar and (c) 0.1 mbar oxygen pressures and 5mm distance from the target, along the surface normal for the laser fluence of 5.08 J cm^{-2}

TOF of O I (777.5 nm) emission recorded at different oxygen pressure for laser fluence 5.08 Jcm^{-2} is shown in figure 6.11. The increase in ambient oxygen partial pressure increased the intensity of the emission lines but delayed the arrival time, thereby reducing the velocity of propagation. Similar variations of TOF spectra were exhibited by other species also. This in accordance with the impedance offered to the forward propagation of the plume by the increase in the ambient gas pressure. The increase in peak intensity with increase in pressure suggests that the number of emitting species per unit volume of the plume increases due to plume shrinking at high oxygen ambience as discussed above. This is found to be true for the TOF of all species investigated.

6.4 Conclusions

The characteristic emissions from species in the laser induced plasma plume were analyzed as a function of distance from the target, laser fluence and ambient gas pressure, using optical emission spectroscopy. Numerous emission lines of titanium neutral were present in the spectrum within the wavelength range of 400 nm to 850 nm. The emission lines corresponding to titanium ions (Ti II) were also recorded with high intensity. The spectral emissions of Pb I and Zr I were very few and intensity feeble in the spectra taken at all ablation conditions. The spectral line intensities of these elements were found to suffer severe attenuation along the plume propagation direction compared to those of Ti I, Ti II and O I species. The estimation of electron temperature and density was carried out up to 10 mm distance from the target surface. Both these parameters decreased with distance from the target. The electron temperature decreased from 1.22 eV to 0.98 eV for distance variation of 1 mm to 10 mm from the target surface while the

electron density varied from $1.83 \times 10^{17} \text{ cm}^{-3}$ to $1.48 \times 10^{17} \text{ cm}^{-3}$ in the same spatial range for laser fluence of 5.08 Jcm^{-2} . Large differences in the values of electron density and electron temperature were not observed with variations in laser power and oxygen ambient gas pressure. Kinetic energies of zirconium and titanium are many folds greater compared to that of oxygen. To reduce the kinetic energies of the species high ambient gas pressure is required. Reduction in the kinetic energies of the species is required as high energetic particles bombard the substrate and cause damage to the film grown. The control of kinetic energy of these particles also avoids the occurrence of secondary phase such as pyrochlore phase and zirconia-rich phase reported in PZT thin film growth [5,6]. The plasma investigation of laser ablated PZT, therefore suggests that the target be ablated at low laser fluence in presence of high oxygen ambient pressure for the uniformity in deposition and nucleation of perovskite film growth.

References

- [1] A. Mele, A. G. Guidoni, R. Kelly, C. Flamini, and S. Orlando, *Appl. Surf. Sci.* **109**, 584 (1997).
- [2] H. F. Sakeek, T. Morrow, W. G. Graham, and D. G. Walmsley, *J. Appl. Phys.* **59**, 3631 (1991).
- [3] F. Cervelli, F. Fusco, M. Allegrini, and E. Arimondo, *Appl. Surf. Sci.* **127**, 679 (1998).
- [4] L. Lian, and N. R. Sottos, *J. Appl. Phys.* **87**, 3941 (2000).
- [5] H. Kidoh, T. Ogawa, A. Morimoto, and T. Shimizu, *Appl. Phys. Lett.* **58**, 2910 (1991).
- [6] J. S. Horwitz, K. S. Grabowski, D. B. Chrisey, and R. E. Leuchtner, *Appl. Phys. Lett.* **59**, 1565 (1991).
- [7] G. H. Heartling, *Ferroelectrics* **75**, 25 (1987).
- [8] C. A. P. de Araujo, L. D. Mcmillan, B. W. Melnick, J. D. Cuchiaro, and J. F. Scott, *Ferroelectrics* **104**, 241 (1990).
- [9] D. W. Bondurant, F. P. Gnadinger, *IEEE Spectrum* **7**, 30 (1989).
- [10] C. J. Chen, E. T. Wu, Y. H. Xu, K. C. Chen, and J. D. Mackenzie, *Ferroelectrics* **112**, 321 (1990).
- [11] S. Watanabe, T. Fujiu, and A. Tanaka, *Appl. Phys. Lett.* **62** 3377 (1993).
- [12] R. L. Vander Wal, T. M. Tichich, J. R. West, and P. L. Householder, *Appl. Spectroscopy* **53**, 1226 (1999).
- [13] F. Claeyssens, A. Cheesman, S. J. Henley, and M. N. R. Ashfold, *J. Appl. Phys.* **92**, 11, 6886 (2002).
- [14] T. Nakayama, *Surface Sci.* **133**, 101 (1983).
- [15] K. J. Saji, N. V. Joshy, and M. K. Jayaraj, *J. Appl. Phys.* **100**, 043302 (2006).
- [16] H. S. Kwok, *Thin Solid Films*, **218**, 277 (1992).

- [17] P. E. Dyer, A. Issa, and P. H. Key, *Appl. Phys. Lett.* **57**, 186 (1990).
- [18] Y. B. Zeldovich, Y. P. Raizer: In *Physics of Shock Waves and High Temperature Hydrodynamics Phenomena*, **Vol. 1, 2** (Academic Press, New York 1966).
- [19] P. E. Dyer, and J. Sidhu, *J. Appl. Phys.* **64**, 4657 (1988).
- [20] X. Y. Chen, Z. C. Wu, Z. G. Liu, X. Y. Lie, and Z. S. Sha. *Appl. Phys A* **67**, 331 (1998).
- [21] G. Epurescu, J. Siegel, J. Gonzalo, F. J. Gordillo-Vazquez, and C. N. Afonso, *Appl. Phys. Lett.* **87**, 211501 (2005).
- [22] M. Ying, Y. Xia, Y. Sun, M. Zhao, Y. Ma, X. Liu, Y. Li, and X. Hou, *Laser and Particle Beam* **21**, 97 (2003).
- [23] N. M. Shaikh, S. Hafeez, B. Rashid, S. Mahmood, and M. A. Baig, *J. Phys. D: Appl. Phys.* **39**, 4377 (2006).
- [24] S. S. Harilal, C. V. Bindhu, R. C. Issac, V. P. N. Nampoore, and C. P. G. Vallabhan, *J. Appl. Phys.* **82**, 2140 (1997).
- [25] S. Amoruso, A. Sambri, and X. Wang, *J. Appl. Phys.* **100**, 013302 (2006).
- [26] S. Amoruso, A. Sambri, M. Vitiello, and X. Wang, *Appl. Surf. Sci.* **252**, 4712 (2006).
- [27] H. R. Griem, *Principles of Plasma Spectroscopy*, (Cambridge University Press, 1997).
- [28] <http://physics.nist.gov>

CHAPTER VIII

Summary and outlook

7.1 Summary

The ZnO plasma generated by pulsed laser ablation and RF magnetron sputtering has been characterized by both optical emission spectroscopy and Langmuir probe. The plasma parameters (electron density and electron temperature) were evaluated for both kind of plasma using these two diagnostic tools. The plasma generation conditions employed were typically the conditions used for the depositions of thin films. A sound understanding of the plasma plume kinematics is essential for the deposition of thin films for specific applications. The thin films produced from ZnO target fall in the category of transparent conducting oxides that fetch far reaching applications in flat panel displays and other devices like thin film transistors (TFT). For TFT fabrication using ZnO, amorphous thin films are prepared either by PLD or RF magnetron sputtering [1-3] while for EL devices crystalline films of ZnO are fabricated also by PLD or RF magnetron sputtering [4-6]. In all these device fabrications, the base material is ZnO, which is mixed with suitable materials at appropriate proportions and plasma is produced by laser ablation or sputtering under suitable ambient gas composition and pressure. Therefore it is essential that the ZnO plasma be characterized taking in to consideration the target composition, the environment of plasma evolution and the nature of energy source with which plasma is produced. The in-situ or ex-situ monitoring of the plasma is essential for understanding the plume kinematics, the degree of ionization and the spatial and temporal behavior of species. The prior knowledge of these plasma parameters enables judicious manipulation of input parameters for plasma production, creating flexibility in the deposition of thin films for specific use.

The electron density measurement in the LIP of pure ZnO and ZnO:Ga was obtained in the order of 10^{17} cm^{-3} and the electron temperature calculated was of the order of 1.2 eV. The presence of a heated substrate at 5 cm distance (a common T-S distance used for film growth) increased the ion density in the plume. ZnO thin films grown on Al_2O_3 substrate exhibited better crystallinity for the substrate temperature of 600°C , laser fluence of 2.54 Jcm^{-2} and ambient gas pressure of 0.001 mbar. The variations of N_e and kinetic energies of the species with laser fluence and the impedance offered by the ambient gas on plume propagation were taken in to consideration for fixing the deposition parameters.

In addition to the measurement of N_e by OES, the kinematics of ions and electrons were studied using Langmuir probe. Breaking of quasi-neutrality of the plume and the presence of ambi-polar electric field arising due to DL was detected. Ions accelerated to acquire energy of the order of keV were detected and the energy variations with laser fluence, ambient gas pressure and distance from the target were determined. In contrast to fast evolving ion TOF spectra, the electron TOF transients exhibited extended temporal profile.

ZnO plasma characterization in the RF magnetron sputtering yielded the plume characteristic very different from that of LIP. The electron density in the RF plasma was obtained in the range of 10^{11} cm^{-3} and electron temperature varied from 0.5 eV to 3.5 eV. Unlike LIP the electron temperature decreased with increase in ambient gas pressure while the ion density increased. The rate of variations of these parameters is also different in both plasmas. XRD and SEM analysis of the films deposited at various conditions suggests that argon pressure of 0.01 mbar and RF sputtering power of 100 W produces smooth crystalline ZnO films when substrates are placed 6 cm away from the target. The selection

of deposition parameters are in conjunction with the properties of the plasma evolution with variations in the input parameters for plasma production. In RF plasma the electron number density is 10^6 orders below while electron temperature is 2 to 3 folds more than the respective values of LIP. Plume in LIP is more of forward directional and highly transient in nature whereas the RF plasma exhibit large lateral spread and hence large area deposition is possible compared to that with LIP. The surface roughness of films deposited by LIP is less and exhibit better stoichiometry and crystallinity. The plasma density goes on decreasing with distance from the target in LIP where as in RF plasma the density increases from the target surface attains maximum at 3-4 cm distance and then decreases. The magnetic field of the magnetron restricts the free forward movement of charged particles and focuses the particles at region where magnetic field converges.

The LIP of multicomponent material -Lead zirconium titanate (PZT) ($\text{Pb}[\text{Zr}_{0.52}\text{Ti}_{0.48}]\text{O}_3$)-exhibited plasma evolution behavior similar to that of ZnO plasma. The N_e and kT_e values were obtained in the same range as in ZnO plasma. The titanium emission lines were numerous compared to emissions from other species. The emission intensity attenuation (spatial) was rapid compared to ZnO plasma. OES measurements could be performed only up to 10 mm distance from the target. The zirconium and lead emission lines were weak and were subjected to severe attenuation along the propagation direction of the plume. The velocities of zirconium, titanium and oxygen were obtained in the decreasing order but exhibited more than double the velocities of the species in ZnO:Ga plasma for similar fluence range and ambient pressure. The plume propagation was impeded by the ambient gas in PZT plasma also.

7.2 Future work

The in-situ measurement of plasma parameters will help to understand the instantaneous plasma behavior, and can control plasma production parameters for the deposition of thin films. Nonintrusive diagnostic technique is most preferred for this purpose.

The OES set-up of LIP study can be modified using LabVIEW software to achieve the plasma parameters simultaneously during the thin film deposition process.

ICCD will make possible the spectral imaging with both temporal and spatial variations. The temporal evolution of the plume can also be studied by imaging the plume at specific delay after the termination of laser pulse.

Triple probe technique [7-9] with suitable automation can be employed in the characterization of both RF magnetron sputtered and laser induced plasma. The evaluation of electron energy distribution function (EEDF) of plasma may also be studied in addition to the other plasma parameters. EEDF give additional information on the ionization process taking place in plasmas.

References

- [1] M. K. Jayaraj, K. J. Saji, K. Nomura, T. Kamiya, and H. Hosono, *J. Vac. Sci. and Technol. B: Microelectronics and Nanometer structures*, **26 (2)**, 495 (2008).
- [2] K. J. Saji, M. K. Jayaraj, K. Nomura, T. Kamiya, and H. Hosono, *J. Electrochem. I society*, **155(6)**, H390 (2008).
- [3] K. J. Saji and M. K. Jayaraj, *Physica Status Solidi:A* (in press).
- [4] G. Anoop, K. Mini Krishna, and M. K. Jayaraj, *Applied Physics A: Mat. Sci. and Processing* **90**, 711 (2008).
- [5] G. Anoop, K. Mini Krishna and M. K. Jayaraj, *J. Electrochem. Soc.* **155**, J7 (2008).
- [6] K. Mini Krishna, G. Anoop, and M. K. Jayaraj, *J. Electrochem. Soc.* **154**, J310 (2007).
- [7] Y. S. Choi, H. J. Woo, K..S. Chung, M. J. Lee, D. Zimmerman, and R. McWilliams, *J. J. Appl. Phys.* **45**, 5945 (2006).
- [8] C. Riccardi, G. Longoni, G. Chiodini, and M. Fontanesi, *Rev. Sci. Instrum.* **72**, 461 (2001).
- [9] S. P. Andreason and J. T. Slough, *Rev. Sci. Instrum.* **75**, 4302 (2004).